RATIOS OF SINGLE HADRONS PRODUCED AT HIGH TRANSVERSE MOMENTUM IN 400 GEV/C PROTON-NUCLEON COLLISIONS

A Dissertation presented

by

Henry Donald Glass

to

The Graduate School

in Partial Fulfillment of the Requirements

for the Degree of

DOCTOR OF PHILOSOPHY

in

Physics

State University of New York

at

Stony Brook

August 1985

STATE UNIVERSITY OF NEW YORK
AT STONY BROOK

THE GRADUATE SCHOOL

Henry Donald Glass

We, the dissertation committee for the above candidate for the Ph.D. degree, hereby recommend acceptance of the dissertation.

Robert L. McCarthy

Dr. Robert L. McCarthy, Associate Professor, Physics

Paul D. Grannis

Dr. Paul D. Grannis, Professor, Physics

J. Smith

Dr. John Smith, Professor, Physics

Scott Anderson

Dr. Scott Anderson, Assistant Professor, Chemistry

This dissertation is accepted by the Graduate School.

Dean of the Graduate School

August 1985

Abstract of the Dissertation

"Ratios of Single Hadrons Produced at High Transverse Momentum in 400 GeV/c Proton-Nucleon Collisions"

by

Henry Donald Glass

Doctor of Philosophy

in

Physics

State University of New York at Stony Brook

1985

We have measured ratios of single hadrons produced at high p_T in 400 GeV/c proton-hydrogen and proton-deuterium collisions. A Ring Imaging Cherenkov detector was employed to identify $\pi^{\pm}$, $K^{\pm}$, p and $\bar{p}$ in the momentum range 80-150 GeV/c. Our acceptance was defined by the region $5.0<p_T<8.0$ GeV/c and $65<\theta^{*}<95°$. We compare our measurements of the ratios K^{+}/π^{+}, p/π^{+}, K^{-}/π^{-}, $\bar{p}/\pi^{-}$, and π^{+}/π^{-} to the results of the Chicago-Princeton experiment and to the Lund high p_T physics Monte Carlo.

Table of Contents

List of Tables

List of Figures

Acknowledgments

"Oh, to be wafted away
from this black Aceldama of sorrow,
Where the dust of an earthy today
is the earth of a dusty tomorrow."
-- from the collected works
of Reginald Bunthorne

A long time ago, at some point in the remote past, I became a graduate student in high energy physics. During this period of my life I have encountered a wide variety of people who have helped me get to where I am today (wherever that is). It is appropriate at this point in my thesis (before we encounter the sex and violence in Chapter One) to thank as many people as I can think of who provided useful advice, suggestions, comments, and food and water along my journey.

First, I would like to thank all of those people who collaborated in Experiment 605 at Fermilab, especially my fellow graduate students David Jaffe, Jim Crittenden, Bob Hsiung, Yoshi Sakai, Bob Plaag, Bruce Straub, Richard Grey, and Takuo Yoshida, all of whom deserve my gratitude for their efforts above and beyond the call of duty. They know as well as anyone that the only thing better than being a graduate student is not being a graduate student.

I would also like to thank all the people I worked with on the Ring Imaging Cherenkov Detector, especially Dick Hubbard, Phillippe Mangeot, George Coutrakon, Fabio Sauli, Anna Peisert, Georges Charpak, Jacques Tichit, Jean Claude Santiard, and others from the CERN, Saclay, and Stony Brook groups.

I also extend my thanks to the cast of thousands on E605, including Chuck Brown, John Rutherfoord, Mark Adams, Steve Smith, Bill Luk, Dan Kaplan, my advisor Bob McCarthy, and everyone else.

There were a number of ways in which "life" at Fermilab was made more tolerable. One of the more outstanding ways was the forming of the "Not Ready for Beam Time Players", a group devoted to the performance of Gilbert & Sullivan operettas. I was fortunate in being involved in two performances, "Trial by Jury" and "Patience". I have never had as much fun in my life as I had while working this group of highly talented people, including Maestro Herman White, directors Carol Wilkinson and Dick Gustavson, Kevin Ford (that smug-faced idiot), Karen Simpson, Ellen Taylor, and my solicitor Leon Lederman.

In the land beyond Fermilab there are a number of small towns, including Geneva and St. Charles, both of which I spent some time living in and getting to know the local folks. My favorite local folks include John and Joan Larson and their family, especially Jamie & Jan, Charlie, Bob, Nate, Laurie, and Julie.

In addition to thanking all the above people, I extend my thanks to all gods, demons, spirits, supreme beings, and mystical forces that provided their assistance to me, whether solicited or not.

I thank Scott Sherwood, 'Hoss' Crotts and others for introducing me to their unique brand of Oriental philosophy, and especially for teaching me that all obstacles can be overcome through determination.

I would like to thank Mom and Dad, who were never quite sure what their son was up to all these years.

Finally, I cannot possibly thank enough my wife ("gosh, are we really married") Shar, who has told me on many occasions how glad she will be when I finish my thesis and become a normal person again (whatever that is). Hubba hubba.

CHAPTER 1

Introduction

High transverse momentum hadronic interactions. The motivation for studying the inclusive production of high transverse momentum particles is to gain a further understanding of the dynamics of the hard scattering of hadronic constituents. High p_T scattering is currently described by the QCD- improved parton model [1-4]. Figure 1 shows the parton model description of a high p_T hadron collision, as well as the related processes of deep inelastic lepton-nucleon scattering and the annihilation of e^+e^- into hadrons. The parton model factors the scattering process into several distinct parts:

a) The interacting hadrons are described by structure functions $G_q^h(x,Q^2)$, which give the probability of finding parton q with momentum fraction x in hadron h.

b) One constituent from each hadron interacts in a hard collision with differential cross section $d\sigma/d\hat{t}$. These cross sections have been calculated to first order in perturbative QCD [5,6] and are tabulated in Table 1 for a variety of subprocesses important in high p_T hadron production. Figure 2 shows the corresponding Feynman diagrams for these subprocesses.

c) Following the hard scattering, each parton fragments into a jet of observable hadrons, where the probability of observing a hadron with momentum fraction z of the parent parton is given by the fragmentation function $D(z,Q^2)$.

The above pieces describing the interaction can be combined to give the inclusive cross section for producing a high p_T hadron [51]:

$$E\frac{d^3\sigma}{dp^3}(p_1p_2\rightarrow h+X) = \frac{1}{\pi}\sum_{abcd}\int dx_a \int dx_b\ G_1^a(x,Q^2) \qquad (1.1)$$
$$\times\ G_2^b(x,Q^2)\ \frac{d\sigma}{dt}(ab\rightarrow cd)\ \frac{1}{z}\ D_h^c(z,Q^2)$$

The functions $D(x,Q^2)$ and $G(z,Q^2)$ have a QCD determined dependence on Q^2 [7], which can be interpreted as the square of the energy scale of the reaction. QCD has the property that as one looks at scatterings at higher and higher momentum transfers (or alternatively, smaller and smaller impact parameters) the effective coupling constant becomes smaller, so that one can approximate quark-quark scattering by the scattering of free particles. The QCD coupling constant α_s depends on the value of Q^2 according to

$$\alpha_s(Q^2) = \frac{12\pi}{(33-2n_f)\log(Q^2/\Lambda_{QCD}^2)} \tag{1.2}$$

where n_f is the number of active quark flavors, and Λ_{QCD} is a scale parameter approximately equal to 0.25 GeV. The exact definition of Q^2 one uses depends on the process one is studying. For example, we see from Figure 1b that in deep inelastic lepton-nucleon scattering that there is only one relevant Feynman diagram in the problem, and Q is simply the momentum transfer. On the other hand, we see in Figure 2 that high-p_T hadron scattering involves many different subprocesses, and it is not clear which combination of kinematic variables correspond to Q^2. One possible definition of Q^2 is the symmetric combination [8]

$$Q^2 = \frac{2\hat{s}\hat{t}\hat{u}}{\hat{s}^2 + \hat{t}^2 + \hat{u}^2} \tag{1.3}$$

where $\hat{s}$, $\hat{t}$, and $\hat{u}$ are the Mandelstam variables describing the parton scattering.

The variables $\hat{s}$, $\hat{t}$, and $\hat{u}$ are defined in terms of the four-momenta of the incoming and outgoing partons. Let us call the four-momenta of the partons in Figure 1a p_a, p_b, p_c, and p_d. Then we define the Mandelstam variables by

$$\begin{aligned} \hat{s} &= (p_a + p_b)^2 \\ \hat{t} &= (p_a - p_c)^2 \\ \hat{u} &= (p_a - p_d)^2 \end{aligned} \tag{1.4}$$

Another possible definition of Q^2 is

$$Q^2 = \hat{t}\hat{u}/\hat{s} \tag{1.5}$$

which is just q_T^2, the square of the transverse momentum acquired by each scattered parton.

Hard hadronic collisions exhibit a typical four jet structure. There are usually two roughly back-to-back high p_T jets, plus two low p_T jets resulting from fragmentation of the beam and target remnants. In addition, there is a diffuse background of particles due to initial and final state soft gluon radiation [9]. Observation of exactly this sort of structure has been dramatically seen in the recent CERN $Sp\bar{p}S$ Collider experiments [10]. At low $\sqrt{s}$, however, this jet structure is rather difficult to observe [11]. Instead, it is more profitable to study the relatively small rate of events, produced with typically a few % of the jet cross section, which result in a single leading high p_T hadron carrying most of the momentum of

the parent quark. One expects that this leading hadron in fact often contains the original scattered quark as one of its constituents.

The structure functions for nucleons can be derived from measurements of deep inelastic lepton-nucleon scattering. Several different parameterizations of these functions now exist [12-14].

The situation with regard to the fragmentation functions is less clear, although a relatively simple laboratory for studying the fragmentation process exists in e^+e^- annihilation experiments. The major problem is that the assumption that the scattered partons fragment independent of the remainder of the hadronic system is only approximately correct. Early independent fragmentation models, such as the well known Feynman-Field model [15-17], have recently been superseded by models which attempt to describe the whole event rather than treating the fragmenting parton in isolation [18-22].

The Lund model. One such model which has enjoyed a certain amount of success in describing the hadronization process is the Lund model [23-27]. The general idea of the Lund scheme is that quarks emerging from a hard collision are attached by a color flux tube, or string, to the other quarks involved in the collision. As the scattered quark moves away from the interaction region, the stretched string breaks in a number of

places. A quark-antiquark pair materialize at each point where the string has broken, and the system evolves to the point where one has a number of small strings, each string having a quark and antiquark at opposite ends. These quark-string-antiquark entities, which we observe as mesons, form a collimated jet of particles travelling in the direction of the original scattered quark. In addition to treating quarks as points at the end of the string, the model treats gluons as kinks in the middle of the string [25]. Finally, a simple model of baryon production is made by allowing diquark-antidiquark pairs to materialize at the ends of strings.

An attractive feature of the Lund model from the experimenter's point of view is that it is available in a well documented Monte Carlo program [28-29]. An experimenter can easily make his own theoretical calculations and directly compare his experimental results with Lund model predictions. An example of such a comparison is presented in Chapter 5, where we discuss the results of measurements of particle ratios at high p_T.

CHAPTER 2

Apparatus

Fermilab Experiment 605 was designed to measure high-p_T leptons and hadrons emerging from proton-nucleus collisions at both 400 GeV/c and 800 Gev/c. We describe below the experimental apparatus as configured in the run between January and July 1984. E605 is a collaboration of the State University of New York at Stony Brook, Columbia University, the University of Washington, Fermilab, CERN, CEN-Saclay, Kyoto University, and KEK.

Figure 3 shows the major components of the experimental apparatus. In the discussion that follows, we employ a right-handed coordinate system in which z points in the beam direction, y points up, and x completes a right-handed coordinate system.

Beam. Our experiment was situated at the end of the Meson-East beam line. Protons were accelerated in the Fermilab Main Ring and Energy Saver to 400 GeV/c momentum, and then extracted to the various experimental areas. Our experiment ran with a typical beam intensity of 4×10^{11} protons/spill. Each spill lasted about 12 seconds, and spills were delivered about once every 40 seconds. The protons within a spill were bunched

into "buckets", with each bucket lasting about 1 nanosecond and with an interval of 18.9 ns between buckets. Beam position was measured by a set of single wire ionization chambers (SWICS), which were remotely removed from the beam during data taking. Beam position at the target location was measured by taking target scans using our thin solid targets. Beam intensity was monitored by a Secondary Emissions Monitor (SEM), and the total SEM count for each spill was recorded on tape. Targeting was monitored by a four counter hodoscope (AMON) placed at 90 degrees relative to the beam direction at the z-position of the target. The size of the beam at the location of the target was .008 inches in the y-direction. The angular divergence of the beam was 60 μrad horizontally and 680μrad vertically.

Target. Two target holders were used. One was a device that held several small solid targets. These were made of beryllium, copper, and tungsten. A remote control switch allowed us to move any one of these targets into the beam. The other target system used, and the one for which data are described here, was an 8 inch long stainless steel flask which held either liquid hydrogen or liquid deuterium. The flask was cylindrical with a 2 inch diameter and had hemispherical endcaps. The walls of the entire flask were .001 inch thick. Surrounding the flask was an evacuated containment vessel with .001 inch thick stainless steel windows at either end. Data were taken with

liquid hydrogen and liquid deuterium targets, interspersed with empty target runs to measure background produced in the steel windows. The hydrogen target was measured via chemical analysis to be 99.999% pure H_2. The deuterium gas, however, was actually a mixture of 95% D_2 and 5% hydrogen deuteride (HD).

The resolution in p_T was estimated to be 3.0±0.2% rms, and was dominated by the effect of target length (2.6%) and the beam divergence (1.4%).

Magnets. Downstream of the target was a set of 3 dipole magnets, called SM0, SM12, and SM3, whose purpose was to sweep away low momentum charged particles and to measure the momentum of the high-p_T particles under investigation. These magnets were placed as shown in Figure 3. During the data run described here the magnets were all run with the same polarity. The direction of the magnetic field was in the negative x direction, causing positive particles to bend downward. The magnet currents were 2000A, 4000A, and 4200A for SM0, SM12, and SM3, respectively. During the last part of the liquid hydrogen running, the magnets were all run with reversed polarity in order to gain a better understanding of the difference in acceptance for positive and negative particles. The magnetic fields of all three magnets were measured with a flip coil.

Magnet inserts. A tungsten collimator oriented at ±36 milliradians production angle was placed at the entrance to SM12 as shown in Figure 4. The purpose of the collimator was to obstruct the passage of neutral particles into the magnet aperture. The previous test run of E605 had shown that neutral particles, particularly photons, provided a serious background, and the collimator was one of several steps taken to cut down this source of background. Another step taken was to insert tungsten-capped lead "teeth" along the top and bottom walls of SM12. These served to intercept photons and other particles and contain showering. Finally, a long copper beam dump was placed partway down the magnet. It served to intercept and absorb the uninteracted beam as well as any low transverse-momentum secondaries. These inserts proved to be largely successful in cutting down the neutral background; however, an effect we had to confront was the scattering of particles from the surface of the collimator. Charged particles scattering in this way could traverse paths similar to those of high-p_T particles emerging from the target, and many of our low threshold triggers were faked in this way. We were able to remove this background in the off-line analysis, as will be described in Chapter 4.

A variety of different types of particle detectors were arrayed at four z-positions called stations in order to collect tracking information. The types of detectors employed, as described below, were scintillation counter hodoscopes, multiwire proportional chambers, drift chambers, and proportional tubes. In addition, a calorimeter provided energy measurements for electrons and hadrons, and a ring imaging Cherenkov counter provided hadron identification.

Hodoscopes. Scintillation hodoscopes were placed at stations 1, 2, 3, and 4 in order to provide information for the fast trigger and as an aid in tracking. The locations of these hodoscope planes are as shown in Figure 5, and their specifications are presented in Table 2. The counters were constructed of Nuclear Enterprises NE110 plastic scintillator. Attached to one end of each counter was a Plexiglas light guide and Hamamatsu R329 photomultiplier tube. Signals from these phototubes were used in the fast trigger, as described in the next chapter.

Chambers. A set of 6 multiwire proportional chambers (MWPC) was placed at station 1, as shown in Figure 5. These planes measured the Y, U, and V coordinates of the particle trajectories, where U and V are oriented at angles $\pm\tan^{-1}(1/4)$ to the Y-axis. The MWPC gas was a mixture of 25% (82.6%Ar/17%CO_2/0.4%Freon) and 75% (50%Ar/50%Ethane) bubbled

through ethyl alcohol at 28°F. This particular mixture was chosen so as to allow chamber operation at high rates without discharge problems.

Stations 2 and 3 each had a set of 6 drift chamber planes, also measuring Y, U, and V coordinates. The chambers were operated with a 50% argon/50% ethane gas mixture and bubbled through ethyl alcohol.

A set of 3 proportional tube planes, measuring X and Y coordinates, was placed behind concrete absorbers at station 4. These tubes were used to identify muons, most hadrons having been absorbed in the calorimeter and following concrete and zinc absorber. These tubes were operated with the same argon/ethane/alcohol gas mixture.

A summary of the various chamber parameters is presented in Table 3 for the MWPC's and in Table 4 for the Drift Chambers.

Calorimeter. The electron-hadron calorimeter was located as shown in Figure 3. Its purpose was twofold: 1) to provide fast linear electron and hadron sums for the trigger logic, and 2) to identify particles as being either muons, electrons, or hadrons in the off-line analysis by measurement of the energy deposition in the various parts of the calorimeter. The calorimeter consisted of two major parts as shown in Figure 6: 1) an electron calorimeter, which was built of alternating layers of lead and scintillator for a total of 19 radiation lengths. It was read

out at 4 longitudinal positions. 2) A hadron calorimeter, built of alternating layers of iron and scintillator for a total of 9 absorption lengths. It was read out at 2 longitudinal positions. Both sections of the calorimeter were divided into a left and a right segment. In addition, the hadron part was segmented in the y-direction into 13 counters and the electron part into 12 counters. Further details regarding the calorimeter are found in reference [30].

Cherenkov Counter Description

Cherenkov Ring Imaging techniques. When a charged particle traverses a medium of index of refraction n with a velocity βc which is greater than the velocity of light in that medium (c/n), photons are emitted in a cone of angle θ_c with respect to the particle trajectory, where this angle is defined by

$$\cos \theta_c = \frac{1}{\beta n} \qquad (2.1)$$

These photons, when reflected from a spherical mirror with radius of curvature R, are focussed onto a ring in the focal plane, which is located a distance f=R/2 from the mirror. The radius of this ring is given by $r=f\tan\theta_c$. The center of the ring is

determined by the angle of the particle trajectory with respect to the optical axis of the mirror. Once the position of the ring center is determined, each detected photon gives an independent measurement of the ring radius. The particle mass, and thus its identity, is determined by combining the measurement of the ring radius with a momentum measurement (from tracking information). Ring radius, particle mass, and momentum are related by

$$r = f\sqrt{(n^2-1) - (m/p)^2} \qquad (2.2)$$

In the above equation we have made the approximations that the momentum and energy of the particle are the same, and that the index of refraction n is very close to 1. These are very good approximations for our experimental conditions, where we use a helium radiator with n=1.000038, and the Cherenkov threshold γ_t = 115. (This γ is just the ratio of particle energy to rest mass: γ=E/m.)

We note that in equation (2.2) and in a considerable part of the following discussion, we find it more convenient to use the quantity $\eta = n^2-1$. We call η the refractivity of the medium. Figure 7 shows the expected ring radii for π, K, and p as functions of momentum given an 8 meter focal length, and $n^2-1=75\times10^{-6}$.

The mean number of detected photons is given by [50]

$$N = \frac{\alpha}{hc} L \int \varepsilon(E) \sin^2\theta_c(E) dE \qquad (2.3)$$

where L is the radiator length, $\alpha/hc = 370\ cm^{-1}eV^{-1}$, and $\varepsilon(E)$ is the overall photon detection efficiency as a function of energy. The integral is evaluated over the range in which the photon detector is sensitive. The Cherenkov angle, θ_c, is also a function of photon energy, because the index of refraction varies with photon energy. This effect is known as chromatic dispersion.

The development of the Ring Imaging Cherenkov Counter was a major effort on the part of the E605 Collaboration [31-36]. We present here a full description of the various hardware components of the Cherenkov counter; in Chapter 4 we will describe the Cherenkov data analysis procedure.

An overall view of the Cherenkov detector is shown in Figure 8; the major parts consisted of the radiator vessel, purification system, mirrors, and photon detectors. We describe each of these parts in detail below.

Radiator vessel. The Cherenkov radiator vessel was an aluminum box 15.2 m long and measuring 3.1 x 2.8 m^2 in cross section at its downstream end. The walls were constructed from

3/32 inch aluminum sheet, except the upstream wall which was 1/32 inch. All joints were welded. Structural support was provided by an external network of I-beams and aluminum channels. The two detector ports were located on either side of the vessel, outside the experimental aperture.

Pure helium was used as the radiator gas. Helium has a very low refractivity ($n^2-1 = 75 \times 10^{-6}$ for 8 eV photons), enabling us to extend π/K separation to very high momenta. Helium also has a low chromatic dispersion in the vacuum ultraviolet, which is essential for achieving good spatial resolution in our photon detector. The radiator gas was maintained at room temperature (typically 60 °F, although we also operated the counter at a temperature as low as 45°F) and at a pressure of about 1.02 atmospheres. The vessel was wrapped in thermal insulation in an effort to keep the interior of the vessel at a uniform temperature. Since the refractivity of a gas is inversely proportional to the temperature, a degrading of ring radius resolution would have resulted if the temperature within the radiator vessel were not uniform to within 1-2 degrees C.

Purification system. The purification system is shown in Figure 8. Its purpose was to conserve helium usage, remove impurities from the gas, and to measure the transmission of ultraviolet light in the gas.

Helium was introduced into the vessel using boiloff from a liquid helium dewar. Automatically operated valves controlled gas flow, maintaining the vessel at a pressure of 5-10 inches of water above atmospheric pressure.

Gas was recirculated first into a 12 m long control tube, which was used to measure the gas transmission. A 8 eV light source [34], placed at one end of the tube, was directed towards a UV-sensitive phototube at the other end of the control tube. The gas transmission was measured by comparing the phototube readings when the control tube was evacuated to when it was full. The transmission was found to be 75-80% during the run.

Oxygen was removed from the radiator gas by mixing it with a small amount of hydrogen and combining them to form water in a Deoxo Catalyzer. The water was then removed in a dryer, while other contaminants and any remaining water were frozen out in a liquid nitrogen trap. Clean helium gas was then pumped back into the radiator vessel. Care needed to be taken to monitor the level of excess uncombined H_2 gas, which, due to its low boiling point, could not be frozen out in the LN_2 trap. By virtue of its large refractivity ($n^2-1 = 450 \times 10^{-6}$) [55], the concentration of H_2 gas in the radiator could be measured from the size of the observed Cherenkov ring radii. The vessel was purged once during the course of the 800 GeV run with pure helium when the H_2 concentration reached 2%. Higher levels of H_2 could not be

tolerated, because its high chromatic dispersion would have adversely affected photon resolution.

Mirrors. An array of 16 mirrors was placed near the downstream end of the radiator vessel, as shown in Figure 8. Each mirror measured 25 X 26 inch^2 in area, and was ground from 7/8 inch thick plate glass into a spherical surface with a 16 m radius of curvature. Use of such a large thickness of glass had the drawback of introducing approximately 0.2 radiation lengths of material into the aperture. However, it was considered impractical to manufacture thinner mirrors that were sufficiently rigid to maintain the required optical qualities. A thin layer of aluminum was deposited on the mirror surface, and covered by a layer of MgF_2. The reflectivity of the mirrors was measured to be about 75% at 1500 A. The mirrors were produced by the Muffoletto Optical Company of Baltimore, MD [53].

The mirrors were mounted in a large rectangular aluminum frame. The weight of the mirrors was supported by steel wires, running vertically and suspended from the frame. Each mirror was held in its own aluminum frame, and supported at three point by viton cushions. Three independently adjustable threaded rods were connected to each mirror frame, allowing each mirror to be independently oriented.

Mirror alignment. The mirrors were aligned so that 2 columns of mirrors (8 mirrors) pointed at one detector, and the other 2 columns pointed to the other detector. Alignment angles were chosen so as to minimize the detector area required to observe photons emitted by all tracks within the experimental aperture. Rather than aligning the mirrors so that they all lay on a spherical surface, they were deliberately "defocussed". What this means is that the rings from adjacent mirrors were well separated on the detector plane and were non-overlapping. This was done so that we could always identify from which mirror a given photon was reflected. This feature proved very useful in the data analysis.

The mirrors were aligned using a point light source placed at a specific point in the detector plane. A grid containing the outline of each mirror's reflection by the light source was taped to the upstream wall of the vessel. The mirrors were finely adjusted until their projections fit into their respective "boxes" on the grid. Using this method, we aligned every mirror to within ±10 mm in image position in the detector plane. A more accurate measurement of the mirror alignment angles was performed using the data itself, as will be described in the next chapter.

Calcium fluoride window. The window separating the radiator gas from the detector gas was a 4 x 8 array of 10 x 10 cm^2 CaF_2 crystals glued to a brass frame. Each crystal was 4 mm thick and

had a transmission of about 70% at 8 eV, with a high-energy cutoff at 9.2 eV. The particular frame and glue used were chosen because their thermal expansion characteristics were similar to those of CaF_2. [36]

Photon detectors. Each of the two photon detectors was a multistep proportional chamber of the type described in references [35-36]. The active area of each chamber was 40 x 80 cm^2. A schematic diagram of the chamber is shown in Figure 9. The chamber was operated with a He(97%)/TEA(3%) gas mixture. The photosensitive gas triethylamine (TEA) has an ionization potential of 7.5 eV, and a 3% mixture of TEA in helium has an absorption length of about 1 mm for photons above this energy and less than 9.2 eV. The chamber operated as follows: a photon crossing the CaF_2 window enters the conversion gap, a region of low electric field (100 volts/mm). Here the photon ionizes a TEA molecule producing a single photoelectron. This electron drifts into the pre-amplification gap, where there is a high electric field (750 volts/mm). Here the electron avalanches, multiplying by a factor of 10^4. A portion of this avalanche is transferred through the transfer gap to the last stage of the chamber, a proportional wire chamber (2 cathode wire planes and 1 anode plane). The electron avalanche multiplies and collects on an anode wire for a total gain of about 10^7. Induced charges are recorded on each cathode plane; typically, the induced pulse is spread over 5-6 cathode wires.

The proportional chamber planes consisted of wires spaced every 1 mm. Each adjacent pair of wires was ganged together before being read out into the preamplifier cards, so from the electronics point of view the chamber was segmented into channels spaced every 2 mm. Anode wires ran vertically, and cathode wires (u and v coordinates) were oriented at ±45 degrees. We note that the u and v coordinates in the Cherenkov counter are not the same as the u and v coordinates in the MWPC's and drift chambers. There were a total of 192 anode channels and 2 x 384 cathode channels.

CHAPTER 3

Data Acquisition

In this chapter we describe the method used to acquire data from the experiment. In particular, we discuss the trigger logic and the readout system.

Trigger Logic. Signals from the phototubes attached to the scintillation hodoscopes described in the previous chapter were sent to LeCroy Model 4416 ECL Discriminators. The high voltages on the phototubes were adjusted so that minimum ionizing particles produced 60 mv pulses. We then set the thresholds on the discriminators to 30 mv. Their output pulses were set to approximately 12 nanoseconds width. The pulses from the phototubes were not synchronized; that is, the light from a particle that hits a hodoscope counter close to the phototube will arrive at the phototube earlier than the light from a particle hitting at the far end. This time jitter is as large as 10 ns for the longest counters (X4). The trigger logic electronics demanded that the pulses in a given bucket be synchronized and this was achieved by sending the output from the discriminators into the University of Washington pulse stretcher modules. These pulse stretchers were gated by the accelerator RF

signal, which was a sine wave with a period equal to the time between buckets. The pulse stretchers synchronized the discriminator pulses to the RF signal. Synchronization of the pulses by the stretcher modules allowed us to achieve one bucket time resolution in the trigger logic. The output signals of the pulse stretchers were then fanned out to several places: 1) Each channel was sent to a coincidence register card setting a bit which was read out into the data stream if the event caused a trigger. 2) Each channel was sent to one or more trigger matrix modules. 3) Each half-bank of counters (left and right halves of each bank) was sent to a hodoscope terminator module, where the logical OR of the half-bank was performed.

Trigger Matrix

Matrix system components. The trigger matrix system was essentially a fast lookup table that provided a set of outputs according to whether any among a possible set of "roads", or combinations of counters, were satisfied. A block diagram of the matrix system is shown in Figure 10, and simplified schematic of a matrix card is shown in Figure 11.

A total of 8 trigger matrices were employed in the experiment, divided into two large groups called the Y Matrices and the Muon Matrices. Both operated in similar ways, their major operational difference being their inputs: for the Y

Matrices, information was input from hodoscope counter banks Y1, Y2, and Y3; the Muon Matrices used input from Y1, Y2, and Y4. Each group of matrices was further subdivided into quadrants: Up-Left, Down-Left, Up-Right, and Down-Right. An Up matrix triggered on tracks that went over the beam dump (positively charged particles), while a Down matrix triggered on tracks passing below the dump (negatives). Left and right simply refer to left and right halves of the apparatus as seen by an incident proton. Each quadrant, hereafter simply referred to as a matrix, produced a single logical output: true, if any combination of 3 counters, one from each bank, matched an entry in the lookup table, and false if otherwise.

Matrix hardware description. Each trigger matrix was composed of 4 modules, or printed circuit cards. Three of these cards, called "matrix modules", were identical; the fourth card, called a "terminator module", was used to collect information from the 3 matrix modules and logically OR them to produce a single logical NIM output.

Each matrix module was essentially a 12 x 8 x 4 lookup table. The lookup table information for each module was loaded into six 256 x 4-bit Random Access Memory (RAM) integrated circuit chips, Fujitsu Model MB7072 [54]. These RAMs operated via emitter-coupled logic (ECL), had 8 Address inputs and 4 output bits, and had a cycle time of 12 ns. They were programmed

via the on-line PDP 11/45 computer through the CAMAC system. Input to each RAM were 4 counters from one hodoscope bank, and 4 counters from a second bank. The output bits of each chip corresponded to the allowed set of counters in the third bank which completed correct matrix combinations. These output bits were then logically ANDed with the actual set of third hodoscope plane hits to form the matrix module output.

Matrix software. One of the most significant features of the trigger matrix system was that all combinations of hodoscope hits were checked simultaneously, providing for the greatest possible speed. To achieve this, every possible combination of 4 x 4 arrays of counters had to be programmed into each RAM. The steps required to load the matrix with a given pattern are described as follows:

First, a physically reasonable trigger matrix pattern had to be generated, consisting of a subset of all possible roads traversed by particles emerging from the target. This was done via a Monte Carlo program. This program produced a set of matrix maps corresponding to the set of allowed hodoscope roads for a given set of magnet currents. These maps were further edited by hand to add or remove individual matrix combinations. For example, "hot cells", or matrix combinations satisfied by uninteresting beamlike particles, were removed at this stage. These maps then had to be transformed, via a program called

TRMAT, into a compact table of values describing the information to be loaded into each RAM chip. Program TRMAT read a file containing the matrix hardware map, which described all the necessary data pertaining to every RAM in the matrix system, namely, its location (CAMAC crate and station number, and module subaddress) and the particular combination of hodoscope inputs (a set of 4 x 4 x 4 counters) treated by that RAM. TRMAT then generated a disk file containing the loading pattern for all the RAMs. A number of such files, corresponding to different magnet settings and running conditions, were generated. The experimenter selected which matrix file he wished to load at the beginning of a data run. The final step was performed by the on-line program, which read the matrix table disk file selected by the user and issued the appropriate instructions required to load the matrix. The loading process was performed via a JORWAY Branch Driver and branch highway. This loading process was performed about once every 5 to 10 runs, and took about one minute to execute. In addition, while a data run was in progress, the PDP read back and checked the contents of each RAM periodically and notified the experimenters if any errors had been detected.

Calorimeter logic. We utilized pulse height information from the calorimeter to provide a number of trigger logic signals. To do this, we first produced analog sums of the pulse

heights from the phototubes in various sections of the calorimeter. Four of these sums, called EUL, EUR, EDL, and EDR, were created by summing pulse heights from either the Left(L) or Right(R) halves of the calorimeter, while restricting the sum to either the upper(U) or lower(D, for down) 9 counters in that half. For example, EUL summed the upper 9 counters on the left side. The four signals EUL, EUR, EDL, and EDR were then all attenuated by the same factor and discriminated, thereby converting analog signals to logical levels.

In addition to the above, we also made the logical signals ETFI and EHI. Both ETFI and EHI summed the pulse height over the entire calorimeter, but were then attenuated by different factors before being discriminated. We set the attenuation factor of EHI higher than ETFI, and EUL, EUR, EDL, and EDR midway between ETFI and EHI. These attenuation factors were changed during the run a number of times to account for different running conditions, and are listed in Table 5. All of the above signals were made by summing over both the electron and hadron parts of the calorimeter.

The motivation for these signals was as follows: ETFI was set to a low attenuation level for use primarily as a study trigger in evaluating the calorimeter trigger efficiency. The signals EUL, EUR, EDL, and EDR were used as inputs to those triggers requiring both a calorimeter energy deposit and a

hodoscope road satisfying the trigger matrix. EHI was designed as a simple, high energy calorimeter (~100 GeV) trigger, regardless of the presence of hodoscope roads.

DC Logic. A block diagram of the DC Logic system is shown in Figure 12. The DC Logic is a flexible system allowing for the simultaneous generation of up to 16 different triggers. Inputs to the DC Logic are provided to two places, the Trigger Fan-In (TFI) Module, and the DC Logic Bus.

The purpose of the TFI module is to generate a start signal for the DC Logic. When the DC Logic receives such a signal, it latches the signals on the DC Logic Bus, creating a set of DC logic levels which are then processed. The TFI generates a start signal whenever any of its inputs are present in the logical true state. We used two inputs to the TFI, called ETFIL and ETFIR. To make ETFIL, we first performed majority logic (3 out of 4) on the hodoscope banks X1L, Y2L, X3L, and Y3L; then we defined the coincidence of this signal with the ETFI signal from the calorimeter logic as ETFIL. ETFIR was done in a similar way using the right-hand hodoscope banks.

The bits on the DC Logic Bus were drawn from the Trigger Matrix outputs and the calorimeter logic. To simplify the trigger logic, we reduced the four Trigger Matrix outputs (YUL,YUR, YDL, YDR) to two by performing the logical OR's of corresponding left and right outputs. We made YU=YUL.or.YUR and

YD=YDL.or.YDR and used these two signals as inputs to the DC Logic Bus. Similarly, we made the corresponding calorimeter signals EU=EUL.or.EUR and ED=EDL.or.EDR and input these to the Logic Bus. Finally, the two remaining calorimeter signals ETFI and EHI were input to the Bus without further modification.

Once the DC Logic has received a start signal from the TFI module and latched the inputs on the Logic Bus, it then performs logical operations on these inputs via the Pin Logic Modules, which are hardware programmable (via switches) printed circuit cards. We created the following hadron trigger bits in the Pin Logic Modules: EYU=YU·EU, EYD=YD·ED, EHI, and ETFI. ETFI was prescaled by a factor of 64. All of these trigger bits were then input to the Trigger Store Module, which performed the logical OR of these inputs to provide the final trigger. This final trigger caused the Trigger Generator Output (TGO) Module to generate readout gates for the event.

Readout system. The event was read out by the Nevis Transport System [37]. The Transport system was a communications system between the data acquisition electronics, the on-line computer, and the readout buffer (Megamemory). Its purpose was to supervise the readout of each event in an orderly fashion. This readout order was: 1) The trigger bits, namely, all bits from the DC Logic Input Bus, the TFI module, and the TGO module, were read out by coincidence register (CR) cards through

Transport. 2) Hodoscope hits, MWPC hits from from station 1, and prop tube hits from station 4 were read out from other CR cards through Transport. Data compression was performed on the CR cards prior to readout; that is, only those channels having nonzero data were read out. 3) Drift chamber hits and drift times were recorded by Time to Digital Converters (TDCs) and then compressed and read out through Transport. 4) Calorimeter pulse height information was recorded and digitized on Nevis Quadratic Analog to Digital Converters (ADCs) and read out. 5) Cherenkov pulse height information was recorded on Saclay and LeCroy ADCs, as described in detail below. All the above information was organized by the Transport system, which inserted identifying header words before each block of data and a word count at the end of each block. The event was stored in the event readout buffer, the University of Washington Megamemory, a 4-megabyte memory appended to the on-line PDP [56]. The readout process took about 10-40 μsec to perform, depending on the event length. During the course of a typical spill, approximately 1000 events consisting of several hundred data words each were sequentially stored in the megamemory. At the conclusion of the spill, the PDP dumped the entire megamemory contents onto 6250-bpi tape. One tape typically was sufficient to record about 100,000 events. The readout system had a very high rate capability, (of order 10 kHz) due to the fact that most of the readout procedure could be performed without any assistance from the on-line computer.

Cherenkov ADC systems. Two ADC systems were employed for performing analog-to-digital conversion of Cherenkov pulse height information. The east chamber used ADCs built for CERN by LeCroy (Model 4200 Fast-Encoding Readout ADCs (FERA), now commercially available). These were 10-bit linear ADC's. The west chamber used ADCs built by the Saclay electronics group, and were 7-bit bilinear ADC's. Both systems performed automatic pedestal subtraction and data compression. This was the first utilization of either system in an experiment, and both proved to be fairly successful.

Collection of data. A summary of the data collected with the liquid hydrogen and deuterium targets is presented in Table 6, where we list the number of protons on target for each target type, as well as the empty target running. In addition, the table also shows the total integrated luminosities. We recorded 200-500 triggers in a typical spill, and each data tape was sufficient to record 80-100 k triggers. We recorded a total of 22 data tapes for the hydrogen target and 35 tapes for the deuterium target.

During the data taking, the on-line PDP computer routinely transferred a portion of the data to our VAX 11/780 computer for monitoring purposes. We ran a program on the VAX that was rather similar to the program used in the main off-line analysis. Its purpose was to check that all parts of the apparatus were

functioning properly. For example, we periodically checked the performance of the Cherenkov chambers by reconstructing photons on the VAX. Chamber voltages were readjusted if we saw that the pulse heights were either too high or too low.

Figure 13 shows the on-line display of the data from one chamber for a typical event as generated by our VAX program. On the left and right sides of the figure we see the histograms of the raw pulse heights of the u and v cathode planes; at the top of the figure is the anode pulse height histogram. The rectangular box represents the 40 x 80 cm^2 chamber area. Within the chamber we see the anode and cathode coordinates as reconstructed by the program, represented by the vertical lines for the anodes and the lines running at $\pm 45^\circ$ for the cathodes. The '+' sign shows the expected location of the ring center, with a circle drawn about it at a radius of 70 mm. The '*' symbols are drawn at the triple intersection of an anode and two cathode coordinates, and represent the locations of the photons which have been reconstructed by the program.

Cherenkov sparking. During the course of the data taking we addressed a number of problems regarding the Cherenkov chambers. The major hardware problem we encountered was that of sparking. Both chambers sparked across their pre-amplification (PA) gaps during spills, with a sparking rate proportional to beam intensity. Following a spark, the chamber required typically

10-50 milliseconds for the electric field in the PA gap to return to its normal value, and during this time there was no amplification of photoelectrons and hence no detection of photons.

While one possible solution would have been to reduce the field in the PA gap, doing so was shown to result in very low pulse heights in the proportional chamber, and therefore poor photon reconstruction efficiency. We therefore kept the electric fields high, tolerating a sparking rate of 10-20 Hz. To monitor the sparking, we set up two logic bits, one for each chamber. Whenever a spark occurred, which we detected by monitoring the PA gap voltage, we set the spark bit and left it gated on for 50 milliseconds. These bits were read out with each event, and in this way we knew the chamber status for each event. Analysis of these events is described in the next chapter.

CHAPTER 4

Data Analysis

In this chapter we describe the methods used to extract the hadron cross sections and ratios from the raw data. Particular emphasis is placed on the procedures used to perform particle identification.

Event analysis; tracking. There were three major parts in the analysis of each event. The first part consisted of using the information from the drift chambers and MWPC's to find tracks. The second part traced the particle trajectory back through the SM12 and SM0 analysis magnets to the target position. In the third part, hadron identification was performed using data from the ring-imaging Cherenkov counter.

The data tapes were analyzed using the CDC Cybers installed at Fermilab. Because of memory limitations and CPU-time considerations, the analysis of each tape was broken up into two distinct jobs. The first job compressed a raw data tape into a 1st pass data summary tape (DST-1). If an event satisfied any of the hadron triggers as discussed in the previous chapter (these were EHI, EYU, EYD, and ETFI), it was analyzed for tracks. The tracking program, JACTRACK [37-38], worked as follows: first, the

drift chambers in stations 2 and 3 were searched for sets of y-u-v triplets. These triplets were required to contain at least one associated pair of hits (e.g., y and y'), with a consistency check being required on the sum of the drift times. After all triplets are found, a search for doublets (2 associated hits in either y-u-v) which are not subsets of the previously found triplets. These triplets and doublets were required to be consistent with a track pointing to an energy deposition cluster in the hadron calorimeter. The tracker then looped over all combinations of station 2 and 3 doublets and triplets and made a list of all track candidates which were consistent with a track emerging from the target. This required that the track point toward the target in the non-bend x view. The tracker also made checksum cuts on all track candidates, requiring that the sum of the drift times in associated hits be consistent with the measured track angle.

Each of the drift chamber track candidates which survived the above cuts was then checked to see if it could be matched with a track segment in the station 1 MWPC's. For each track, a minimum of 4 chamber hits was required in each of stations 2 and 3 (out of 6 hits maximum per station), and a minimum of 3 hits were required in station 1. Typical chamber efficiencies were between 85-95%. Drift chamber efficiency was uniform as a function of drift time, except for the region very near the field

wires, where the efficiency dropped to 65-85%, depending on the chamber. The overall tracking efficiency, as calculated using the individual chamber efficiencies, was estimated to be about 96% for a typical run.

Traceback. Any event satisfying a hadron trigger was written to DST-1, along with tracking information and momentum, which was calculated using the measured field in SM3. A second pass was then made on the data tapes, in which traceback to the target and Cherenkov analysis were performed. The traceback procedure, FLIPSWIM [39], worked as follows: Magnets SM0 and SM12 were divided into a number of 18 inch long sub-magnets. Starting with the known track direction and position at station 1, the particle was traced to the effective bendplane of each submagnet, where a p_T kick was calculated from the magnetic field map. This procedure continued through all the sub-magnets, unless the particle track was rejected for hitting a point outside the open aperture. When the track had been traced to the z-position of the target (z=-130 inches), the initial p_T and θ (polar angle) of the track were calculated, provided the track satisfied the target constraint cuts $|x_{tgt}|<0.6$ inches and $|y_{tgt}|<1.2$ inches. In this phase of the analysis, a large number of background events were rejected, mainly because these events originated from sources other than the target. The details of the number of events passing each stage of the above analysis are presented in

Table 7. In the Table, 'N triggers' gives the number of events we analyzed for each trigger type. 'N tracks' gives the number of triggers for which tracks were reconstructed. We see that EYU and EYD have a higher fraction of tracks reconstructed than for EHI. This is because EYU and EYD both required Trigger Matrix roads to be satisfied. 'N target' gives the number of tracks which were succesfully traced back to the target position. We note that most of the surviving events are EHI triggers. This is because it was relatively easy for a secondary hadron emerging from the collimator to fake a high p_T track (satisfying the Trigger Matrix) and to pass the low threshold EU and ED calorimeter triggers. These background tracks had a more difficult time satisfying the higher energy threshold EHI trigger. The number of events in parentheses in the 'N ovl' rows indicate the number of EYU and EYD triggers which simultaneously satisfied the EHI trigger.

In Table 8 we list the number of events passing a further set of cuts which were imposed following the traceback analysis and before the Cherenkov analysis.

Calorimeter analysis. The calorimeter was used in the analysis of the hadron data for two purposes: 1) to reject leptons, and 2) as an aid in tracking by requiring a hadron track to point to an energy deposit cluster in the calorimeter. A cluster is defined as a set of adjacent counters (typically 2-3 counters) which have recorded an ADC pulse height above pedestal.

The charge as measured by the calorimeter ADC's must first be converted to an energy measurement. This was done for each counter by comparing the collected charge to the momentum of each track passing through that counter. For high momentum particles we can make the approximation that the energy deposit is equal to the momentum. In order to relate energy to charge deposited we first correct the charge deposited for the attenuation of light along the length of the counters. That is, we collect less light from a particle which hits the calorimeter at a position far from the phototubes than we collect from a particle which deposits the same energy but hits near the phototubes. After this correction is made, the histogram of the ratio of collected charge to particle momentum is approximately gaussian in shape. The rms width of this gaussian is the energy resolution of the calorimeter ($\delta E/E = 75\%/\sqrt{E}$). The peak value is chosen as the scale factor converting charge to energy. This value is, in general, different for each counter.

We required a minimum of 30 GeV per cluster in order to reject muons. Muons fail this requirement because they will leave only a minimum ionizing deposit of about 5 GeV on average. Electrons and hadrons can be distinguished by the longitudinal development of their showers. Electrons interact with a heavy atom (such as lead) via bremsstrahlung, which creates an electromagnetic shower. This shower develops very quickly, and

electrons deposit most of their energy in the first few modules of the calorimeter (i.e., in the EM portion). Hadrons, on the other hand, begin to shower after they experience an inelastic collision with a heavy nucleus, and for materials containing heavy nuclei, the nuclear interaction length is longer than the radiation length. Hadronic showers will thus take longer to develop and are spread over a greater longitudinal distance than electromagnetic showers. In the case of our calorimeter, we expect most hadrons to deposit a significant part of their energy in the last two modules (i.e., the hadronic portion). We made the requirement that hadrons deposit less than 90% of their energy in the EM portion of the calorimeter. Any particle depositing more than this fraction was considered to be an electron. The fraction of hadrons lost by this requirement was estimated to be about 0.5%.

Analysis of Cherenkov data.

Analysis of the Cherenkov data for a given event was performed only for those events surviving the tracking and traceback analysis. Having determined via the calorimeter that these events were hadrons, the Cherenkov counter was required to identify the particular species of hadron. The Cherenkov analysis was performed by the CERKOV patch of the main analysis program and operated in the following way:

Calculation of ring centers. Cherenkov photons emitted along the path of a particle traversing the Cherenkov radiator vessel may strike one or more mirrors and be reflected onto one or both photon detectors, producing one or more ring images. These rings each have a center which is defined by reflecting the particle trajectory off each relevant mirror and onto the appropriate detector as if this trajectory were the path being taken by a photon. These ring centers were used as reference points in the subsequent analysis for calculating ring radii. For each track, a ring center was calculated for every mirror that could conceivably intercept photons from that track. While geometrical aberrations introduced by the apparatus distort the rings from perfect circularity, the ring "radius" is defined for each photon as being equal to the distance from the measured photon position to the nearest calculated ring center. The non-overlapping of ring images from neighboring mirrors allowed us to measure ring radii unambiguously.

Calculation of u, v, and x cluster coordinates. Both cathode planes and the anode plane of each chamber were scanned for clusters, or groups of adjacent wires having a pulse height greater than a certain threshold. For simple clusters, which are clusters having only one maximum, the coordinate is calculated by a center of gravity method. The amplitude, or pulse height summed over all the channels in a cluster, is stored for each

cluster. Multiple clusters, which have more than one peak, are divided at the minimum points into separate clusters. Single low or high channels in the cathode planes are ignored when searching for maxima and minima, but no attempt at smoothing is done, except in those cases where individual channels are dead, in which case they are set equal to the average of neighboring channels. There were never more than five dead channels during any run, and they were often repaired soon after being discovered by the monitoring program.

A masking procedure was employed to prevent spurious coordinates from being considered in the analysis. The requirement was that each cluster coordinate must lie within 100 mm of any calculated ring center. If there were no ring centers for a given detector in a particular event, the data from that detector was simply not analyzed. A maximum of 20 cluster coordinates from each wire plane was allowed, after masking, and if that number was exceeded, the event was cut as being too noisy to analyze correctly. The number of these overflow events was less than 0.5% of the data. We have no reason to believe there was any bias in these overflow events with regard to particle type.

Finding photon candidates. The list of cluster coordinates in the u, v, and x planes were searched for triplets. Candidates were accepted with the following criteria: 1) the x-projection

calculated from the u and v coordinates must be within 2 mm of the x- coordinate. 2) The amplitude correlation between all three planes must be sufficiently good. The amplitude correlation factor was calculated according to

$$W_{uv} = \frac{A_u + A_v - |A_u - A_v|}{A_u + A_v} \qquad (4.1)$$

where A_u and A_v are the u and v amplitudes. The above function was constructed so that its range was $0 \leq W_{uv} \leq 1$, and so that $W_{uv}=1$ for perfect correlation ($A_u=A_v$). It was required that $W_{uv} \geq 0.5$ for a candidate point to be accepted. Similarly, a cathode-anode correlation function

$$W_{uvx} = \frac{A_{uv} + A_x - |A_{uv} - A_x|}{A_{uv} + A_x} \qquad (4.2)$$

was constructed, where A_x was the anode amplitude and A_{uv} was the sum of the cathode amplitudes. We also required $W_{uvx} \geq 0.5$ for a good candidate point.

Any u-v-x triplet satisfying the above criteria was stored in the list of candidates. A maximum of 100 candidates were allowed. This situation occured, with subsequent event rejection, in only 0.1% of the events. The candidates were then ordered, with the candidates having the best amplitude correlation being placed at the top of the list.

Selecting a subset of candidates as the solution. The candidate list was searched for the best possible subset of candidates. Starting with the candidate point with the best amplitude correlation, and working down the list, each candidate is assigned to the "solution list" if the following criteria are met: 1) The candidate does not share any of its u, v, and x coordinates with a candidate already in the list. 2) Failing the above, an attempt to "split" a shared coordinate was made. The amplitude for this shared coordinate was divided among the two candidates in such a way that both candidates still satisfied the amplitude correlation criteria. If it was possible to do this, the candidate was added to the list. This procedure attempted to recover from the fairly common situation in which cathode pulses in either the u- or v- view overlapped. Such an overlapping was less common in the anode plane, since pulses in the anodes were in general only one channel wide.

After the solution list was generated according to the above procedure, a "quality factor" was calculated. This was defined as the fraction of the total available amplitude (summed over all three coordinate planes) actually used by the candidates. For example, if there was a cathode cluster which was not associated with any of the candidate points in the solution list, then the quality factor for this solution would be less than 1.

Following the construction of the initial solution list, an attempt was made to improve the quality factor of the list by either rejecting or adding candidates to the list. We rejected a candidate from the list if its amplitude correlation was the lowest of any candidate in the list and if it had at least one shared coordinate. We added a candidate to the list if it had the highest amplitude correlation of any candidate not already in the list and shared at most one coordinate with any of the candidates in the list. Each time the solution list was changed (either by rejecting or adding a candidate) a new quality factor was calculated. This procedure stopped when: 1) 100 iterations of the above procedure had been performed. (This never happened). 2) A solution that was identical to a previously tried solution was constructed. 3) It was impossible to either reject or add a candidate. When this happened, the solution list having the highest quality factor was chosen as the best solution. Typically, this procedure required less than 10

iterations, and ended with a solution having a quality factor of greater than 95%.

Calculating photon positions. The final list of candidates was used to calculate the photon x and y coordinates. For photons whose u-v-x clusters were not shared by other photons, this calculation was straightforward; for photons containing a single shared coordinate, the other two non-ambiguous coordinates were used to calculate the photon position. A maximum of 20 photons were allowed from each detector, but we never encountered an event having more than 15 photons in a chamber.

Radius calculation. Each photon was assigned to a Cherenkov ring and its radius calculated. The correction for spherical aberrations was applied at this stage, and was done in the following way: a "model photon" was emitted from the particle trajectory at a point approximately halfway down the Cherenkov radiator, at an azimuthal angle equal to that of the real photon, but at a polar angle θ_c equal to the maximum allowed Cherenkov angle. This photon corresponded to one emitted by a particle travelling with velocity $\beta = 1$. This photon was then traced to the appropriate mirror and then reflected onto the detector surface. Its radius was measured and the reduced radius, defined as the radius of the real photon divided by the radius of the model photon, was calculated. The reduced radius is a quantity which is corrected for spherical aberration effects. For a given

particle type, one expects the reduced radius to depend only on the particle momentum and the index of refraction of the medium.

While it is true that the expected value of the reduced radius is independent of a large number of factors, the standard deviation of the distribution of real photons is not independent of these factors. We calculated the error in the expected value of the reduced radius for each photon, taking into account the chromatic dispersion of the radiator, astigmatism (uncorrectable spherical aberrations due to uncertainty in the emission point of the photon), the momentum resolution of the track, errors in mirror alignment, and the intrinsic resolution of the chamber. We measured the single photon resolution using very high momentum (>100 GeV/c) muon tracks and found it to be 1.2 mm rms, as shown in Figure 14. Chromatic dispersion was the single most important contribution to the resolution, accounting for 0.75 mm, and is about the value one expects when using a 99%He/1%H_2 mixture as the radiator gas.

Particle identification. At this point we tested the combined list of reconstructed photons and their radii against each of the particle hypotheses π, K, and p. We assumed that each photon was either a real Cherenkov photon or a random photon produced by other means such as scintillation. We measured the mean number of random photons (those photons not lying near a Cherenkov ring but within the 100 mm mask) to be about 1.1 for a typical event.

For each particle hypothesis, we initially calculate the sum of χ^2, where

$$\chi^2 = \sum \frac{(r_i - \rho_j)^2}{\sigma_{ij}^2} \qquad (4.3)$$

This sum is carried out over all photons. In this equation, r_i is the measured photon reduced radius, ρ_j is the expected value of the reduced radius for particle type j, and σ_{ij} is the standard deviation of the predicted distribution of radii about ρ_j. The values of σ_{ij} vary from photon to photon primarily because the effect of uncorrectable astigmatism is sensitive to the photon's azimuthal angle ϕ. Also, σ_{ij} depends on particle hypothesis due to the uncertainty in particle momentum. For protons slightly above threshold, the ring radius changes rapidly with momentum, and σ_{ij} is large (e.g., σ_{ij}=6.0 mm at 120 GeV/c typically). On the other hand, the ring radius for π's is practically insensitive to momentum and σ_{ij} is typically 1.2 mm.

After calculating χ^2, we then calculate a confidence level for this value of χ^2 and n degrees of freedom (corresponding to n photons) [52]

$$C.L.(\chi^2,n) = \frac{1}{2^{n/2}\Gamma(n/2)} \int_{\chi^2}^{\infty} y^{\frac{1}{2}(n-2)} e^{-y/2} dy \qquad (4.4)$$

where $\Gamma(n)$ is the usual Gamma function:

$$\Gamma(n) = \int_0^{\infty} t^{n-1} e^{-t} dt \qquad (4.5)$$

We then attempt to improve this confidence level by rejecting the photon having the worst χ^2 and assigning it to the random photon category. The probability for a random photon to lie within a distance Δr of a Cherenkov ring of radius r is given by

$$P(\Delta r) = \frac{\pi\left[(r+\Delta r)^2 - (r-\Delta r)^2\right]}{A} \cdot P(A) = \frac{P(A)}{A} \cdot 4\pi r \Delta r \qquad (4.6)$$

where P(A) is the probability for a random photon to lie within an area A. We measured $P(A)=25\pm5\%$ for an area $A=10^4$ mm^2 by measuring the number of photons lying outside the Cherenkov ring. The next step is to recalculate the confidence level for this

hypothesis by calculating χ^2 for n-1 good photons and folding in the probability of seeing 1 random photon. If this new confidence level is less than the previously calculated value, we stop and call the higher confidence level the probability for particle hypothesis j to be correct.

On the other hand, if we find that rejecting a photon improves the confidence level, we continue in an iterative process to reject the photons with the worst χ^2 and recalculate the confidence level. We continue until we reach a solution with n good photons and m rejected photons such that the confidence level is maximized, and we call this value the probability for particle hypothesis j to be correct. If we reject all photons, we reject this particle hypothesis and assign a probability of zero.

The above procedure is repeated for each of the three particle hypotheses π, K, and p and a probability assigned to each. We then decide the particle identity on the basis of the hypothesis having the highest probability. In most cases, all but one of the hypotheses will be rejected and particle identification is unambiguous.

There are two ways for the particle to be assigned to a category other than π, K, and p: 1) There are no reconstructed photons in the event. We assign the particle to the "No Photons" category. 2) We do reconstruct photons, but the probability for

all photons to be random is greater than any of the probabilities for the particle to be π, K, or p. In this case we assign the particle to the "ambiguous" category. The number of such ambiguous events is about 10-12% of the number of zero photon events, and is consistent with the number of zero photon events expected to contain random photons.

A particle identification summary for the hydrogen and deuterium data is presented in Table 9.

Systematic radius corrections. Corrections to the reduced radius measurement were applied which took into account a variety of changing conditions during the course of the run. The two most important corrections required by the Cherenkov program were: 1) corrections for changes in the mirror alignment angles, and 2) corrections for the changing value of the refractivity of the radiator gas. These quantities fluctuated over the course of the run, sometimes changing significantly over the interval of a few hours. The way in which these quantities were monitored is described as follows:

Mirror alignment corrections. For every track whose photons are intercepted by a given mirror, one can calculate the x and y coordinates of the ring center in the detector plane. This can be done provided one knows the orientation angles of the mirror. If, as was observed to occur, the mirror angles drift from their original values with time, then the ring center will be displaced

by an amount Δx and Δy from its original position. While it is true that each track will in general have a different ring center, all of these ring centers will be displaced by the same amount when a given mirror's orientation angles change. An approximate relation is that changing a mirror's alignment by 1 milliradian results in displacing all the photons reflected by that mirror by 16 mm.

We calculated the ring center displacements Δx and Δy for each mirror every run and wrote these values into a survey file which was later read by the analysis program. The calculation was performed by making a scatter plot of ring radius vs azimuthal angle ϕ for each photon hitting a given mirror. Now if the mirror alignment is known precisely, the points on the scatter plot will lie on the straight line $r=r_0=$constant, where r_0 is the radius of the ring. Since the mirror alignment is not known precisely, we measure r and ϕ with respect to some point which we believe to be the ring center but is actually displaced from the true ring center by the unknown amounts Δx and Δy. The points on the r vs ϕ scatter plot will then lie on the curve

$$r = \Delta x\cos\phi + \Delta y\sin\phi + \sqrt{r_0^2 - \Delta x^2\sin^2\phi - \Delta y^2\cos^2\phi + \Delta x\Delta y\sin 2\phi} \qquad (4.7)$$

We then fit the scatter plot to this equation and extract Δx and Δy for each mirror. Figure 15 illustrates this procedure.

Figure 16 shows the drift in Δy for a typical mirror over the course of a few days. The effect of thermal stresses in the mirror frames and supports were sufficient to account for the observed motion. The motion of each mirror was to a large extent independent of the motion of other mirrors. Each mirror's orientation drifted in a random walk fashion about some nominal orientation. Ring centers were observed to drift by up to 1.5 mm per day, although they were typically more stable, and no ring center drifted by more than 10 mm from its original position over the course of the run.

Index of refraction. After mirror alignments were corrected, each raw data tape was reanalyzed and the first 1000 muon tracks were selected for studying the index of refraction of the radiator gas. Starting from the relation

$$r = f\sqrt{(n^2-1) - (m/p)^2} \qquad (4.8)$$

we can calculate the refractivity $\eta=n^2-1$ if we measure the ring radius, particle mass and momentum. We made a histogram of the distribution of n^2-1 for Cherenkov photons from muon tracks via this procedure, as shown in Figure 17. This histogram was fitted

to a gaussian, and the peak was then used as the value of n^2-1 to be used for that run. As can be seen from Figure 18, the refractivity typically oscillated with a period of one day, corresponding to the circadian temperature cycle of the experimental environment.

Particle Yields and Systematic Corrections

The data were grouped into bins in total momentum p and transverse momentum p_T, where the bin widths were chosen to be 10 GeV/c in p and 0.5 GeV/c in p_T. Both bin sizes were larger than the resolution in p and p_T, respectively, and were chosen so that reasonable statistics could be gathered in each bin. Binning in p was done because many of the systematic corrections applied to the data were functions of total momentum.

The raw yields of each particle type were then corrected for a number of effects, including particle misidentification, zero photons, sparking, below threshold protons, decays in flight of kaons, target flask effects, and calorimeter efficiency. Each of these corrections is described in detail below. We first begin, however, with a discussion of the Cherenkov Monte Carlo program, which proved invaluable in identifying and calculating corrections for many of these systematic effects.

Monte Carlo description. The Cherenkov Monte Carlo program, CARLOV, was identical in all respects to the main analysis program, except that instead of analyzing real events it analyzed simulated events generated by a Monte Carlo subroutine which was substituted for the usual raw data unpacking routine. For each event, we start with a track of given momentum and arbitrarily choose the particle type (π, K, or p). We generate a random number of photons chosen according to a Poisson distribution. The point of emission of the photon along the particle path and its azimuthal angle ϕ are chosen for each photon according to a flat random number distribution. The mean Cherenkov angle θ_c is determined by particle mass and momentum, but the actual value of θ_c chosen for each photon is smeared by a gaussian to account for chromatic dispersion.

Each photon is then traced to a mirror and reflected onto a detector plane, and we record its position. After all Cherenkov photons have been generated in this way, we generate a random number of background photons according to a Poisson distribution with mean equal to 1.0. We simply choose random points on the detector plane for the location of these photons and record their positions.

The next step is to convert the photon hits into digitized ADC pulse heights in each of the cathode and anode planes. This is done in such a way as to model the pulse shapes and the

distribution of pulse height of real photon hits as closely as possible. This information is then stored in the Cherenkov ADC common blocks and passed to the main Cherenkov analysis program for processing. The program then analyzes the above data in the same way it would analyze real data. The number of reconstructed photons is compared with the number of generated photons, thereby providing us with an estimate of the software reconstruction efficiency. We also compare the program's conclusion of the particle type with the particle type generated by the Monte Carlo, and this gives us an estimate of the particle identification efficiency as well as the probability for misidentification (confusing one particle type with another).

Misidentification. For each particle type there is a probability that the analysis program will misidentify it as being some other type. The cause of this misidentification, surprisingly, has very little to do with photon resolution, since nearly all particles in our acceptance had momenta below 150 GeV/c implying π/K separation was at least 8 mm (about 6 sigma). Instead, the major source of misidentification is the photon background. One expects a non-negligible fraction of events to have a background photon located in a region where one would expect to see Cherenkov photons, and one can easily be misled by the presence of such photons. This is particularly true for those events in which we base the particle identification on the

location of a single photon. We shall see that protons are particularly sensitive to this type of misidentification.

Figure 19 shows the photon number distribution for particles identified by the program as being π, K, or p. We observe that the mean number of Cherenkov photons is particle type dependent, and is equal to 2.67 for identified pions, 2.26 for kaons, and 1.43 for protons. The fraction of events which are identified on the basis of a single photon is 21.9% for pions, 31.7% for kaons, and 67.0% for protons. A further piece of information regarding misidentification can be learned by studying the number of background photons as a function of particle type. For π^+, π^-, K^+, and p, we find in a typical run that there are an average of 1.10 photons per event which do not lie on or near the expected Cherenkov ring radius for that particle type. For K^-, however, we find 1.48 extra photons, and for $\bar{p}$ we find 3.67 extra photons. This implies that rare particle types, such as K^- and $\bar{p}$, are contaminated by events having many stray photons in which one of these photons happens to lie near the expected ring radius.

We ran the Monte Carlo and studied how often each generated particle type was misidentified by the program. We then estimated correction factors for each particle type, where we defined the correction factor has the probability for a particle which as been identified as belonging to type i to really be type i. These correction factors, which we list in Table 10, depend

to some extent on the relative particle abundances, and we quote in the Table an error for each factor which assumes a 10% systematic error in relative particle abundance. It is worth noting that while π's are correctly identified 99% of the time, one out of three antiprotons is misidentified.

Photon reconstruction efficiency. We observed from the Monte Carlo study that photon reconstruction efficiency is a function of the number of photon hits on the chamber, and can be described by

$$\varepsilon_m = e^{b(1-m)} \qquad (4.9)$$

where m is the number of photon hits, ε_m is the single photon reconstruction efficiency (i.e., the probability of reconstructing an individual photon), and b is a parameter determined by fit to be equal to 0.022±.001. This is seen in Figure 20a, which shows a plot of ε_m versus the number of photon hits m. The value of the parameter b is linearly dependent on the value of the two-photon minimum separation, as seen in Figure 20b, and the value of b given above is consistent with a two-photon minimum separation of 10±2 mm. Figure 20b was obtained via the Monte Carlo by varying the mean cathode pulse width, which directly affects the two-photon separation.

The two-photon minimum separation is defined as the minimum distance for which two photons can be separately resolved. We histogrammed in Figure 21 the distance between the two closest photons in each event for a large number of real events. We see that there are few events with photons closer than 10 mm.

If we generate m photon hits, each of which has a reconstruction probability ε_m, then the probability of reconstructing n of these photons is given by

$$P_{rec}(m,n) = \varepsilon_m^n (1-\varepsilon_m)^{m-n} \left(\frac{m!}{n!(m-n)!}\right) \qquad (4.10)$$

neglecting efficiency correlations. If we now generate photons according to a Poisson distribution with mean equal to μ

$$P_{pois}(m) = \frac{\mu^m}{m!} e^{-\mu} \qquad (4.11)$$

then the probability of reconstructing n photons is given by a folding of the Poisson distribution with the reconstruction efficiency:

$$P(n) = \sum_{m \geq n} P_{pois}(m) \cdot P_{rec}(m,n) \tag{4.12}$$

which can be explicitly written as

$$P(n) = \frac{e^{-\mu}}{n!} \sum_{m \geq n} \frac{\mu^m \epsilon_m^n (1-\epsilon_m)^{m-n}}{(m-n)!} \tag{4.13}$$

The mean of this distribution is given by

$$\begin{aligned} \langle x \rangle &= \sum_{n=0}^{\infty} P(n) \cdot n \\ &= \sum_{n=1}^{\infty} \frac{e^{-\mu}}{(n-1)!} \sum_{m \geq n} \frac{\mu^m \epsilon_m^n (1-\epsilon_m)^{m-n}}{(m-n)!} \end{aligned} \tag{4.14}$$

This mean value $\langle x \rangle$ is always less than the mean μ of the original Poisson distribution. A point worth mentioning here is that if the photon reconstruction efficiency were not dependent on the number of photon hits (i.e., $\epsilon_m = \epsilon$ for all values of m), then the above distribution P(n) would simply reduce to a Poisson distribution with mean $\nu = \mu\epsilon$. Such a reduction cannot be made if, as we have observed, ϵ_m depends on m.

Zero-photon correction. We are interested in determining with what frequency we do not reconstruct any photons. That is, if we assume that we can identify a particle on the basis of reconstructing at least one photon, and the number of reconstructed photons is determined by some distribution P(n), then we must correct the number of particles we identify by a factor which accounts for the probability of reconstructing zero photons:

$$N_{corr} = N_{obs}/\varepsilon_{id} = \frac{N_{obs}}{(1-P(0))} \qquad (4.15)$$

We call ε_{id} the particle identification efficiency. For a Poisson distribution, we have

$$\varepsilon_{id} = 1-e^{-\mu} \qquad (4.16)$$

where μ is the mean of the distribution. As we have seen in the previous section, the number of reconstructed photons differs from a Poisson distribution, and we must use the expression

$$\epsilon_{id} = 1 - e^{-\mu} \sum_{n=0}^{\infty} \frac{\mu^n}{n!} (1-\epsilon_n)^n \qquad (4.17)$$

for the identification efficiency. This quantity can be calculated once we know the photon reconstruction efficiencies ϵ_n, which were calculated via the Monte Carlo, and the mean number of photons μ, whose calculation is described in the next section.

Mean number of photons. The mean number of photons is proportional to the square of the Cherenkov ring radius, and for a particle type i with momentum p can be expressed by

$$\mu_i(p) = \mu_0 \left(\frac{r_i(p)}{r_0} \right)^2 = \mu_0 \left\{ 1 - \frac{m_i^2}{\eta p_i^2} \right\} \qquad (4.18)$$

where $\eta = n^2 - 1$ is the refractivity and μ_0 is the mean number of photons for an infinite-momentum particle. To calculate μ_0, we took a sample of pions from each run and calculated the mean number of "scaled" photons, where we scaled the number of photons observed for each pion by a factor which accounts for finite-momentum effects:

$$n_{scaled} = n_{obs} \left(\frac{1}{1 - m_\pi^2/\eta p^2} \right) \qquad (4.19)$$

We call the observed mean number of scaled photons $\langle x_{obs} \rangle$. This is related to $\langle x \rangle$, the mean number of reconstructed photons governed by the distribution P(n), by

$$\langle x_{obs} \rangle = \frac{\langle x \rangle}{\epsilon_{id}} = \frac{\langle x \rangle}{1-P(0)} \qquad (4.20)$$

since we must correct the observed mean by the particle identification efficiency in order to properly account for zero-photon events. For the distribution P(n) we observe in our data, we obtain the following expression for $\langle x_{obs} \rangle$:

$$\langle x_{obs} \rangle = \frac{\sum_{n=1}^{\infty} \frac{e^{-\mu}}{(n-1)!} \sum_{m \geq n} \frac{\mu^m \epsilon_m^n (1-\epsilon)^{m-n}}{(m-n)!}}{1 - e^{-\mu} \sum_{n=0}^{\infty} \frac{\mu^n}{n!} (1-\epsilon_n)^n} \qquad (4.21)$$

In principle we can invert this equation to obtain μ_0. This cannot be done analytically, and we instead constructed a table of $\langle x_{obs} \rangle$ vs μ_0, measured $\langle x_{obs} \rangle$ as we described above, and looked up the corresponding value of μ_0 in the table.

The value of μ_0 was calculated for each detector and for each run, and is shown in Figure 22. The mean number of photons was typically 2.5 to 2.75 during the periods of optimal chamber performance.

Corrections for sparking. As mentioned in chapter 3, we attempted to monitor the occurrence of sparking in the photon chambers by setting a bit to be read out in the event record every time a spark was detected. The effect of a spark is to leave the chamber dead for a time interval of the order 10-50 milliseconds, and we find that it was not possible to distinguish an event containing no photons due to sparking from a perfectly normal event which just happens to contain no photons. We present in Table 11 the summary of a separate analysis of normal events and events which have the spark bit set. We see that the fraction of events which have been positively identified is lower for the spark events than for the normal events, as expected. Nevertheless, we do see that more than 50% of the spark events can be identified.

We needed to check if sparking occured in those events which did not have the spark bit set. This could be determined by seeing if there were more zero-photon events than could be accounted for by applying the zero-photon correction as described previously. In, fact, we did observe such a zero-photon excess in certain runs, which led us to believe that the spark bit

failed intermittently. This situation was corrected by calculating a live factor, or "non-sparking" factor, for each chamber and for each run. This live factor was calculated by dividing the number of identified hadrons, corrected for misidentification and zero-photon effects, by the total number of hadrons:

$$\ell = \frac{\sum N_i f_i / \varepsilon_i}{N_{tot}} \qquad (4.22)$$

In the above expression, N_i is the number of identified hadrons of type i, f_i is the misidentification correction, and ε_i is the particle identification efficiency. This calculation is summed over all particle types, but only for particles with momenta above proton threshold.

The live factors for each detector are plotted vs run number in Figure 23. The corrected yield of each particle type is then given by

$$Y_i(p,p_T) = \frac{N_i(p,p_T) f_i(p)}{\varepsilon_i(p) \ell} \qquad (4.23)$$

These yields were subsequently corrected for protons below threshold, decays in flight, and target flask effects.

Protons below threshold. Protons below threshold (110 GeV/c) have an identification efficiency of zero. To account for their number in a statistical way, we first calculated the number of identified π's and K's below 110 GeV/c and applied all the correction procedures discussed previously, and then simply identified all excess hadrons as protons.

We checked the validity of this procedure by calculating the number of protons above threshold via two methods and compared the results: first, we counted the number of positively identified protons and applied the standard correction procedures; and second, we subtracted the number of π's and K's from the total number of hadron events. The two methods agreed to within statistical errors.

Decays in flight. We had to correct the number of observed kaons for decays in flight. The major decay modes of charged kaons are $K^{\pm}\rightarrow\mu^{\pm}\nu$ (branching ratio = 64%) and $K^{\pm}\rightarrow\pi^{\pm}\pi^{0}$ (B.R. = 21%). We neglected all other decay modes. For the case of $K\rightarrow\mu\nu$, a kaon decaying in this fashion before hitting the calorimeter will leave only a minimum energy deposit in the calorimeter and will not set any of the hadron triggers. For the case $K\rightarrow\pi\pi^{0}$, the combined energy deposit of the two pions will generally look like a single cluster in the calorimeter, provided the K decays after the SM3 magnet. In most cases, however, the decay angle between the K and the charged pion will be sufficiently large so that we

will not be able to reconstruct a track. We estimate that only 0.1% of the decays $K \to \pi\pi^0$ will be reconstructed for 100 GeV/c kaons. This fraction rises to about 0.2% for 200 GeV/c kaons. So by concluding that all K decays are either not triggered or are rejected in the analysis, we can correct for them simply by multiplying the kaon yield in each momentum bin by a factor

$$f_{decay} = e^{mx/pc\tau} \qquad (4.24)$$

where p is the average momentum of the bin, $c\tau = 370.9$ cm is the decay constant for kaons, and x is the distance from the target to the front face of the calorimeter (2030 inches). The correction factor for a 100 GeV/c kaon is about 5%.

Pions decay via $\pi^{\pm} \to \mu^{\pm}\nu$ (100% branching ratio) and have a longer lifetime than kaons ($c\tau$=780.4 cm). We find that the decay probability for π's is less than 1% for all interesting momenta, and so we neglect their decay in the analysis.

Target flask corrections. A certain fraction of the events we analyzed came from beam-target flask interactions, as well as from interactions of the beam with either of the two windows at either end of the vacuum box containing the target. To correct for this background, we interspersed normal target running with a number of empty target runs. The particle yield due solely to

beam-liquid interactions is given by

$$Y = Y_{full} - \left(\frac{N_{full}}{N_{empty}} \right) Y_{empty} \qquad (4.25)$$

where N_{full} and N_{empty} are the number of protons on target for the full- and empty- target running, respectively. The above expression must also be corrected for the fact that an "empty" target is not really empty but contains H_2 (or D_2) gas. While this correction is of the order of 3%, it only affects the absolute normalization of the cross-sections and cancels out in the calculation of particle ratios.

Calorimeter efficiency correction. The probability for a hadron to satisfy the EHI (total energy deposit) trigger after depositing an amount of energy E in the calorimeter is given by the error function

$$\varepsilon(E) = \mathrm{erf}\left[\frac{E-E_t}{\sigma}\right] = \frac{1}{\sqrt{2\pi}\sigma} \int_{-\infty}^{E} e^{-\frac{1}{2}\left(\frac{x-E_t}{\sigma}\right)^2} dx \qquad (4.26)$$

where E_t is the energy threshold for the calorimeter trigger. The energy E as measured by the calorimeter must first be

corrected by an attenuation factor which depends on the x-position of the track. The threshold E_t varies from counter to counter and mostly depends on differences in phototube gain. The threshold for each counter was measured by studying pre-scaled hadron events. These prescaled events were triggered in the same way as EHI triggers (total energy deposit), but with a lower attenuation factor, and therefore a lower threshold (typically 50-60 GeV). We plotted the fraction of the pre-scaled events satisfying the EHI trigger as a function of calorimeter energy deposit, and fitted the resulting distribution to the function shown above.

A plot of the distribution for a typical counter is shown in Figure 24. The EHI trigger thresholds were measured for every counter and are listed in Table 12. As shown in Figure 25, the average efficiency for positive and negative particles is somewhat different, making comparison of positive and negative yields subject to systematic error. To minimize this error, we made two requirements: 1) the trigger efficiency for each hadron track we accepted was required to exceed 10%. 2) For every hadron that satisfies the above requirement, we make the additional demand that the "analogous" opposite sign track also have a trigger efficiency exceeding 10%. An analogous track is defined by the track having opposite sign to the original track, but having the same p_T and θ^*. The azimuthal angle for this track

is chosen to be $-\phi$, where ϕ is the azimuthal angle of the original track. The effect of this requirement is to insure as well as possible that the acceptances for positives and negatives are the same. This minimizes the systematic error due to calorimeter trigger efficiency in the π^+/π^- measurement.

We used a lower attenuator setting for the EHI triggers in the early part of our data run, resulting in lower thresholds than listed in Table 12. Table 5 lists the attenuator settings for the different runs; the thresholds with a given attenuator setting equal to a is given by

$$E_a = E_7 \times 10^{(a-7)/20} \tag{4.27}$$

where E_7 is the EHI threshold given in Table 12, and a is the attenuator setting.

The thresholds of the EYU and EYD triggers were measured in a similar way to the EHI triggers. When calculating the trigger efficiency for a given track, if more than one trigger (EYU, EYD, or EHI) was set, we used the lowest threshold among those triggers which had been set.

Species dependence of the calorimeter trigger. We checked whether the efficiency of the calorimeter trigger depended on particle type. This concern arose because of the fact that

different particle types have different nuclear interaction cross sections. In particular, the total cross section for proton-proton collisions at 100 GeV/c beam momentum is $\sigma_{tot}(pp) = 40$ mb, while the corresponding cross sections for π's and K's are $\sigma_{tot}(\pi p) = 25$ mb and $\sigma_{tot}(Kp) = 20$ mb. This implies that hadronic showers initiated by π's and K's begin later in the calorimeter than proton initiated showers, which might result in the calorimeter responding differently to different particle types. We checked this hypothesis by measuring the calorimeter trigger thresholds for each individual particle type using the method described in the last section. We found no difference in threshold to within ±1 GeV.

Cross section measurement. The inclusive cross section for pp→h+X was calculated using the formula

$$E\frac{d^3\sigma}{dp^3}(p_T) = \frac{N(p_T)}{\mathcal{L}\cdot a(p_T)\cdot\varepsilon(p_T)\cdot\overline{p_T}\cdot\Delta p_T} \qquad (4.28)$$

where the various quantities in this expression are:

$N(p_T)$= the observed particle yield in the bin p_T to $p_T+\Delta p_T$,

L=the integrated luminosity, which is equal to $N_p N_0 \rho\ell$, the number of protons on target times N_0 (Avogadro's number) times the target density times the target length.

$\varepsilon(p_T)$= the overall efficiency for events in this p_T bin. The overall efficiency is the product of all the various efficiencies discussed in the previous section, and include particle identification efficiency, calorimeter trigger efficiency, and tracking efficiency.

$a(p_T)$= the geometrical acceptance, which is defined as 4π times the fraction of particles produced at a given p_T whose trajectories pass through the experimental aperture. The acceptance was calculated via a simple Monte Carlo program.

CHAPTER 5

Results and Discussion

We present our measurements of the invariant cross sections and ratios of cross sections as functions of transverse momentum p_T and center of momentum production angle θ^*. Following a discussion of systematic error, we compare our data to general expectations within the framework of the Quark Parton Model. We conclude by making a detailed comparison with the Lund Monte Carlo.

Invariant cross sections. The naive parton model [2] predicts that the cross section for the inclusive reaction $pp \rightarrow \pi^+ + X$ should fall as a power of p_T,

$$E \frac{d^3\sigma}{dp^3} = \frac{1}{p_T^N} f(x_T, \cos\theta^*) \qquad (5.1)$$

where f is a function of the dimensionless variables $x_T = 2p_T/\sqrt{s}$ and $\cos\theta^*$. N is expected to be equal to 4 for dimensional reasons [40], since the cross section $Ed^3\sigma/dp^3$ has units of $[cm^2 GeV^{-2}]$, which in natural units ($\hbar = c = 1$) is equal to $[energy^{-4}]$. However, early measurements [40] found N=8, leading

to the realization that the production mechanisms were more complicated than the naive parton model suggested. From a more sophisticated QCD analysis of the problem, one finds several different subprocesses contributing to high-p_T production [5-6,8]. For example, Figure 26 shows a calculation showing the relative contribution of gluon-gluon, gluon-quark, and quark-quark subprocesses on pion production. In fact, one notes from the figure that above 6 GeV/c in p_T, simple quark-quark scattering becomes the dominant subprocess.

The cross sections for the reactions $pp \rightarrow \pi^{\pm}+X$ and $pd \rightarrow \pi^{\pm}+X$ are presented in Table 13 and Figure 27. We show the results from the Chicago-Princeton (CP) experiment [41-44] in the figures for comparison. We note that our results are within a factor of two of CP in the region in p_T where our acceptances overlap. We note that although some systematic errors affecting the shape of the data still remain, we conclude that none of these errors affect the particle ratios. We now continue with the main thrust of our discussion, namely, the particle ratios.

Like-sign particle ratios. The ratios K^+/π^+, p/π^+, K^-/π^-, and $\bar{p}/\pi^-$ are presented in Table 14 and Figures 28-37. Also displayed in the figures are the results of the Chicago-Princeton (CP) measurements of these same quantities, but at a lower p_T [41-44]. (There is a small region of overlap around 6 GeV/c p_T.) We have extended their measurements by 1 to 2 GeV/c in p_T, and are in agreement with the general features of their data.

π^+/π^- ratios. Measurement of the relative production of π^+ and π^- involved a detailed knowledge of the calorimeter efficiency. Such a study was undertaken and is described in the previous chapter, where we took note of the somewhat different efficiencies for positive and negative particles. The results for π^+/π^- are presented in Table 15 and Figure 32 for $pp \rightarrow \pi^{\pm}x$, and Table 15 and Figure 37 for $pd \rightarrow \pi^{\pm}x$. In addition, measurements from the CP experiment have been included in each figure.

Dependence of particle ratios on θ^*. We divided the data into bins according to center of mass angle θ^* for the particle ratios K^+/π^+ and π^+/π^-. The results are shown in Table 16 and Figures 38-41. The other particle ratios did not contain enough events for us to make a meaningful measurement of the θ^* dependence.

Sources of systematic error. One advantage to the measurement of particle ratios is that it is relatively free of systematic error, as compared to making an absolute cross section measurement. Only those errors which depend upon particle type contribute to the systematic errors in the particle ratios.

Particle ratios are given by

$$R_{ij} = Y_i/Y_j \qquad (5.2)$$

where Y_i and Y_j are the corrected particle yields for particle types i and j respectively. The corrected yields were discussed in the previous chapter and can be written

$$Y_i = \frac{N_i f_i}{\varepsilon_i \ell} \cdot Z_i \qquad (5.3)$$

where N_i, the raw yields, are corrected by the misidentification factor f_i, the detection efficiency ε_i, and the sparking correction ℓ. The factor Z_i is a "generic" correction factor which includes corrections which apply to only certain particle types: protons must be corrected to account for the number below threshold, kaons must be corrected for decays in flight, and the π^+/π^- ratio must be corrected for the difference in calorimeter trigger efficiency for positive and negative tracks.

By writing the expression for the particle ratios with all the correction factors shown explicitly,

$$R_{ij} = \left(\frac{N_i f_i}{\varepsilon_i \ell}\right)\left(\frac{\varepsilon_j \ell}{N_j f_j}\right)\left(\frac{Z_i}{Z_j}\right) = \left(\frac{N_i}{N_j}\right)\left(\frac{\varepsilon_j}{\varepsilon_i}\right)\left(\frac{f_i}{f_j}\right)\left(\frac{Z_i}{Z_j}\right) \qquad (5.4)$$

we see that the particle ratio R_{ij} is just the ratio of the raw counts N_i/N_j, multiplied by a series of correction factors. The

total error in R_{ij} can be expressed as

$$\frac{\sigma_R^2}{R_{ij}^2} = \left[\left(\frac{\sigma_{Ni}}{N_i}\right)^2 + \left(\frac{\sigma_{Nj}}{N_j}\right)^2\right] + Sys\{\varepsilon_i,\varepsilon_j,f_i,f_j,Z_i,Z_j\} \quad (5.5)$$

The terms in square brackets represent the statistical error where we use $\sigma_N=\sqrt{N}$. The function $Sys\{\cdots\}$ represents the systematic error due to uncertainties in calculating the correction factors. We assume that the errors in the individual correction factors add in quadrature, allowing us to write

$$Sys\{\varepsilon_i,\varepsilon_j,f_i,f_j,Z_i,Z_j\} = \left(\frac{\sigma_{\varepsilon i}}{\varepsilon_i}\right)^2 + \cdots + \left(\frac{\sigma_{Zj}}{Z_j}\right)^2 \quad (5.6)$$

The problem remains to determine the individual errors. In the following discussion, we estimate the limit of error for each correction factor, so that our estimate for the overall systematic error is rather conservative.

The error due to uncertainty in the particle detection efficiency ε_i depends on the error in measuring the mean number of photons and in calculating the photon reconstruction efficiency. The error in the mean number of photons for a

particle with a given momentum depends in turn on the error in the momentum measurement and the error in the refractivity measurement. The photon reconstruction efficiency was calculated via Monte Carlo, and its error depends upon how well we modelled real pulses in the Monte Carlo. We find that the error in ε_i only becomes significantly large for particles with momenta slightly above Cherenkov threshold. Given the momentum distribution of the particles in our data, we estimate $\sigma_\varepsilon/\varepsilon$ to be equal to 1% for π's, 2% for K's, and 6% for protons.

The sparking correction is important only in calculating the p/π ratio. This is so because one needs to know this correction in order to be able to calculate the number of protons below threshold. We can write the p/π ratio as

$$R_{p/\pi} = \frac{\left[N\not{s} - (N_\pi f_\pi/\varepsilon_\pi) - (N_K f_K/\varepsilon_K)\right]_{<110\ \mathrm{GeV}} + (N_p f_p/\varepsilon_p)}{N_\pi f_\pi/\varepsilon_\pi} \qquad (5.7)$$

The terms in square brackets are evaluated only for particles below proton threshold (110 GeV/c). N is the total number of such particles, and $\not{s}$ is the sparking correction. The dependence of the error in the p/π ratio on $\not{s}$ is given by

$$\frac{\partial R}{\partial \lambda} = \frac{N}{N_\pi f_\pi / \varepsilon_\pi} \qquad (5.8)$$

This number is ≈1.5. The limit of error on λ, which depends on the error in ε_i for every particle type i, is estimated to be 5%, leading to an estimate of 7.5% for the limit of error on the contribution of λ to the systematic error in the p/π ratio.

Table 17 lists the overall systematic error estimates on each of the particle ratios. In addition to the contributions to the error discussed above, we include contributions of 0.5% to the K/π ratios to account for the error in calculating the number of K decays, and a contribution of 10% to the π^+/π^- ratio to account for the error in calculating the calorimeter trigger efficiency. We note that the $\bar{p}/\pi^-$ ratio has the highest systematic error estimate, 13.4%, and its main contribution, 9%, comes from $\bar{p}$ misidentification.

Discussion. The major features of the data are easy to understand within the framework of the Quark Parton Model. At high p_T, we expect mostly quark-quark scattering as the dominant subprocess, with a small amount of quark-gluon scattering whose rate relative to qq diminishes with p_T [6]. From knowledge of the quark content of mesons, we can reach the following conclusions:

Both $\pi^+(u\bar{d})$ and $K^+(u\bar{s})$ result primarily from the fragmentation of a scattered u quark, while $\pi^-(d\bar{u})$ results primarily from d quark fragmentation. $K^-(s\bar{u})$, on the other hand, contains no valence quarks in common with nucleons, and it is reasonable to suggest that K^- arise from the fragmentation of a scattered gluon.

If we assert that quark fragmentation is more or less independent of p_T, the K^+/π^+ ratio should be constant at high p_T, and should reflect the relative difficulty of producing $s\bar{s}$ pairs during fragmentation compared to producing the lighter quarks. In fact, we observe a fairly constant ratio of about .4 above about 4 GeV/c p_T for both pp and pd data, although we see a slight decrease with higher p_T.

The K^-/π^- ratio should fall with p_T, reflecting the fall off of the gluon structure function at high x. Our data (as well as CP) does show a strong drop with p_T in the hydrogen data, falling to almost zero at 8 GeV/c p_T. We see a drop in the deuterium data as well, although the slope of this drop is somewhat less.

The π^+/π^- ratio should be very different in pp and pn scattering. From measurements of deep-inelastic scattering, it is now known that the ratio of the u quark to d quark structure functions in the proton rise at high x, as shown in Figure 42. One possible explanation for this is the idea, proposed by the Stockholm group [45-48], that the d-quark and one of the u-quarks

in the proton form a loosely bound diquark system, whose effective structure function peaks at very low x. Only the remaining u-quark has an appreciable probability of being found at high x, leading to the prediction that the highest p_T collisions are the result of u-u quark scatterings, while u-d and d-d scatterings are suppressed. This in turn implies a very high π^+/π^- ratio at high p_T, rising well above the value of 2 that one expects from simple quark counting.

The situation is entirely different in pn collisions. The structure functions of the neutron are determined by isospin symmetry, and we have the relations $d_n(x)=u_p(x)$ and $u_n(x)=d_p(x)$. Therefore, there are equal numbers of u and d quarks in the pn scattering system at all values of x and at $\theta^*=90°$, which leads to the expectation that π^+/π^- is equal to 1 at all values of p_T. By assuming that the $V\pi^+/\pi^-$ ratio in proton-deuteron scattering can be approximated by averaging the predictions for proton-proton and proton-neutron scatterings, we conclude that the π^+/π^- ratio should rise with p_T at a rate one-half that of the rise in proton-proton scattering. Our measurements confirm these simple predictions within systematic errors, except for the point at 5.75 GeV/c, which shows a measurement of less than 1, which is surprising in terms of the above discussion.

Baryon production. The production of baryons at high p_T is less well understood than meson production [49]. In the Lund model, baryons are produced from the creation of diquark-antidiquark pairs during the fragmentation process. The model assigns a fixed probability for the creation of diquark pairs relative to quark pairs, leading to a p/π^+ ratio which is independent of p_T. We see from our data that at higher p_T the ratio p/π^+ approaches a constant value of about .1, having fallen off from higher values at low p_T. It has been suggested [45] that the scattering of diquarks are responsible for the large number of baryons seen at low p_T, but this process is not expected to contribute significantly at higher values of p_T.

Production of $\bar{p}$'s are expected to be very small, considering the fact that antiprotons do not share any valence quarks in common with nucleons. The situation here is similar to K^- production, and one might suggest that gluon fragmentation is responsible for high p_T $\bar{p}$'s. We observe a fall off of $\bar{p}/\pi^-$ with p_T in both the hydrogen and deuterium data, but in both cases the ratio seems to level off to a minimal value of 0.025. This leveling off is seen by CP in hydrogen but not in deuterium, where they instead observe the ratio falling to zero at 6 GeV/c.

We have made a detailed comparison of our data with the Lund Monte Carlo program for high-p_T physics, and we summarize our findings in Figures 28-46. In the following discussion, we first discuss some of the general features of the Lund program, and then we describe how we modified various parameters and switches in the program in order to achieve better agreement with our data. We finally draw some physics conclusions based on the above exercise.

Program description. We used program PYTHIA version 4.1 [57] to generate high-p_T Monte Carlo events, which were then passed to the Lund fragmentation routines in program JETSET version 6.1 [58]. These programs are based on previously published versions [28,29]. These events were generated in the following way: first, one parton is chosen from each of the colliding hadrons (we are allowed to choose either pp or pn collisions). The momentum and flavor of each parton is chosen according to the distribution functions $G(x,Q^2)$. These partons are then allowed to collide and their scattering angles are chosen according to the 1st order QCD scattering cross sections $d\hat{\sigma}/d\hat{t}$. The program then fragments each parton jet along with the beam and target fragments according to the Lund string model. The program keeps track of all particles which have been created in the fragmentation process; in addition, particles are created following the parton fragmentation via the deacy of unstable

particles. We are then left with a large number (typically 20-50) final state particles, including photons, electrons, neutrons, protons, pions, and kaons. We then histogram the values of p_T and θ^* of all final state charged stable hadrons (i.e., π, K, p) which have p_T greater than 2 GeV/c. We repeat this process for the next Monte Carlo event.

In each program run we generated 50,000 hard scattering events, which led to the production of about 5000 π's, and smaller numbers of K's and protons, with p_T greater than 2 GeV/c. In most events, we find that the scattered partons fragment to such a degree that their momenta are divided among a large number of particles, none of which have a very high p_T. Because of this, we find that the Lund Monte Carlo is a very inefficient way to study the production of high-p_T single particles; on the other hand, its availability and its simplicity of program structure made it easy for a non-expert to use. To model proton-deuteron interactions, we made two program runs, one with proton-proton scattering and the other with proton-neutron scattering. We then approximated proton-deuteron scattering by averaging the results of the above runs and ignoring any nuclear effects.

Comparison with standard parameters. The Lund program has a number of parameters set by default to certain 'reasonable' values. Two of these which govern the details of the fragmentation process are P(s)/P(u) and P(qq)/P(q). The

parameter P(s)/P(u) gives the relative probability of creating an $s\bar{s}$ quark-antiquark pair out of the vacuum as compared to creating a $u\bar{u}$ pair. This parameter is set by default to 0.3. The other parameter, P(qq)/P(q), gives the relative probability for creating a qq-$\bar{q}\bar{q}$ diquark-antidiquark pair to that of creating just an ordinary $q\bar{q}$ pair. This is set to 0.1 by default.

Besides these parameters, the program has a number of switches allowing us to choose among several options. One switch allows us to choose which set of structure function parameterizations we wish to use. By default we use the EHLQ structure functions [14]. Another switch allows us to change the definition of Q^2. Also, one can turn on or off the simulation of initial and final state gluon radiation, and one can select among several options for QCD matrix elements.

The standard program predictions are shown in the solid curves in Figures 28-37 for each of the particle ratios. We make the following observations: the Lund prediction for π^+/π^- is in excellent agreement with the hydrogen data but disagrees with the deuterium data. For those ratios involving K's and protons, however, the Monte Carlo predictions are clearly incorrect. We see that the prediction for K^+/π^+ is low, while the prediction for K^-/π^- has too shallow a slope, so that it is too low below 5 GeV/c p_T and too high above this p_T. The predictions for p/π^+ and $\bar{p}/\pi^-$ are consistently too high in both the H_2 and D_2 data.

We have attempted to adjust enough parameters to get predictions in reasonable agreement with the data for all the particle ratios. The first major step was to correct the fragmentation parameters P(s)/P(u) and P(qq)/P(q). We lowered P(qq)/P(q) to a value of 0.05. The result can be seen in the dashed curves in Figures 28-37, and is in very good agreement with the data for $\bar{p}/\pi^-$, but we see that for the p/π^+ ratio, we model the high-p_T (>5GeV/c) very well, while our predictions for low p_T are much too low. This lends support to the idea that scattering of constituent diquarks is responsible for the anomalously high production of low-p_T protons. We could not make a quantitative study of this hypothesis because constituent diquarks were not an available option in the Lund Monte Carlo program. We also raised the parameter P(s)/P(u) to a value of 0.5, which, as we see in the dashed curves in Figures 28-37, gives us reasonably good agreement for the K^+/π^+ ratio, but pushes the K^-/π^+ prediction in the wrong direction, that is, much too high.

Gluon radiation. The most recent version of the Lund program, version 4.1, attempts to model the radiation of gluons by the initial and final state partons. By this we mean that the interacting partons can radiate a significant portion of their energy away as gluons, both before and after the primary collision. We explored the possibility that a significant number

of K^- resulted from the fragmentation of these radiated gluons by simply switching off this process in the Lund program. The results are shown in Figure 44. We see little or no change in any of the particle ratios. This leads us to suggest that gluon radiation is not a significant factor in the generation of high-p_T hadrons. On the contrary, we discovered in running that Lund Monte Carlo that we generated larger numbers of high-p_T hadrons by turning off the gluon radiation. In the remainder of our analysis, we will continue to leave out gluon radiation effects.

Structure function comparison. Figures 42 and 43 show ratios of structure functions, as parameterized by EHLQ[14] and Duke-Owens[12]. We see that in Figure 42, which shows the ratio of the u-quark to d-quark structure functions, that while both parameterizations have the same general shape, EHLQ is somewhat higher than Duke-Owens. We also see a slight difference in the ratios of the gluon to u-quark structure functions in Figure 43. We ran the Lund Monte Carlo with the Duke-Owens structure functions to see if our data, particularly π^+/π^- in the case of u-quark to d-quark structure functions, could distinguish between the two parameterizations. Our results are shown in Figure 45. We find it hard to favor one set of structure functions over the other.

Definition of Q^2. We explored the possibility that Q^2 should be defined in some other way. A reasonable alternative which seems to have some physical justification is

$$Q^2 = \hat{t}\hat{u}/\hat{s} \tag{5.9}$$

This is just the square of the transverse momentum acquired by each scattered parton. We ran the Lund program with this definition of Q^2. The result is seen in Figure 46, and we see little effect on the particle ratios.

Conclusions. We have measured particle ratios in proton-proton and proton-deuteron collisions and compared our results to the Lund Monte Carlo. We find the good agreement with the standard Lund model in the π^+/π^- ratio in hydrogen, but does not agree as well with the π^+/π^- ratio in deuterium. We find that the standard Lund model is not consistent with our measurements of the K/π and p/π ratios, but better agreement can be obtained via modification of the Lund parameters governing the details of the fragmentation process. In particular, we find we can obtain good agreement with the measurements of K^+/π^+ by setting the parameter $P(s)/P(u) = 0.5\pm.05$, and we obtain good agreement with $\bar{p}/\pi^-$ by setting the parameter $P(qq)/P(q) = 0.05\pm.005$. However, we observe that the p/π^+ ratio cannot be fit

to the Lund model over the range $2<p_T<8$ GeV/c, and suggest that the anomalously large number of protons seen at lower values of p_T are due to the scattering of diquark constituents as described in [45-48]. We also observe that the ratio K^-/π^- falls off at high p_T much faster than predicted by the Lund model.

List of References

1. J.D. Bjorken, Phys. Rev. 179 (1969) 1547.

2. R.P. Feynman, Photon Hadron Interactions, Benjamin Press, New York, 1972.

3. S. Berman, J.D. Bjorken, & J. Kogut, Phys. Rev. D4 (1971) 3388.

4. S.D. Ellis & M.B. Kislinger, Phys. Rev. D9 (1974) 2027.

5. R. Cutler & D. Sivers, Phys. Rev. D16 (1977) 679.

6. B.L. Combridge, J. Kripfganz, & J. Ranft, Phys. Lett. 70B (1977) 234.

7. J.F. Owens, E. Reya, and M. Glück, Phys. Rev. D18 (1978) 1501.

8. R.P. Feynman, R.D. Field, & G.C. Fox, Phys. Rev. D18 (1978) 3320.

9. M. Derrick & T. Gottschalk, ANL-HEP-CP-84-76.

10. G. Arnisson et. al., Phys. Lett. 123B (1983) 115.
M. Banner et. al., Phys. Lett. 118B (1982) 203.
P. Bagnaia et. al., Z. Phys. C20 (1983) 117.

11. M.W. Arenton et. al., Phys. Rev. D31 (1985) 984.

12. D.W. Duke & J.F. Owens, Phys. Rev. D30 (1984) 49.

13. M. Gluck, E. Hoffman, & E. Reya, Z. Phys. C13 (1982) 119.

14. E. Eichten, I. Hinchliffe, K. Lane, & C. Quigg, Rev. Mod. Phys. 56 (1984) 579.

15. R.D. Field & R.P. Feynman, Nucl. Phys. B136 (1978) 1.

16. R.D. Field & R.P. Feynman, Phys. Rev. D15 (1977) 2590.

17. R.P. Feynman et. al., Nucl. Phys. B128 (1977) 1.

18. R.D. Field & S. Wolfram, Nucl. Phys. B213 (1983) 65.

19. B.R. Webber, Nucl. Phys. B238 (1984) 492.

20. F.E. Paige & S.D. Protopopescu, BNL-29777 (1981).

21. R. Odorico, Nucl. Phys. B228 (1983) 381.

22. R.D. Field, G.C. Fox, & R.L. Kelly, Phys. Lett. 119B (1982) 439.

23. B. Andersson et. al., Phys. Reports 97C (1983) 31.

24. B. Andersson et. al., Z. Phys. C1 (1979) 105.

25. B. Andersson & G. Gustafson, Z. Phys. C3 (1980) 223.

26. B. Andersson, G. Gustafson, & T. Sjöstrand, Z. Phys. C6 (1980) 235.

27. G. Gustafson, Z. Phys. C15 (1982) 155.

28. H.-U. Bengtsson et. al., LU TP 84-3.
H.-U. Bengtsson, Computer Phys. Comm. 31 (1984) 323.
H.-U. Bengtsson, G. Ingelman, Computer Phys. Comm. 34 (1985) 251.

29. T. Sjöstrand, LU TP 82-3.
T. Sjöstrand, Computer Phys. Comm. 27 (1982) 243.

30. Y. Sakai, Ph.D. Thesis, Kyoto University, Japan, 1984.

31. H. Glass et. al. IEEE Transactions on Nucl. Sci. NS-32 (1985) 692.

32. H. Glass et. al., IEEE Transactions on Nucl. Sci. NS-30 (1983) 30.

33. M. Adams et. al., Nucl. Instr. & Meth. 217 (1983) 237.

34. G. Coutrakon et. al., IEEE Transactions on Nucl. Sci. NS-29 (1982) 323.

35. R. Bouclier et. al., Nucl. Instr. & Meth. 205 (1983) 403.

36. Ph. Mangeot et. al., Nucl. Instr. & Meth. 216 (1983) 79.

37. J. Crittenden, Ph.D. Thesis, Columbia University, 1985.
Y.B. Hsiung, Ph.D. Thesis, Columbia University, 1985.

38. D. Jaffe, Ph.D. Thesis, SUNY at Stony Brook, in preparation.

39. R. Gray, Ph.D. Thesis, University of Washington, in preparation.

40. P. Darriulat, Ann. Rev. Nucl. Sci. 30 (1980) 159.

41. D. Antreasyan et. al., Phys. Rev. D19 (1979) 764.

42. D. Antreasyan et. al., Phys. Rev. Lett. 38 (1977) 112.

43. J.W. Cronin et. al., Phys. Rev. Lett. 31 (1973) 1426.

44. J.W. Cronin et. al., Phys. Rev. D11 (1975) 3105.

45. S. Fredriksson, M. Jändel, & T.I. Larsson, Phys. Rev. Lett. 51 (1983) 2179.

46. S. Fredriksson et. al., Z. Phys. C14 (1982) 35.

47. S. Fredriksson et. al., Z. Phys. C19 (1983) 53.

48. S. Ekelin & S. Fredriksson, TRITA-TFY-84-11 (1984).

49. J.F. Owens, Phys. Rev. D19 (1979) 3279.

50. J. Litt and R. Meunier, Ann. Rev. Nucl. Sci. 23 (1973) 1.

51. E. Leader and E. Predazzi, An Introduction to Gauge Theories and the 'New Physics', Cambridge University Press, 1982.

52. P.R. Bevington, Data Reduction and Error Analysis for the Physical Sciences, McGraw-Hill, New York, 1969.

53. Muffoletto Optical Company, Baltimore, Maryland.

54. Fujitsu,Ltd., Marunochi, Chiyoda-ku, Tokyo, Japan.

55. V.P. Zrelov, Cherenkov Radiation in High-Energy Physics, Atomizdat, Moscow 1968.

56. R.E. Plaag, Ph.D. Thesis, University of Washington, in preparation.

57. H.-U. Bengtsson, G. Ingelman, T. Sjöstrand, "The Lund Monte Carlo for QCD high pt Scattering," 1985. Documentation and source code available from T. Sjöstrand, Theoretical Physics Dept., FNAL, P.O. Box 500, Batavia, IL 60510.

58. T. Sjöstrand, "The Lund Monte Carlo for Jet Fragmentation and e+e- annihilation," 1985. Documentation and source code available from T. Sjöstrand.

TABLE I

1st order QCD cross sections

subprocess	$d\sigma/dt$
$q_a q_b \to q_a q_b$	$\frac{\pi\alpha_s^2}{s^2}\left(\frac{4}{9}\,\frac{s^2+u^2}{t^2}\right)$
$q_a q_a \to q_a q_a$	$\frac{\pi\alpha_s^2}{s^2}\left[\frac{4}{9}\left(\frac{s^2+u^2}{t^2}+\frac{s^2+t^2}{u^2}\right)-\frac{8}{27}s^2\right]$
$qg \to qg$	$\frac{\pi\alpha_s^2}{s^2}\left[-\frac{4}{9}\left(\frac{s}{u}+\frac{u}{s}\right)+\frac{s^2+u^2}{t^2}\right]$
$gg \to gg$	$\frac{\pi\alpha_s^2}{s^2}\left[\frac{9}{2}\left(3-\frac{tu}{s^2}-\frac{su}{t^2}-\frac{st}{u^2}\right)\right]$

TABLE II

Hodoscopes

Plane	No. of counters	Aperture width x (inches)	Aperture width y (in.)	z-position (in.)	counter width (in.)	counter length (in.)
X1	12	48	60	807.375	4	30
Y1	12	48	60	805.875	5	24
Y2	17	64	68	1114.94	4	32
X3	13	104	92	1836.95	8.665 (4.341)	46
Y3	13	104	92	1847.20	7.00 (7.50)	52
Y4	14	116	100	2035.50	7 (8)	58
X4	16	126	114	2131.12	8 (7)	57

TABLE III

MWPC parameters

plane	z-pos (in.)	width x (in.)	width y (in.)	No.of wires	wire spacing (in.)
U1A	746.777	50.5	59.6	896	.078
Y1A	756.666	50.5	58.88	736	.080
V1A	766.831	50.5	59.6	896	.078
U1B	786.809	50.5	59.6	896	.078
Y1B	776.930	50.5	58.88	736	.080
V1B	796.805	50.5	59.6	896	.078

TABLE IV

Drift chambers

plane	z-pos (in.)	width x (in.)	width y (in.)	No. of wires	wire spacing (in.)
U2	1083.610	66.0	72.0	208	.388
U2'	1085.734	66.0	72.0	208	.388
Y2	1093.015	66.0	70.4	176	.400
Y2'	1095.141	66.0	70.4	176	.400
V2	1103.369	66.0	72.0	208	.388
V2'	1105.493	66.0	72.0	208	.388
U3	1801.404	106.0	95.50	144	.796
U3'	1804.154	106.0	95.50	144	.796
Y3	1811.370	106.0	91.84	112	.820
Y3'	1814.120	106.0	91.84	112	.820
V3	1821.325	106.0	95.50	144	.796
V3'	1824.075	106.0	95.50	144	.796

TABLE V

Calorimeter attenuator settings (dB)

Runs	ETFI	EU/ED	EHI
943-948 (H)	2	4	4
949-981 (H)	2	2	4
986-999 (D)	2	2	6
1015-1016 (D)	2	5	7
1017-1070 (D)	2	3	7
1103-1122 (H)	0	3	7

TABLE VI

Luminosities

Target	protons on target	number of nucleons (cm^{-2})	integrated luminosity (cm^{-2})
LH_2(full)	4.32×10^{14}	8.6×10^{23}	3.7×10^{38}
"(empty)	1.16×10^{14}	4.8×10^{22}	5.6×10^{36}
LD_2(full)	8.25×10^{14}	2.0×10^{24}	1.6×10^{39}
" (empty)	2.63×10^{14}	4.8×10^{22}	1.3×10^{37}

TABLE VII

Event reconstruction cuts

Hydrogen Data (magnets normal)

	EYU	EYD	EHI
N triggers	118,284	76,878	1,117,426
N tracks	73,060	48,659	162,786
N target	626	530	13,302
N ovl	(529)	(392)	--

Hydrogen data (magnets reversed)

	EYU	EYD	EHI
N triggers	58,370	59,130	422,599
N tracks	38,258	41,912	87,899
N target	522	690	7168
N ovl	(163)	(360)	--

Deuterium data

	EYU	EYD	EHI
N triggers	800,268	401,622	1,507,706
N tracks	505,620	264,638	110,132
N targ	5379	5572	28,385
N ovl	(2231)	(1628)	--

TABLE VIII

Fiducial geometry cuts

cut	H_2 data	D_2 data
Target events	21394	35477
$\|x\| > 4$" at calorimeter	18259	31343
$\|y\| > 4.2$" at collimator	16191	27101
$\|x\| < 0.6$" at target	15663	26031
$\|y\| < 1.2$" at target	15054	24968
Trigger efficiency >10%	14501	23286

TABLE IX

Cherenkov identification summary

Hydrogen data

_	π	K	p	No phot	Ambig	Ovflow
Pos.	5428	2160	349	2201	257	69
Neg.	2654	274	20	949	127	13

Deuterium data

_	π	K	p	No phot	Ambig	Ovflow
Pos.	6655	2689	513	1754	340	38
Neg.	8573	830	92	1397	369	35

TABLE X

Misidentification correction factors

Particle	factor
π^+	.98±.01
K^+	.97±.01
p	.70±.05
π^-	1.00±.01
K^-	.82±.03
$\bar{p}$	.67±.06

TABLE XI

Spark Rate Analysis

Non-Spark events (bit not set):

chamber	N events	N identified	% identified
EAST	8190	6439	78.6
WEST	3856	3249	84.3

Spark events (bit set):

chamber	N events	N identified	% identified
EAST	450	269	59.8
WEST	395	223	56.5

TABLE XII

Calorimeter thresholds (EHI trigger, att=7)

counter (R)	E_t(GeV)	counter (L)	E_t(GeV)
1	120.2±8.6	1	129.5±9.9
2	113.9±7.1	2	132.9±10.3
3	101.8±6.5	3	134.7±10.7
4	105.9±7.3	4	129.9±9.5
5	119.0±9.1	5	134.0±8.2
6	123.6±10.7	6	143.9±12.9
7	114.6±11.5	7	130.1±13.8
8	126.8±8.6	8	126.6±9.8
9	120.3±8.3	9	129.6±9.9
10	93.9±9.3	10	110.0±20.0
11	95.1±6.3	11	101.4±8.3
12	91.9±8.8	12	111.4±6.7
13	93.7±7.1	13	107.4±8.3

TABLE XIII

Single particle invariant cross sections

$pp \rightarrow \pi^+ + X$

p_T (GeV/c)	$Ed^3\sigma/dp^3$ ($cm^2 GeV^{-2}$)
5.76	$(3.43\pm0.09)\times10^{-35}$
6.22	$(1.75\pm0.07)\times10^{-35}$
6.71	$(7.40\pm0.43)\times10^{-36}$
7.21	$(3.50\pm0.33)\times10^{-36}$
7.70	$(1.09\pm0.23)\times10^{-36}$
8.20	$(2.97\pm0.69)\times10^{-37}$
8.70	$(6.67\pm3.75)\times10^{-38}$
9.20	$(2.70\pm2.29)\times10^{-38}$

$pp \rightarrow \pi^- + X$

p_T	$Ed^3\sigma/dp^3$
5.75	$(1.78\pm0.07)\times10^{-35}$
6.20	$(8.37\pm0.49)\times10^{-36}$
6.71	$(2.32\pm0.29)\times10^{-36}$
7.21	$(1.28\pm0.18)\times10^{-36}$
7.70	$(3.51\pm0.93)\times10^{-37}$
8.20	$(1.05\pm0.62)\times10^{-37}$
9.20	$(3.14\pm2.00)\times10^{-38}$

TABLE XIII, continued

$pd \rightarrow \pi^+ + X$

p_T	$Ed^3\sigma/dp^3$
6.20	$(1.74\pm0.04)\times10^{-35}$
6.71	$(8.49\pm0.32)\times10^{-36}$
7.21	$(5.73\pm0.26)\times10^{-36}$
7.70	$(1.93\pm0.15)\times10^{-36}$
8.20	$(5.51\pm0.71)\times10^{-37}$
8.70	$(9.46\pm2.94)\times10^{-38}$
9.20	$(5.00\pm2.06)\times10^{-38}$

$pd \rightarrow \pi^- + X$

p_T	$Ed^3\sigma/dp^3$
6.20	$(1.67\pm0.04)\times10^{-35}$
6.71	$(6.88\pm0.29)\times10^{-36}$
7.21	$(3.64\pm0.21)\times10^{-36}$
7.70	$(1.13\pm0.12)\times10^{-36}$
8.20	$(2.60\pm0.50)\times10^{-37}$
8.70	$(8.33\pm4.07)\times10^{-38}$

TABLE XIV

Like-sign particle ratios

Hydrogen data

p_T	K^+/π^+	p/π^+	K^-/π^-	$\bar{p}/\pi^-$
5.35	.468±.028	.198±.011	.112±.019	.023±.017
5.75	.442±.016	.131±.008	.092±.011	.032±.009
6.20	.458±.022	.142±.011	.076±.012	.021±.009
6.71	.430±.034	.110±.015	.044±.025	.022±.019
7.21	.430±.052	.107±.028	.042±.034	.024±.026
7.69	.373±.062	.026±.017	.013±.043	.004±.004
8.20	.378±.153	.038±.042	--	--

Deuterium data

p_T	K^+/π^+	p/π^+	K^-/π^-	$\bar{p}/\pi^-$
5.34	.486±.034	.201±.022	.098±.007	.023±.005
5.76	.453±.017	.128±.008	.088±.005	.018±.003
6.22	.394±.015	.126±.008	.080±.006	.021±.004
6.73	.424±.023	.108±.010	.075±.009	.020±.006
7.22	.409±.027	.107±.012	.043±.009	.031±.012
7.70	.383±.045	.100±.025	.059±.021	.005±.009
8.21	.349±.079	.102±.039	.089±.053	--

TABLE XV

π^+/π^- ratios

P_T	π^+/π^-(H)	π^+/π^-(D)
5.75	2.31±.09	0.92±.03
6.20	2.46±.12	1.03±.03
6.71	2.58±.17	1.21±.05
7.21	2.93±.37	1.62±.09
7.70	3.18±.66	1.80±.17
8.20	2.83±1.13	2.19±.43

TABLE XVI

θ^* dependence

Hydrogen data

K^+/π^+

p_T	$65 < \theta^* < 75°$	$75 < \theta^* < 85°$	$85 < \theta^* < 95°$
5.73	.52±.02	.37±.03	.30±.08
6.20	.46±.03	.47±.04	.32±.06
6.71	.52±.06	.36±.04	.25±.08
7.19	.34±.07	.54±.09	.42±.15
7.70	.42±.11	.35±.09	.33±.12

π^+/π^-

p_T	$65 < \theta^* < 75°$	$75 < \theta^* < 85°$	$85 < \theta^* < 95°$
5.73	2.73±.14	1.76±.13	1.05±.24
6.20	2.77±.20	2.28±.19	2.09±.31
6.71	3.63±.49	2.36±.22	2.19±.43
7.19	3.14±.66	2.95±.60	2.12±.64
7.70	3.18±1.14	3.22±1.02	3.01±1.40

TABLE XVI, continued

Deuterium data

K^+/π^+

p_T	$65 < \theta^* < 75°$	$75 < \theta^* < 85°$	$85 < \theta^* < 95°$
5.75	.46±.02	.38±.03	.56±.13
6.21	.40±.02	.37±.02	.45±.06
6.72	.45±.03	.38±.03	.33±.07
7.20	.42±.04	.42±.04	.37±.06
7.69	.39±.07	.45±.07	.35±.10

π^+/π^-

p_T	$65 < \theta^* < 75°$	$75 < \theta^* < 85°$	$85 < \theta^* < 95°$
6.21	1.20±.05	0.91±.04	0.74±.08
6.72	1.44±.08	1.02±.07	1.08±.16
7.20	2.19±.20	1.38±.11	1.28±.17
7.69	2.91±.56	1.39±.19	1.42±.30
8.22	2.51±.93	2.53±.74	1.54±.61

TABLE XVII

Systematic error estimates

Ratio	σ_R/R(limit of error)
K^+/π^+	.035
K^-/π^-	.052
p/π^-	.121
p/π^-	.134
π^+/π^-	.104

Figure Captions

Figure 1a. Parton model diagram of high-p_T hadron scattering.

Figure 1b. Parton model of deep inelastic lepton-nucleon scattering.

Figure 1c. Parton model of e^+e^- annihilation.

Figure 2. 1st order QCD Feynman diagrams for parton subprocesses important in high-p_T hadron scattering. Shown are diagrams for scattering of identical quarks ($q_a q_a \to q_a q_a$), quarks of different flavors ($q_a q_b \to q_a q_b$), quark-gluon scattering ($qg \to qg$), and gluon-gluon scattering ($gg \to gg$).

Figure 3. Plan and elevation views of the experimental apparatus.

Figure 4. Elevation view of magnets SM0 and SM12, target, collimator, and beam dump.

Figure 5. Schematic view of the wire chamber and hodoscope planes in Stations 1, 2, and 3. Shown in the figure are wire directions and hodoscope segmentation. Not shown are the Station 4 muon identification hodoscope and proportional tube planes.

Figure 6. Schematic view of the calorimeter.

Figure 7. Expected radius vs momentum curves for π, K, and p for refractivity $\eta=75\times10^{-6}$ and mirror focal length 8 m.

Figure 8. Schematic view of the Cherenkov detector, showing Radiator vessel, photon detectors, mirrors, and purification system.

Figure 9. Schematic view of multistep avalanche chamber. Also shown is an illustration of the process by which a photon is detected through photoionization and subsequent electron avalanche.

Figure 10. Block diagram of the Trigger Matrix. The symbol D refers to LeCroy 4416 Discriminators, PS refers to Pulse Stretcher Modules, CR refers to Nevis Coincidence Register cards, and T refers to Trigger Matrix Terminator Modules.

Figure 11. Trigger Matrix card schematic diagram. Shown are line receivers (input from pulse stretcher modules), Random Access Memories, and interconnections to Terminator module and CAMAC system. Not shown are details of CAMAC logic.

Figure 12. Schematic of Fast Trigger Logic and DC Logic system. Symbol D means discriminator, $\sum$ means linear sum, 3/4 means 3-out-of-4 majority logic, and P/S means pre-scaler.

Figure 13. Typical on-line display of a Cherenkov event. Details of figure explained in text (Chapter 3).

Figure 14. Single photon radius histogram. Histogram is fit to gaussian of width σ=1.2 mm.

Figure 15a. Illustration of mirror alignment technique. True center of circle is at '·'; preliminary guess for center of circle is at '+'. Photon '*' is measured to have radius r and angle ϕ with respect to '+' center; true radius is r_0.

Figure 15b. Plot of measured radius r vs angle ϕ. Dashed curve is for situation when true circle center is known. Solid curve (see equation 4.7) is for situation when mirror is misaligned and circle center is not known.

Figure 16. Position of y-coordinate of ring center vs time for a typical mirror.

Figure 17. Distribution of measured refractivity n^2-1 using ring radii from muon tracks.

Figure 18. Refractivity n^2-1 vs time.

Figure 19. Distribution in number of detected photons for each particle type π, K, and p.

Figure 20a. Monte Carlo calculation of photon reconstruction efficiency vs number of generated photons. Error bars are Monte Carlo statistical errors.

Figure 20b. Monte Carlo calculation of dependence of parameter b (from equation 4.9) on two-photon minimum separation.

Figure 21. Distribution of distance between two nearest photons in an event. Separate histograms are shown for east and west chambers.

Figure 22. Histograms of mean number of photons n_0 vs run number. Separate histograms are shown for east and west chambers and for hydrogen and deuterium runs.

Figure 23. Histograms of live factor λ vs run number. Separate histograms are shown for east and west chambers and for hydrogen and deuterium runs.

Figure 24. Histogram showing fraction of prescaled triggers (ETFI) satisfying EHI trigger as a function of energy. This histogram is for a typical calorimeter counter.

Figure 25. Average trigger efficiency for the EHI trigger with attenuator setting of 7 dB. Solid curve is for negative particles, and dashed curve is for positives.

Figure 26. Contributions to single pion cross section from parton subprocesses $qq \rightarrow qq$, $qg \rightarrow qg$, and $gg \rightarrow gg$. Figure taken from ref. [40].

Figure 27. Single pion invariant cross sections.

Figure 28. K^+/π^+ ratio, hydrogen data, as measured by this experiment (E605, black circles) and Chicago-Princeton (CP, open circles). Superimposed on the experimental points in Figures 28-37 are theoretical curves for standard Lund Monte Carlo (solid curve), and modified Lund (P(s)/P(u)=0.5, P(qq)/P(q)=0.05, dashed curve).

Figure 29. p/π^+ ratio, hydrogen data.

Figure 30. K^-/π^- ratio, hydrogen data.

Figure 31. $\bar{p}/\pi^-$ ratio, hydrogen data.

Figure 32. π^+/π^- ratio, hydrogen data.

Figure 33. K^+/π^+ ratio, deuterium data. as measured by this experiment

Figure 34. p/π^+ ratio, deuterium data.

Figure 35. K^-/π^- ratio, deuterium data.

Figure 36. $\bar{p}/\pi^-$ ratio, deuterium data.

Figure 37. π^+/π^- ratio, deuterium data.

Figure 38. K^+/π^+ ratio, hydrogen data, binned according to θ^*. Dark circles are for $65<\theta^*<75°$, open circles are for $75<\theta^*<85°$, and triangles are for $85<\theta^*<95°$. Curves in Figures 38-41 are predictions from modified Lund Monte Carlo (P(s)/P(u) = 0.5, P(qq)/P(q) = 0.05).

Figure 39. π^+/π^- ratio, hydrogen data, binned according to θ^*.

Figure 40. K^+/π^+ ratio, deuterium data, binned according to θ^*.

Figure 41. π^+/π^- ratio, deuterium data, binned according to θ^*.

Figure 42. Ratio of u-quark to d-quark structure functions vs x, with Q^2 fixed at 64 GeV^2. Solid curve is EHLQ parameterization [14], and dashed curve is Duke-Owens parameterization [12].

Figure 43. Ratio of gluon to u-quark structure functions vs x, at fixed Q^2 = 64 GeV^2. Solid curve is EHLQ[14], dashed curve is Duke-Owens[12].

Figure 44a. Lund Monte Carlo predictions superimposed on particle ratio measurements, hydrogen data. Solid curves in Figures 44 a and b are modified Lund (same as dashed curve of Figures 28-37), and dashed curves are modified Lund but with no gluon radiation.

Figure 44b. Lund Monte Carlo predictions for deuterium data.

Figure 45a. Lund Monte Carlo structure function comparison, hydrogen data. Solid curves in Figures 45 a and b are modified Lund plus no gluon radiation, EHLQ structure functions. Dashed curves are with same parameters but using Duke-Owens structure functions.

Figure 45b. Lund Monte Carlo structure function comparison, deuterium data.

Figure 46a. Lund Monte Carlo Q^2 study, hydrogen data. Solid curves in Figures 46 a and b are same as dashed curves in Figure 45, and correspond to defining Q^2 according to equation (1.3). Dashed curves use definition of equation (5.9).

Figure 46b. Lund Monte Carlo Q^2 study, deuterium data.

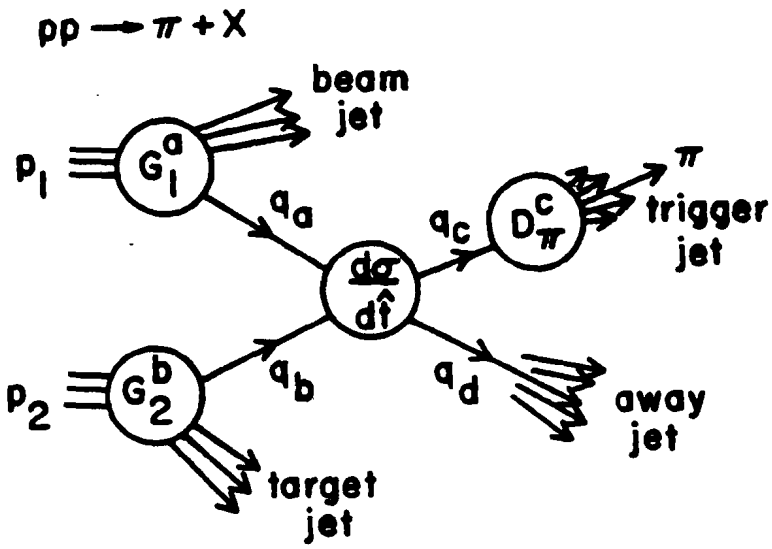
pp → π + X
beam jet
p1
G1a
qa
qc
Dcπ
π
trigger jet
dσ/df̂
p2
G2b
qb
qd
away jet
target jet

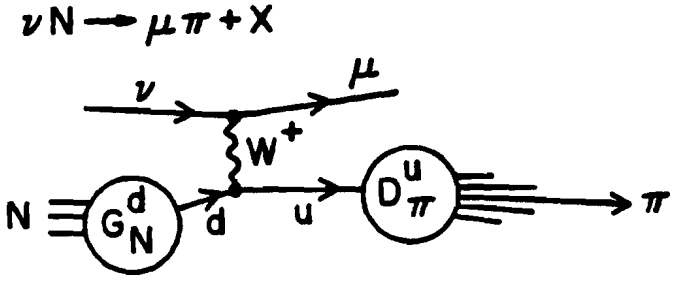
νN → μπ + X
ν
μ
W+
N
GNd
d
u
Dπu
π

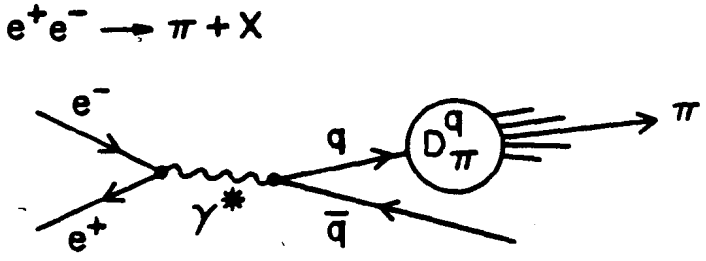
e+e− → π + X
e−
q
Dπq
π
e+
γ*
q̄

Figure 1

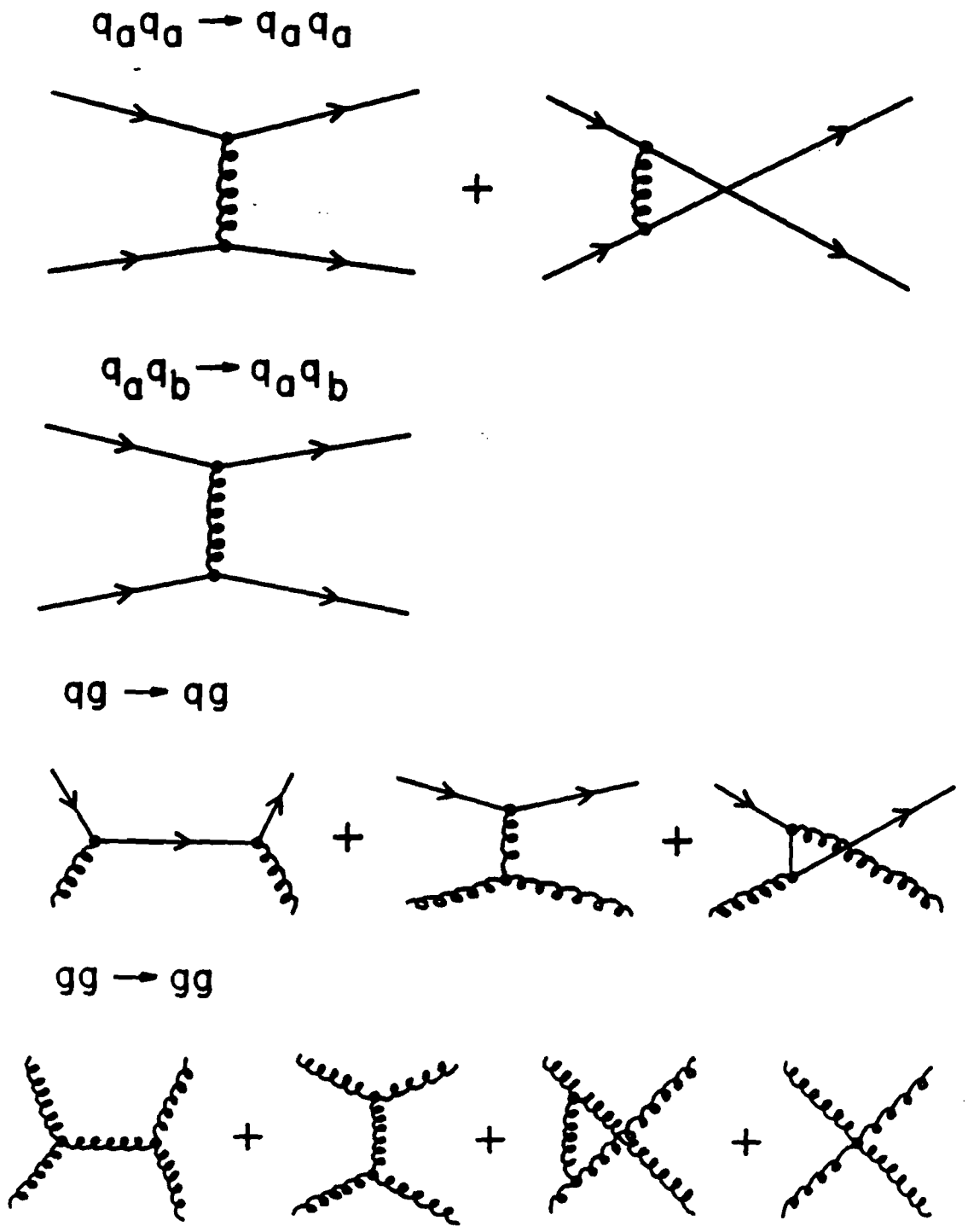

Figure 2

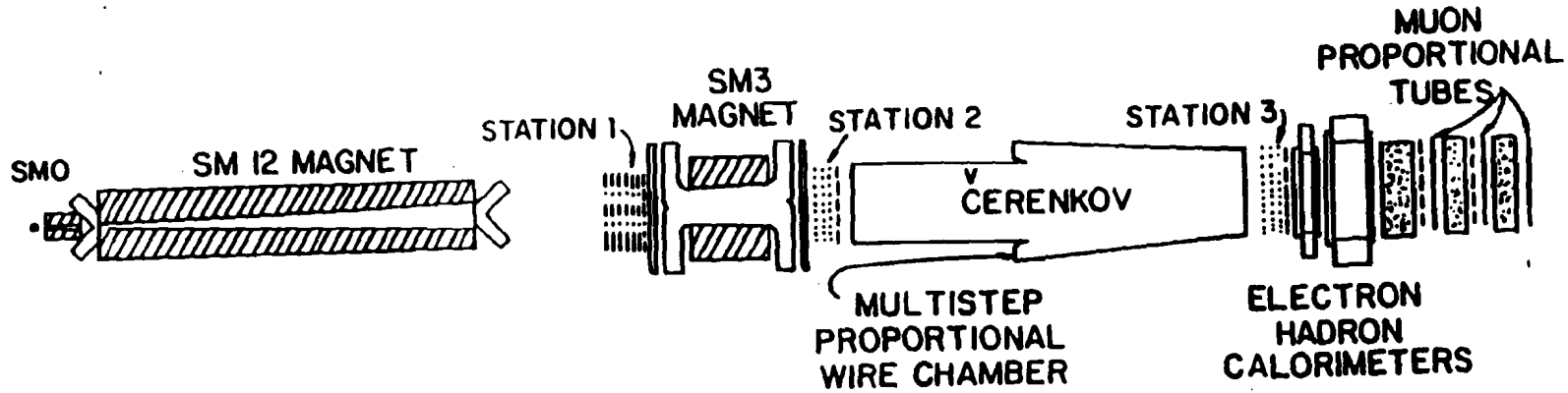

PLAN VIEW E-605

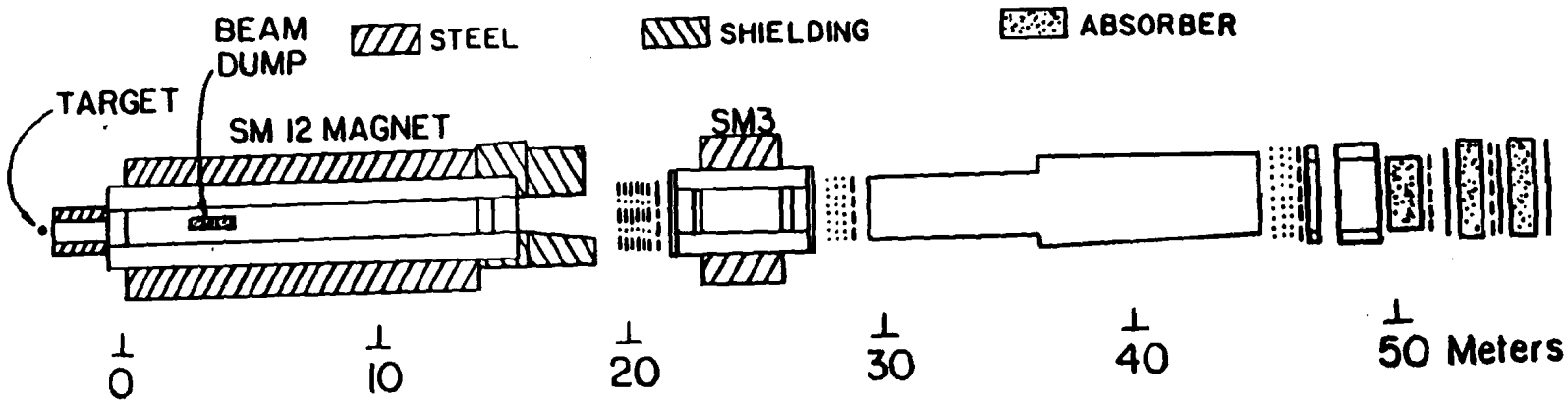

ELEVATION SECTION E-605

..... DRIFT CHAMBER

-.-.- PROPORTIONAL CHAMBER

----- COUNTER BANK

Figure 3

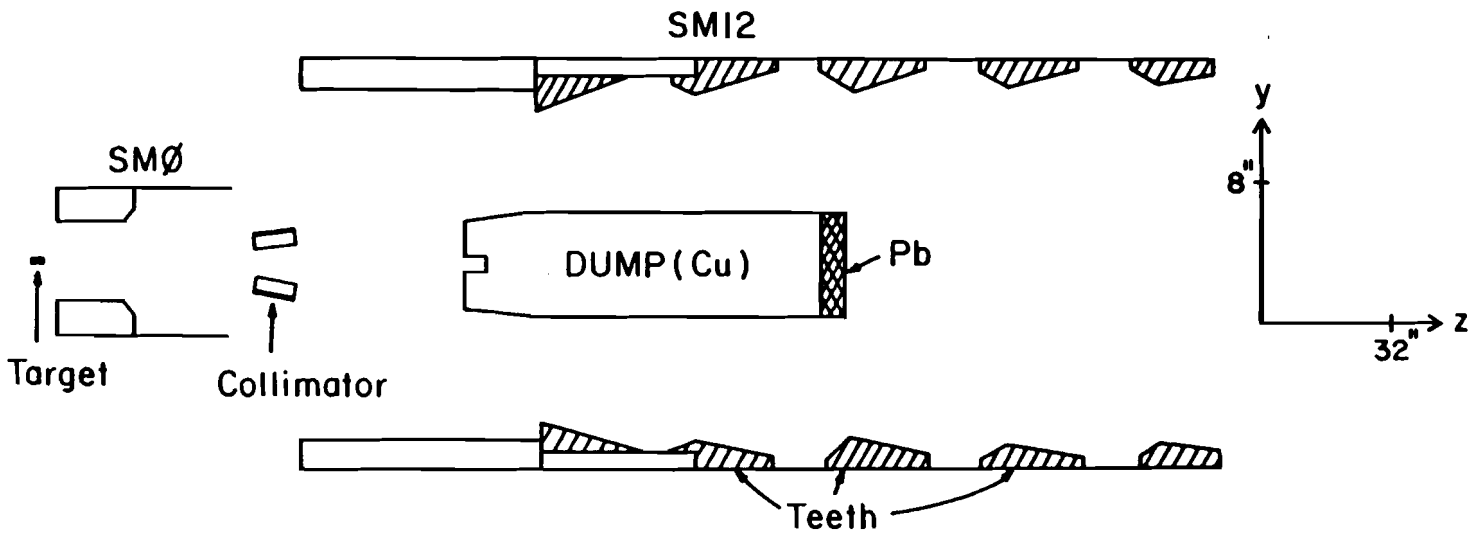

Figure 4

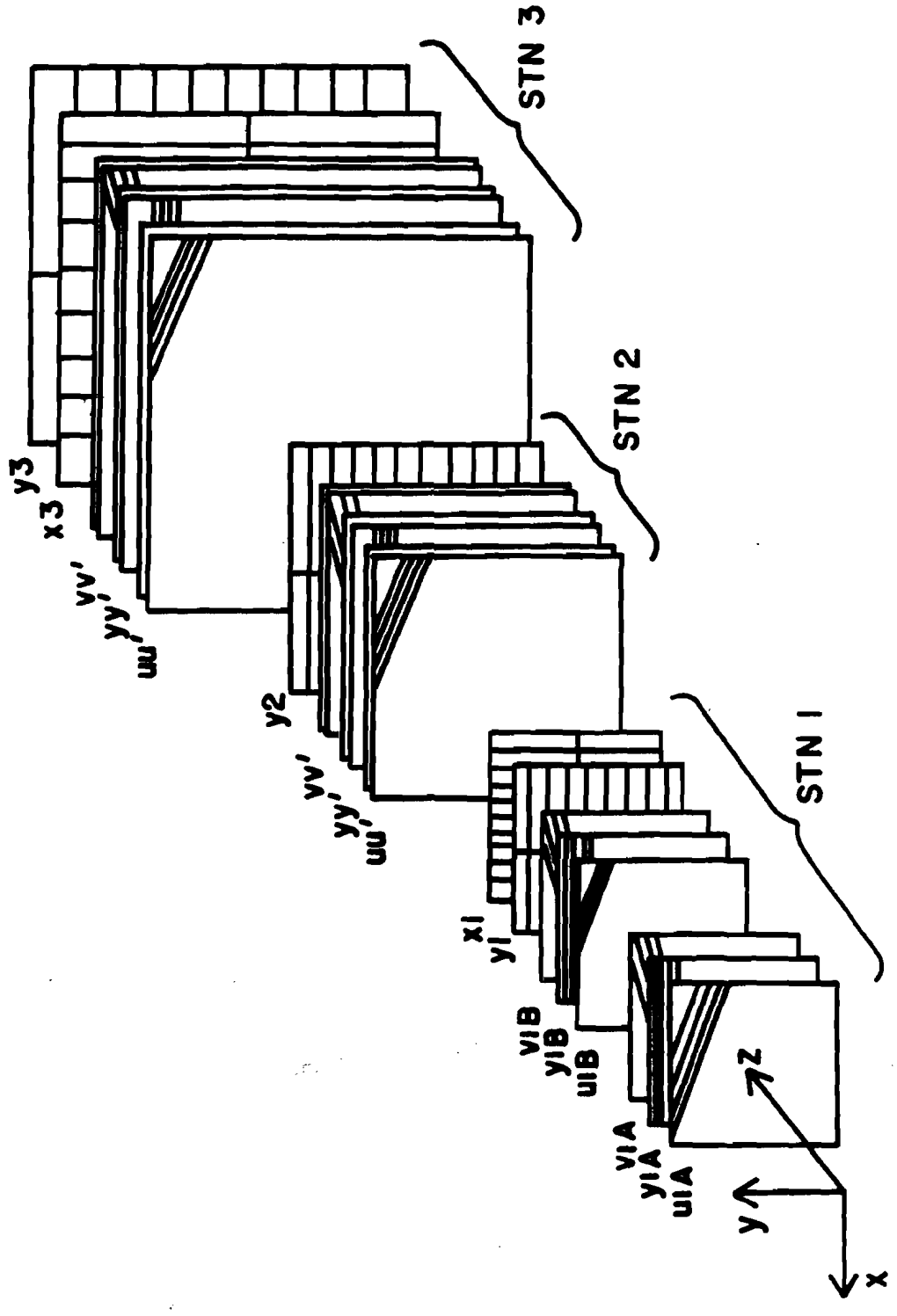
STN 3
STN 2
STN 1
y3
x3
vv'
yy'
uu'
y2
vv'
yy'
uu'
x1
y1
viB
yiB
uiB
viA
yiA
uiA
z
y
x

Figure 5

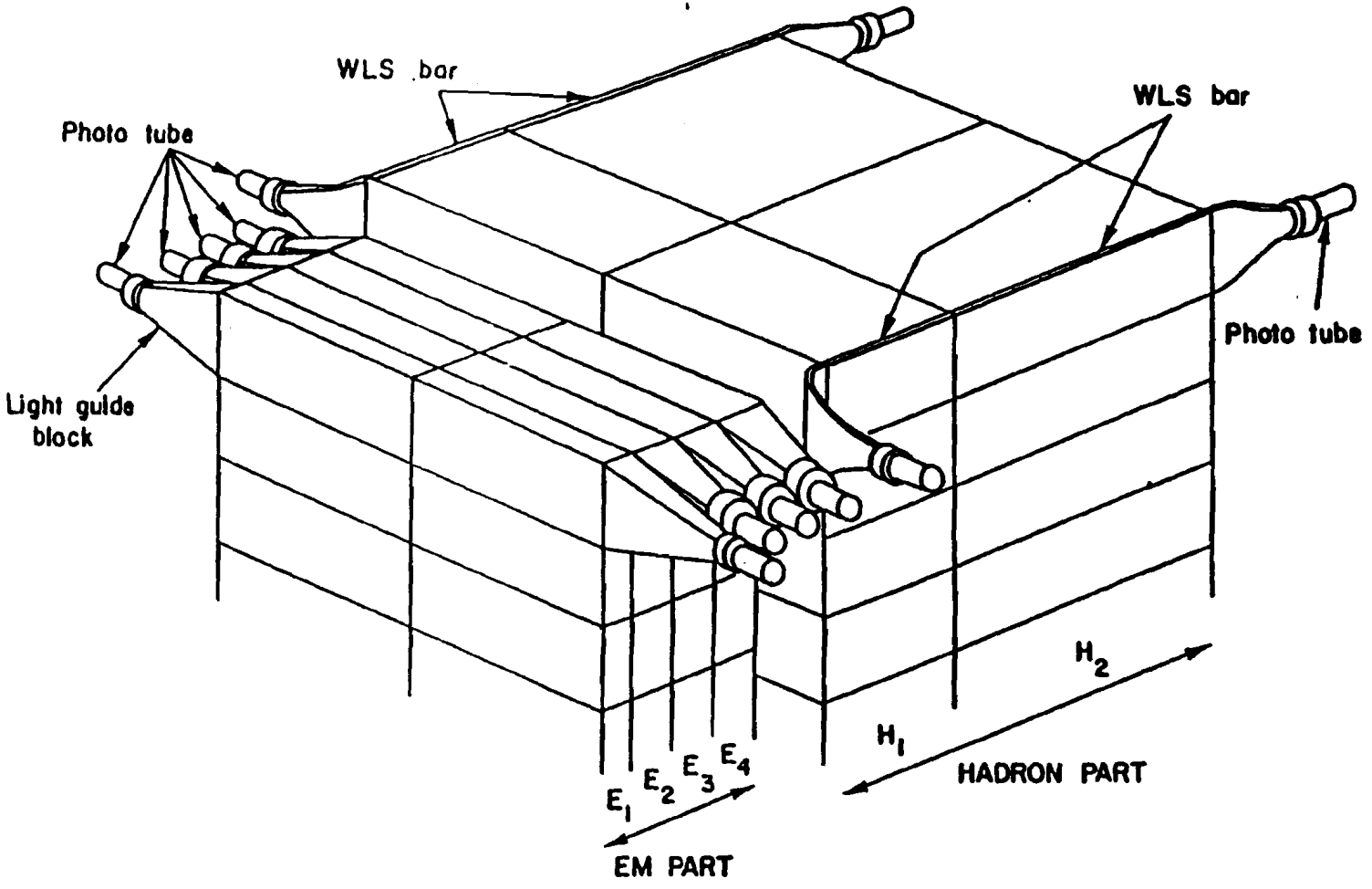
WLS bar
WLS bar
Photo tube
Photo tube
Light guide block
H_2
H_1
HADRON PART
E_1 E_2 E_3 E_4
EM PART

Figure 6

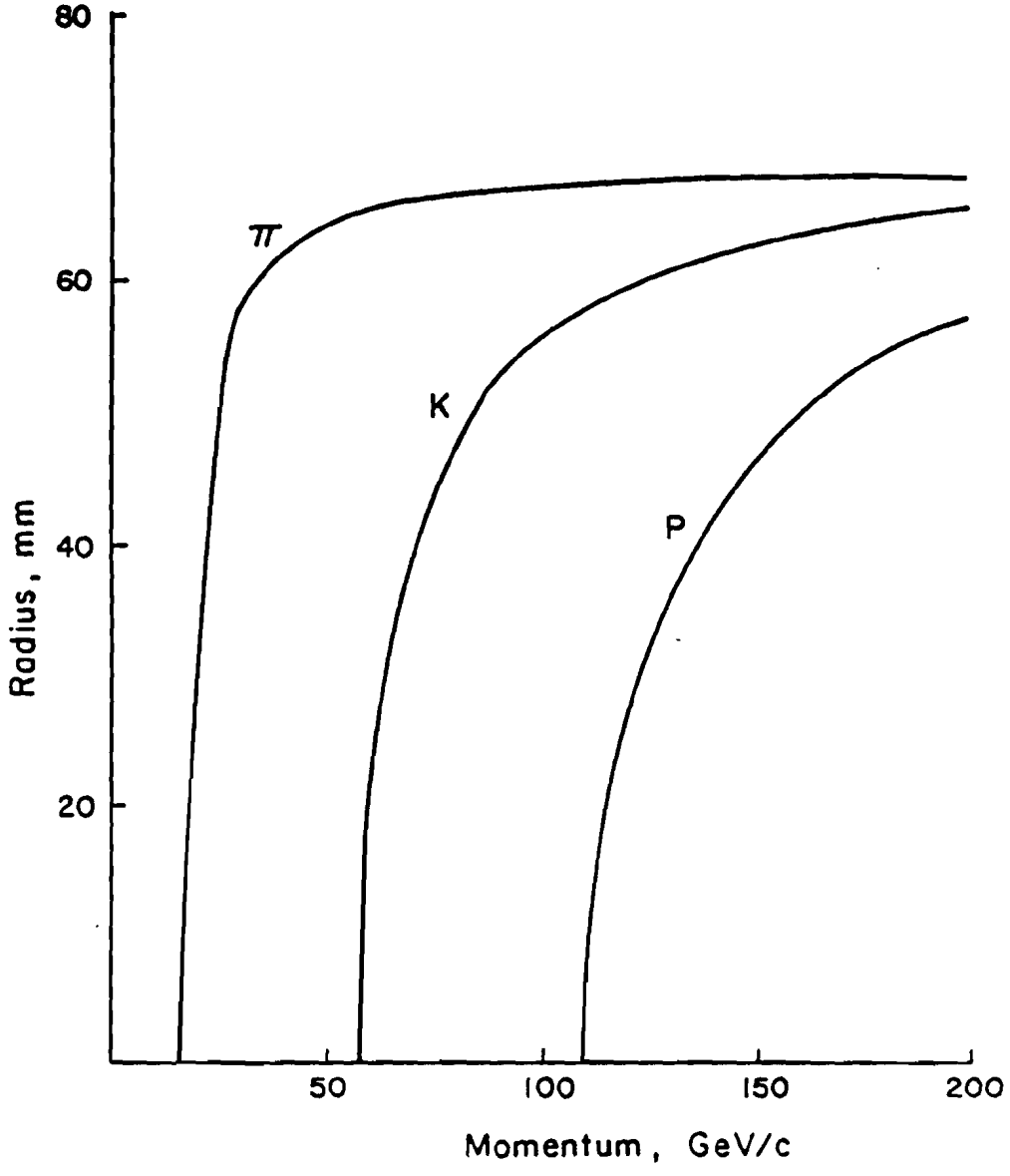

Figure 7

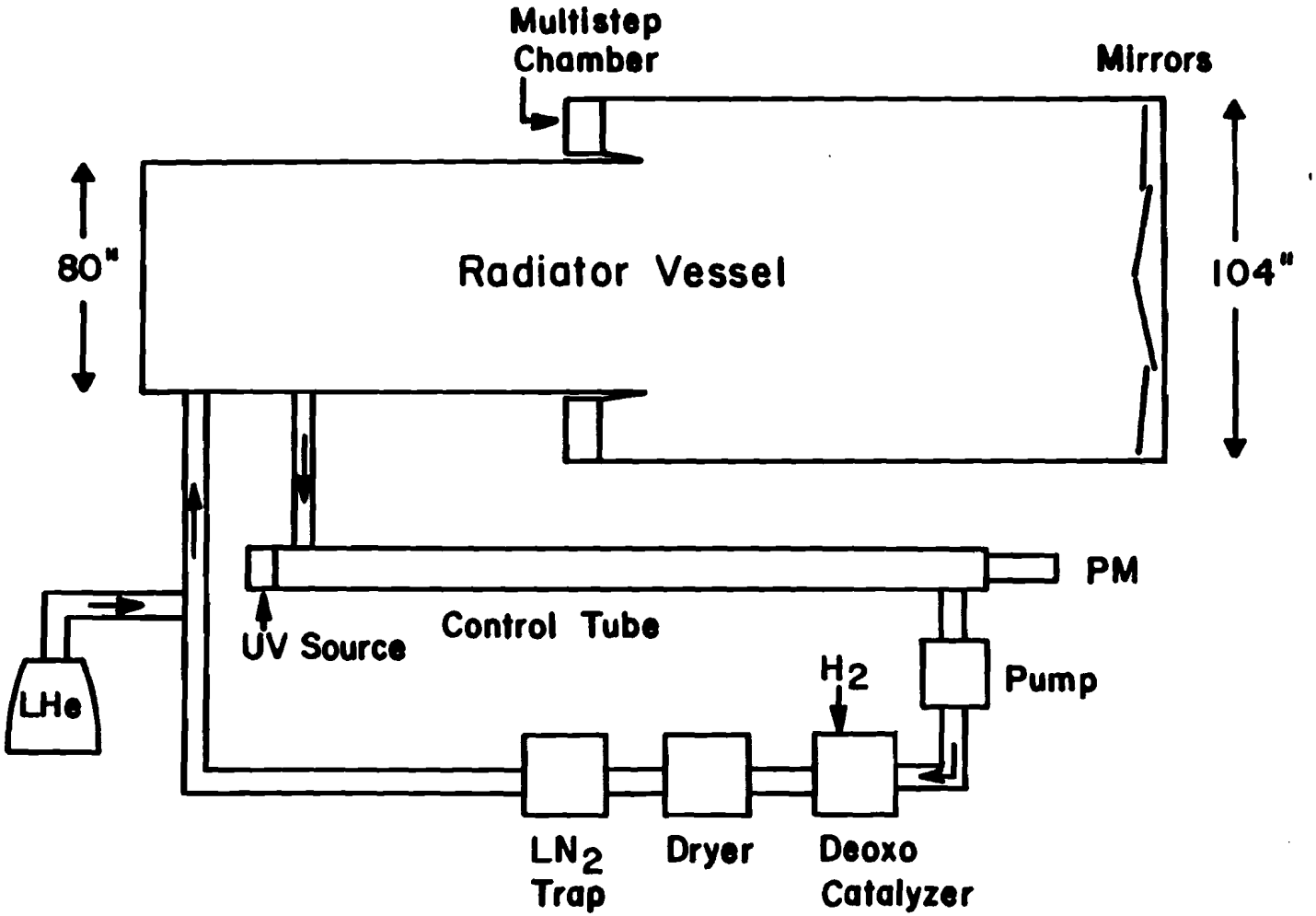
Multistep
Chamber
Mirrors
80"
Radiator Vessel
104"
PM
UV Source
Control Tube
LHe
H2
Pump
LN2
Trap
Dryer
Deoxo
Catalyzer

Figure 8

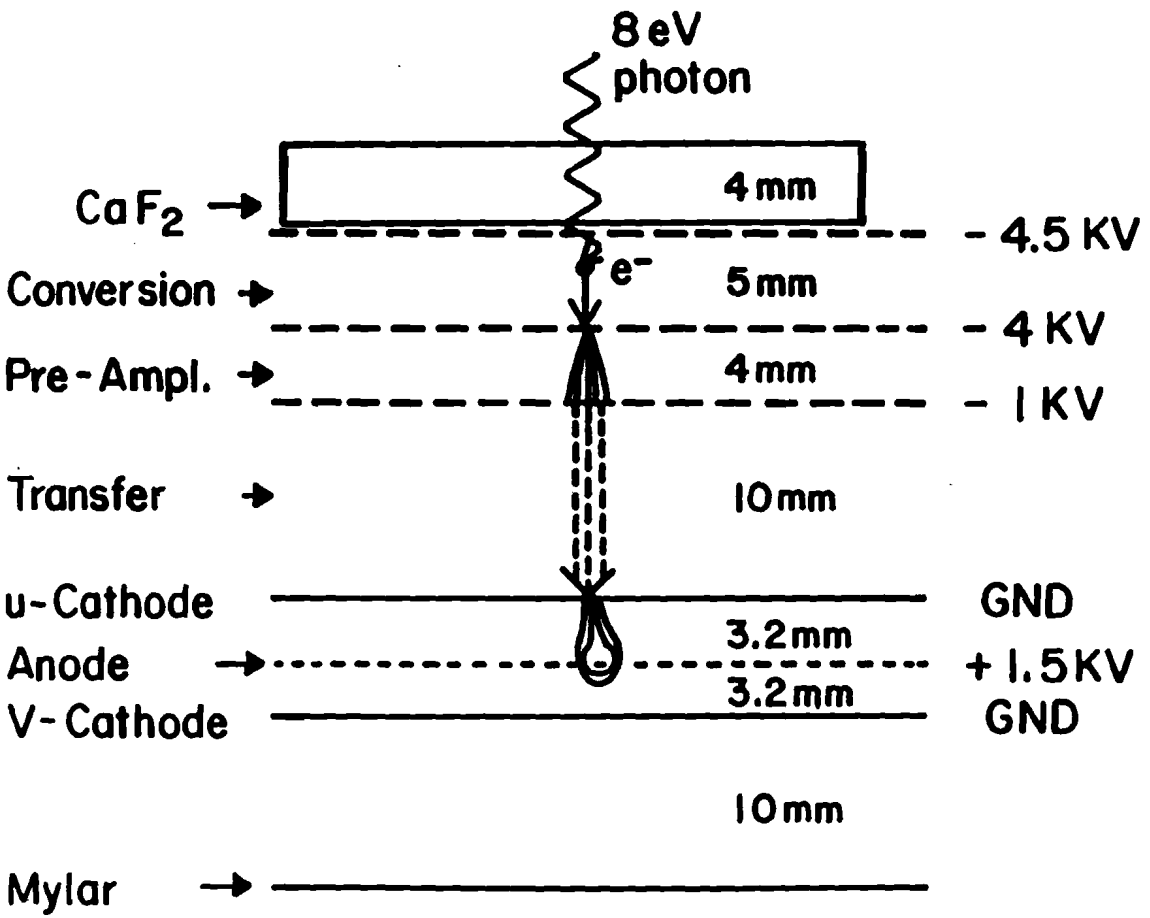
8 eV
photon
4 mm
CaF_2
- 4.5 KV
e^-
5 mm
Conversion
- 4 KV
4 mm
Pre-Ampl.
- 1 KV
Transfer
10 mm
u-Cathode
GND
3.2 mm
Anode
+ 1.5 KV
3.2 mm
V-Cathode
GND
10 mm
Mylar

Figure 9

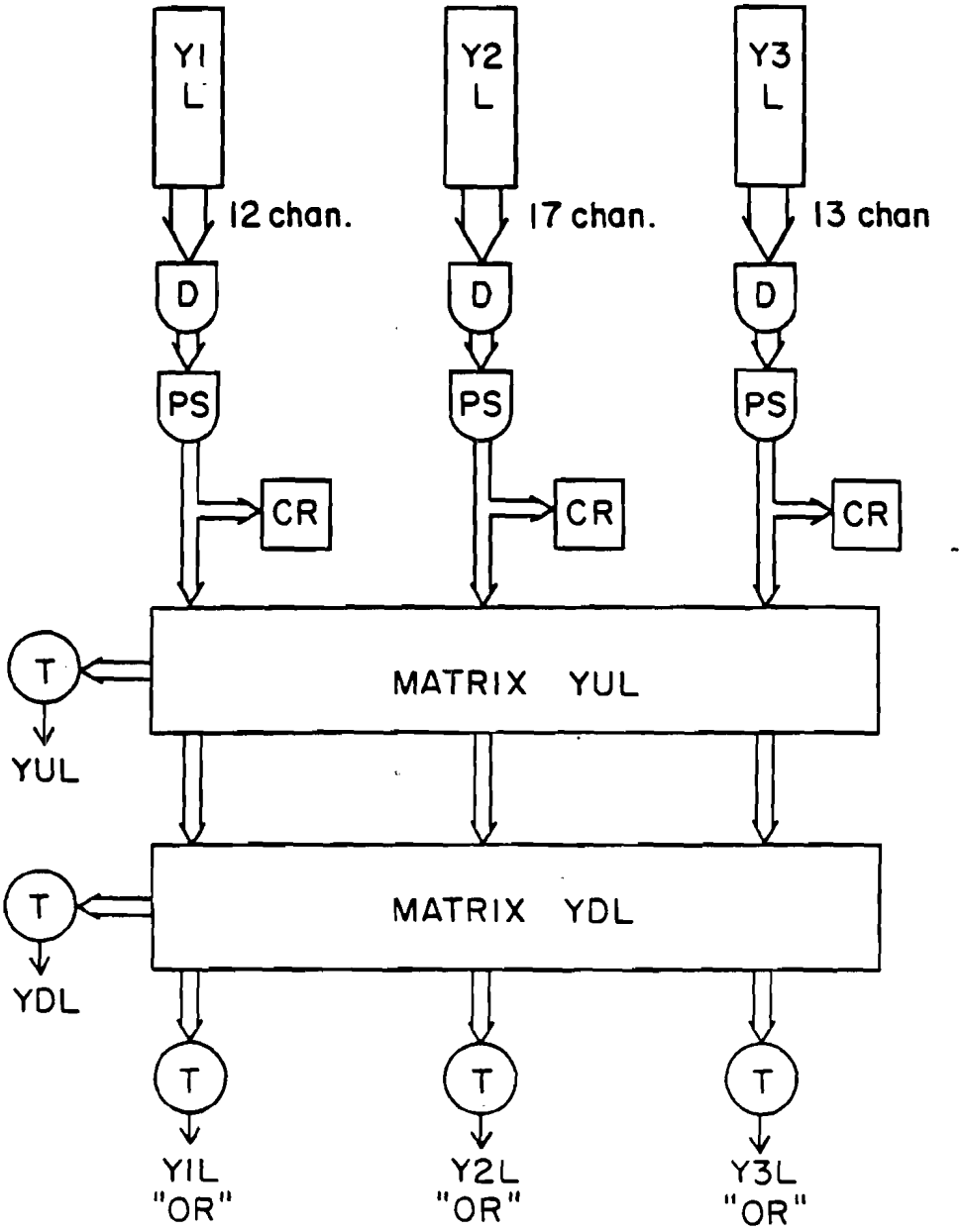
Y1 L
Y2 L
Y3 L
12 chan.
17 chan.
13 chan
D
D
D
PS
PS
PS
CR
CR
CR
T
MATRIX YUL
YUL
T
MATRIX YDL
YDL
T
T
T
Y1L "OR"
Y2L "OR"
Y3L "OR"

Figure 10

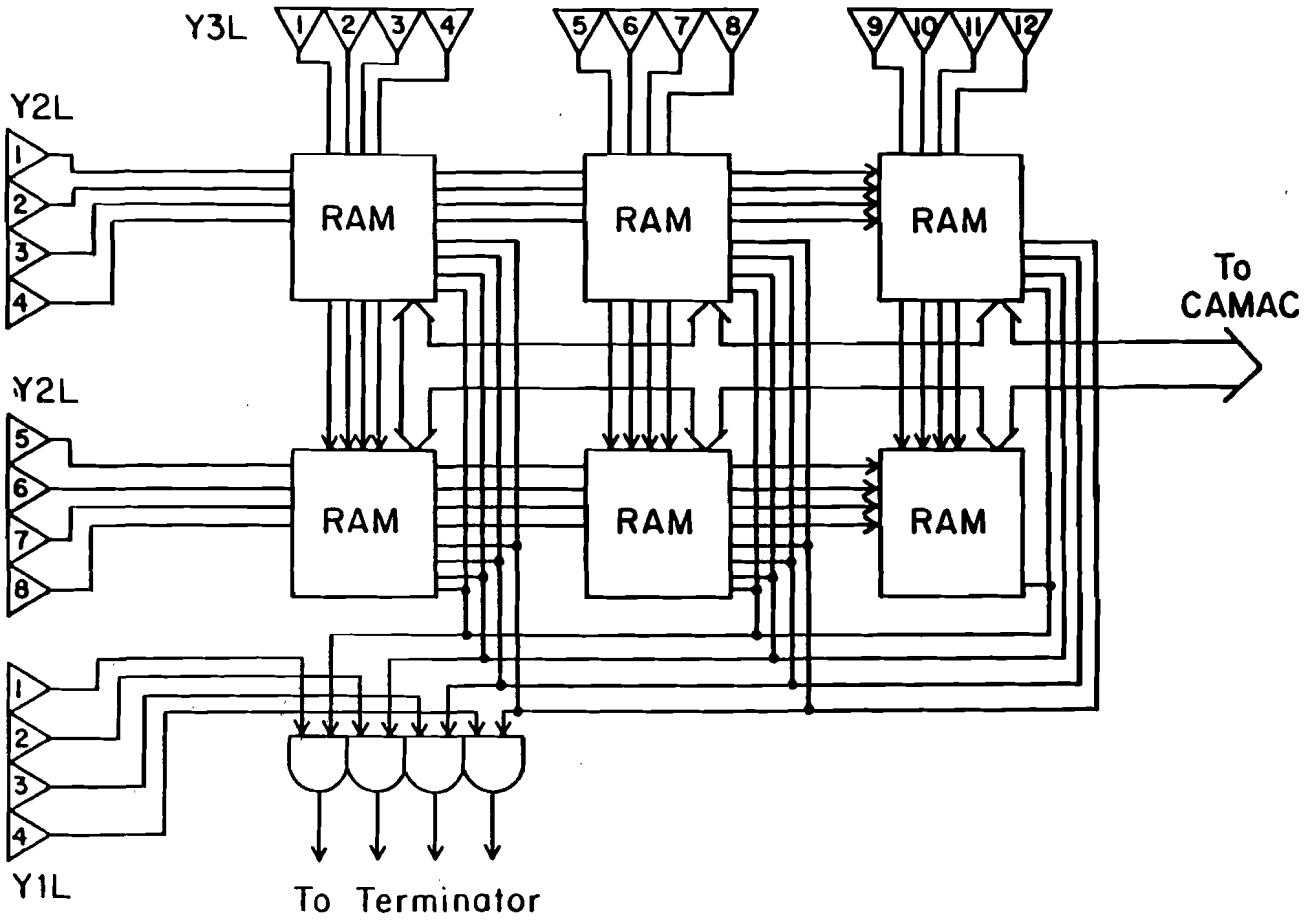
Y3L
1
2
3
4
5
6
7
8
9
10
11
12
Y2L
1
2
3
4
RAM
RAM
RAM
To
CAMAC
Y2L
5
6
7
8
RAM
RAM
RAM
1
2
3
4
Y1L
To Terminator

Figure 11

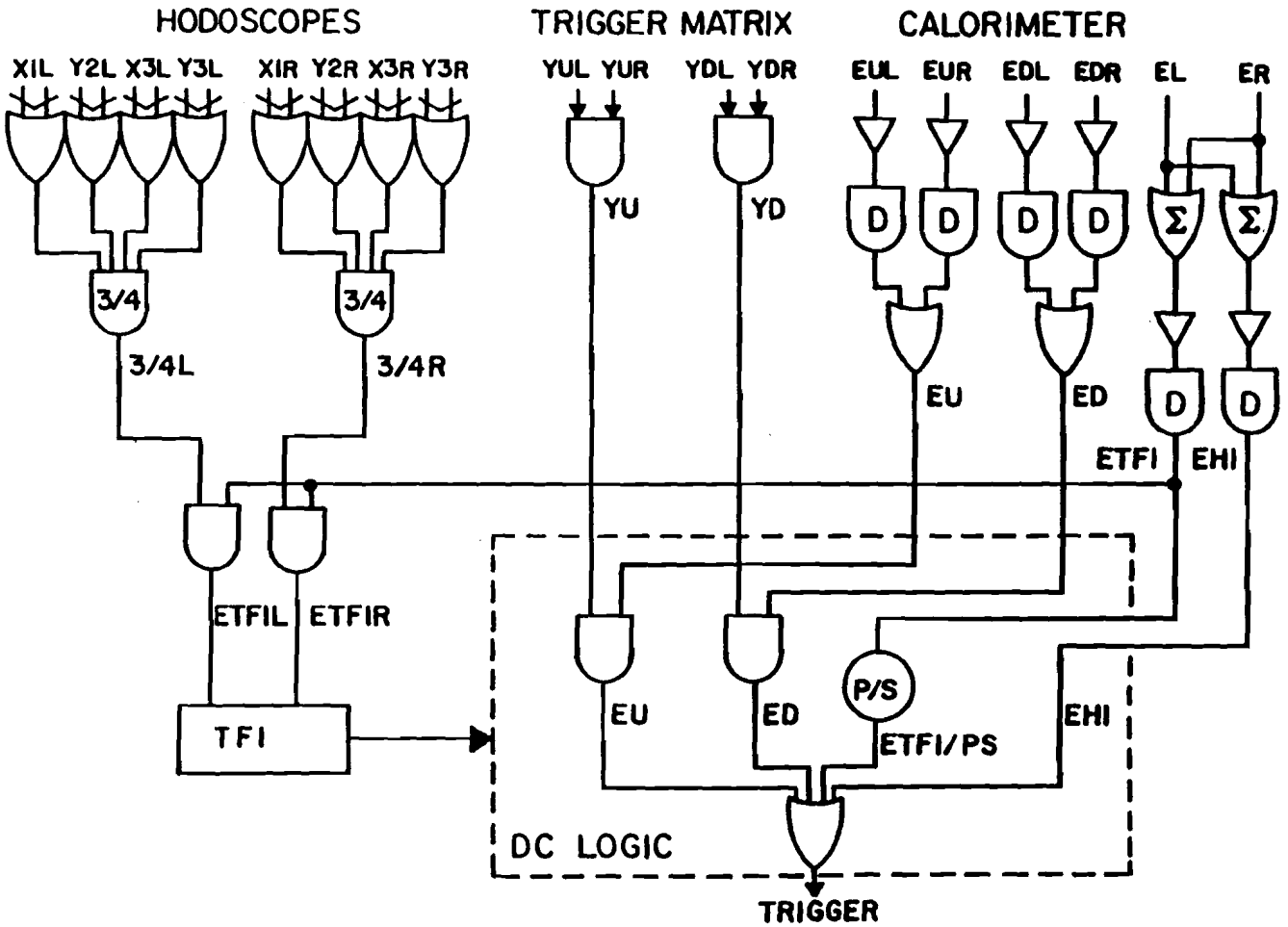
HODOSCOPES
TRIGGER MATRIX
CALORIMETER
XIL Y2L X3L Y3L
XIR Y2R X3R Y3R
YUL YUR
YDL YDR
EUL EUR EDL EDR EL ER
3/4
3/4
3/4L
3/4R
YU
YD
D
Σ
EU
ED
ETFI
EHI
ETFIL ETFIR
TFI
P/S
ETFI/PS
DC LOGIC
TRIGGER

Figure 12

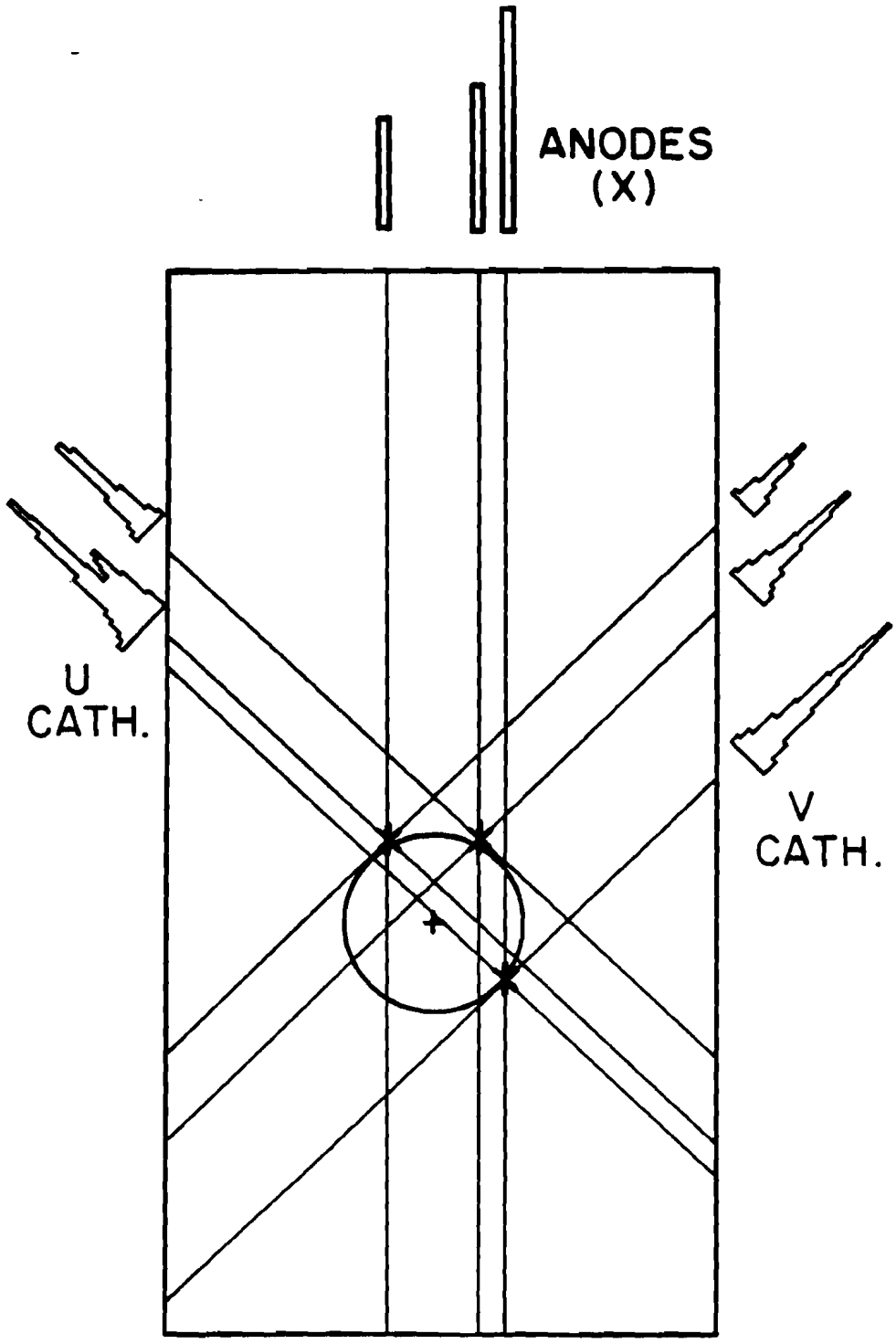

Figure 13

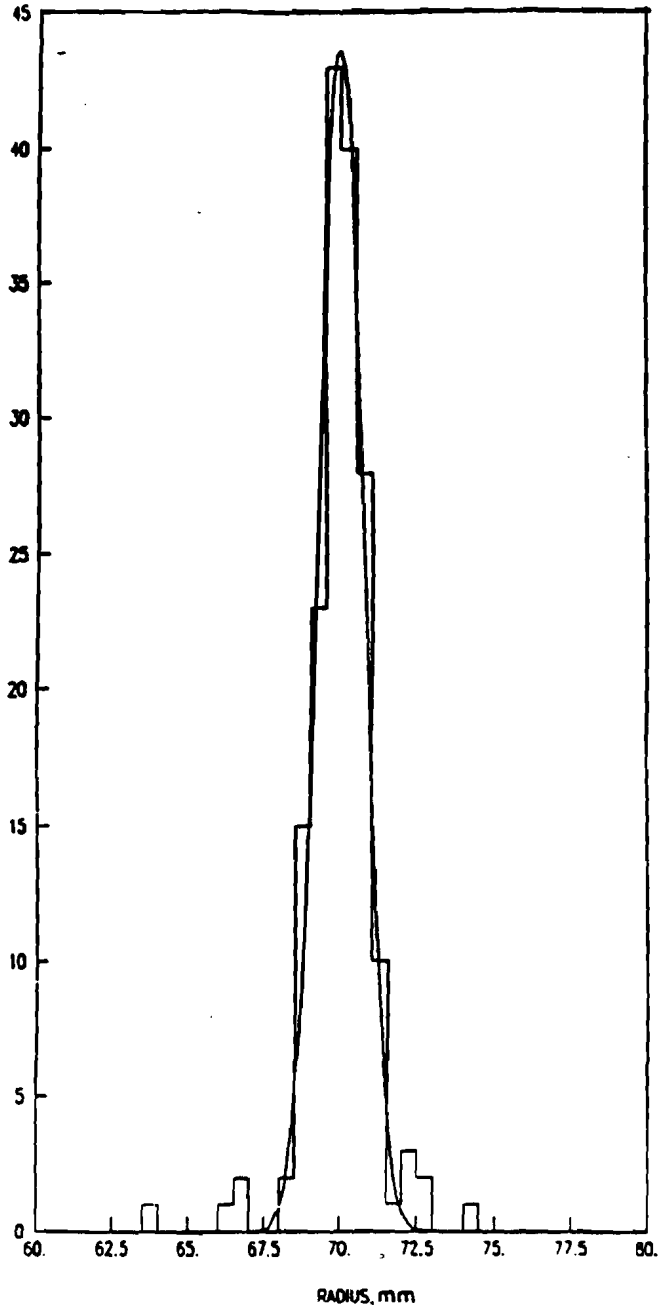

Figure 14

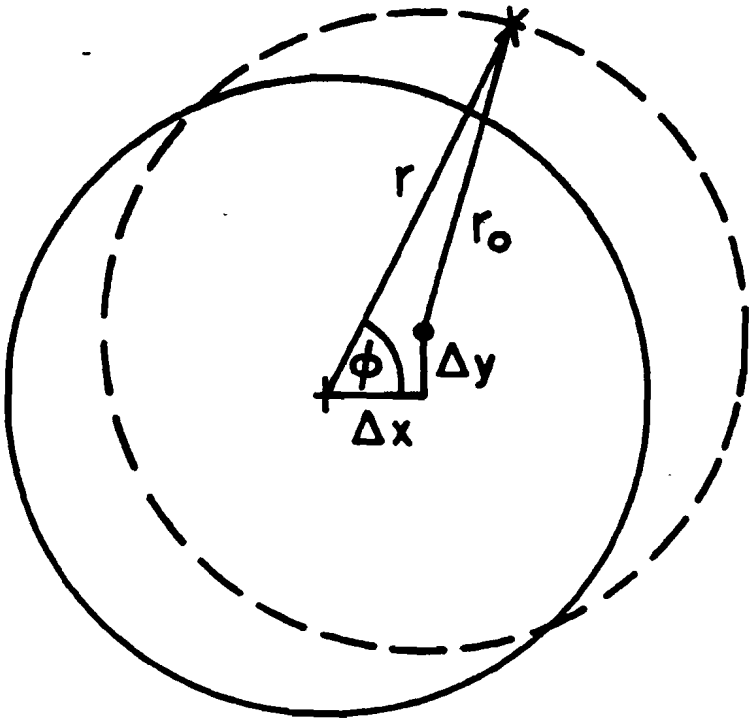

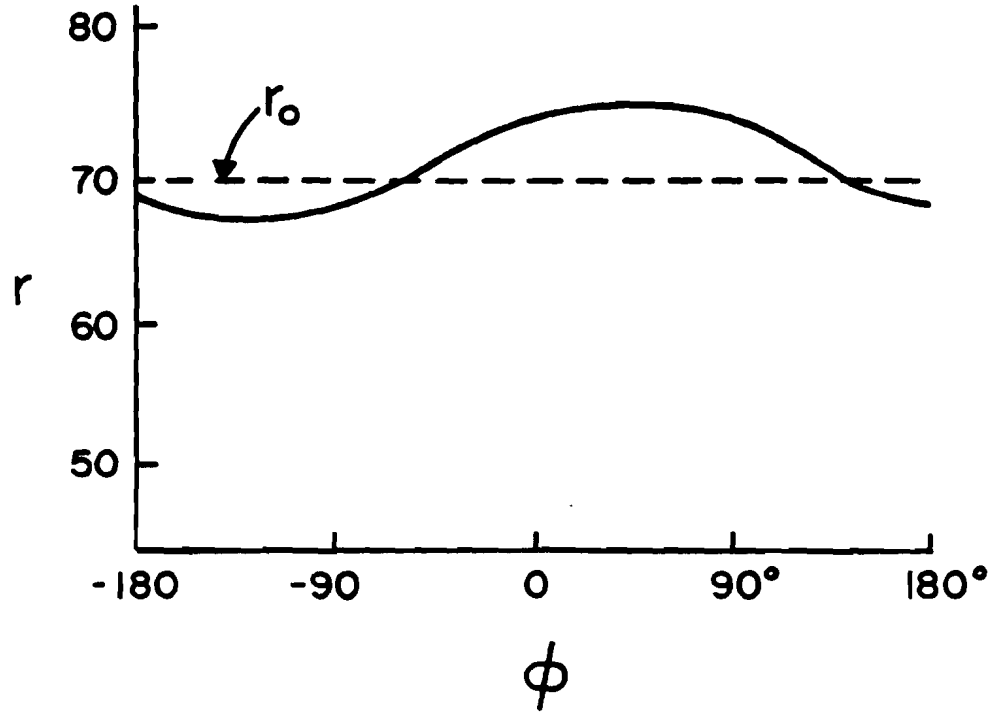

Figure 15

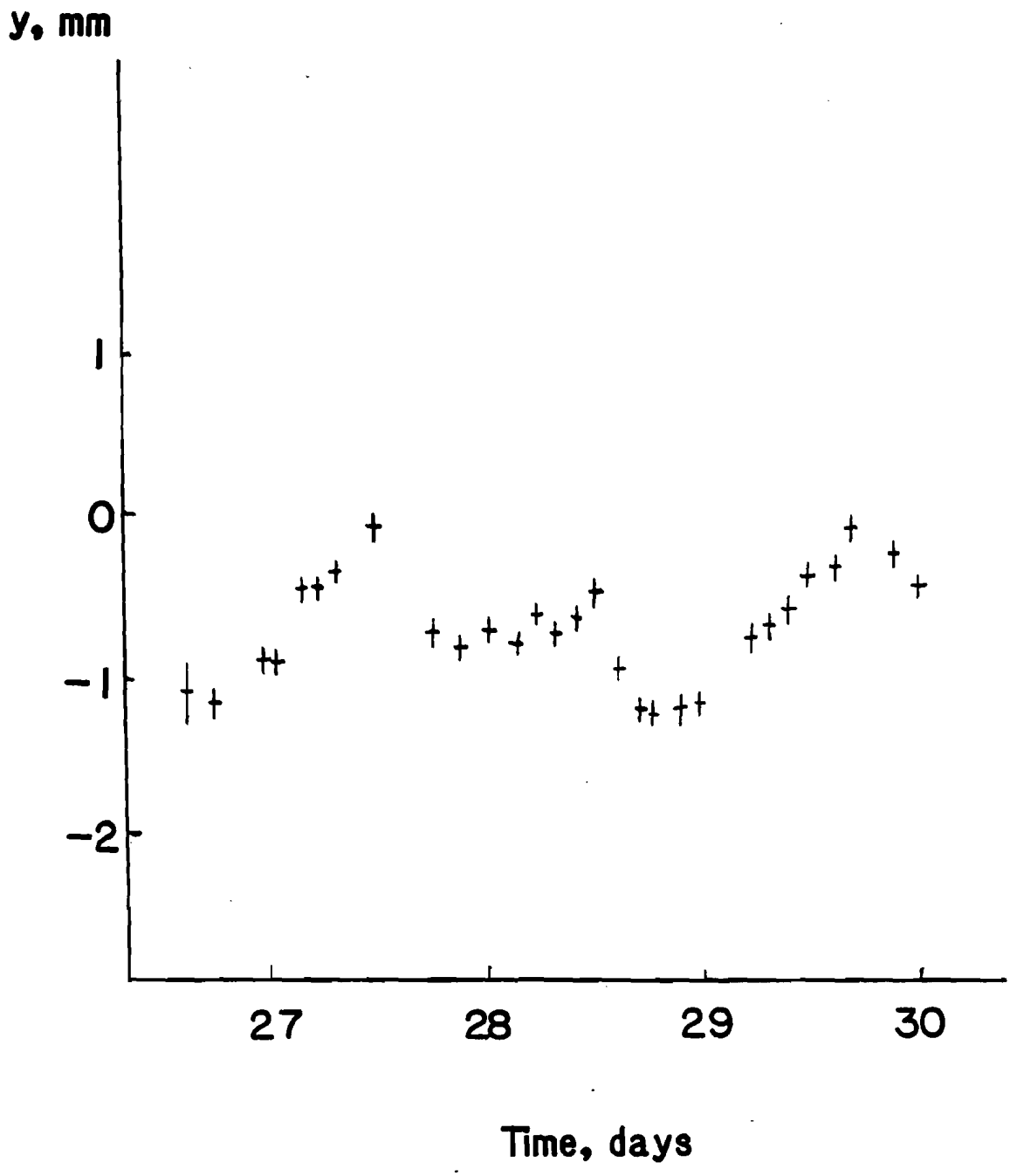

Figure 16

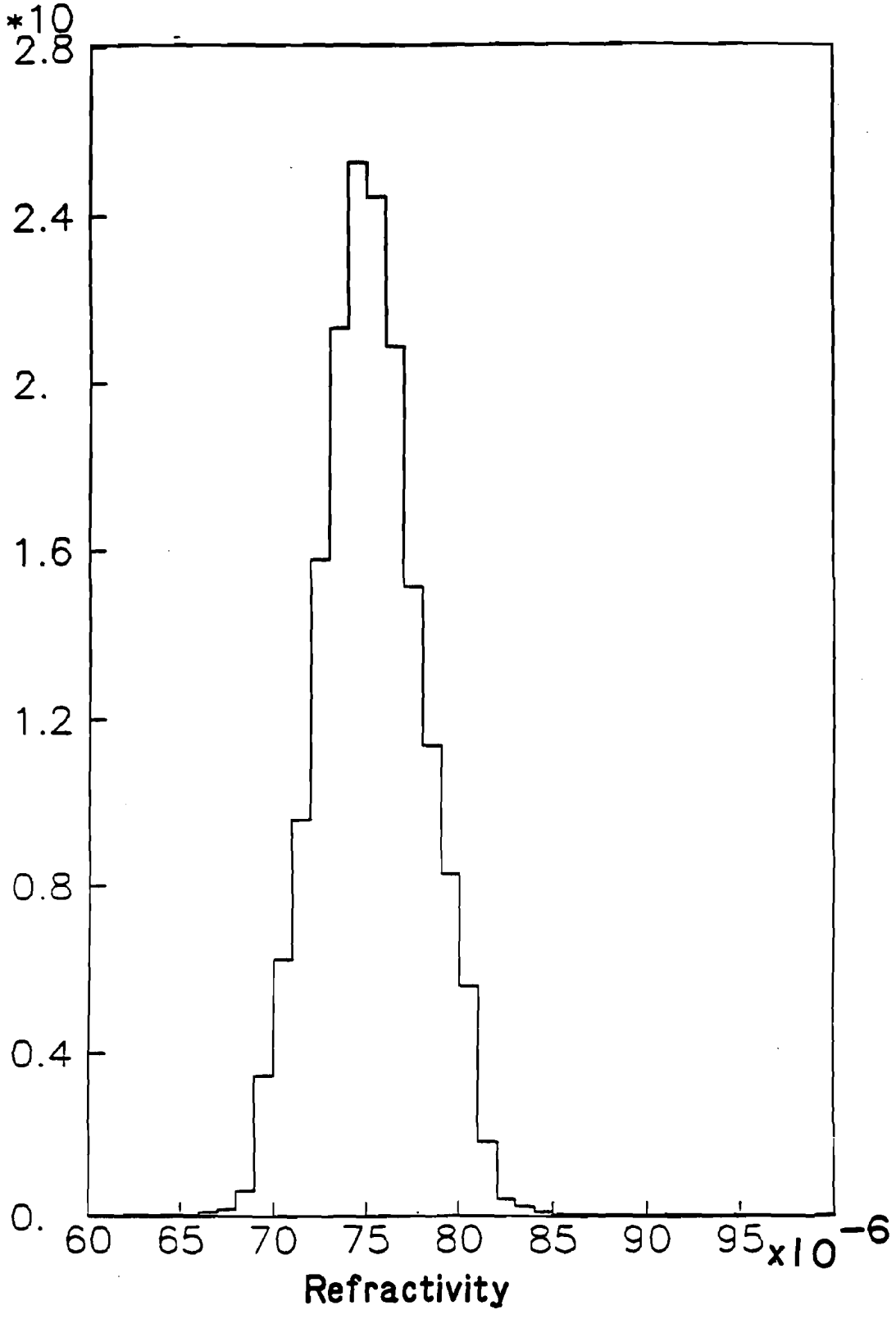

Figure 17

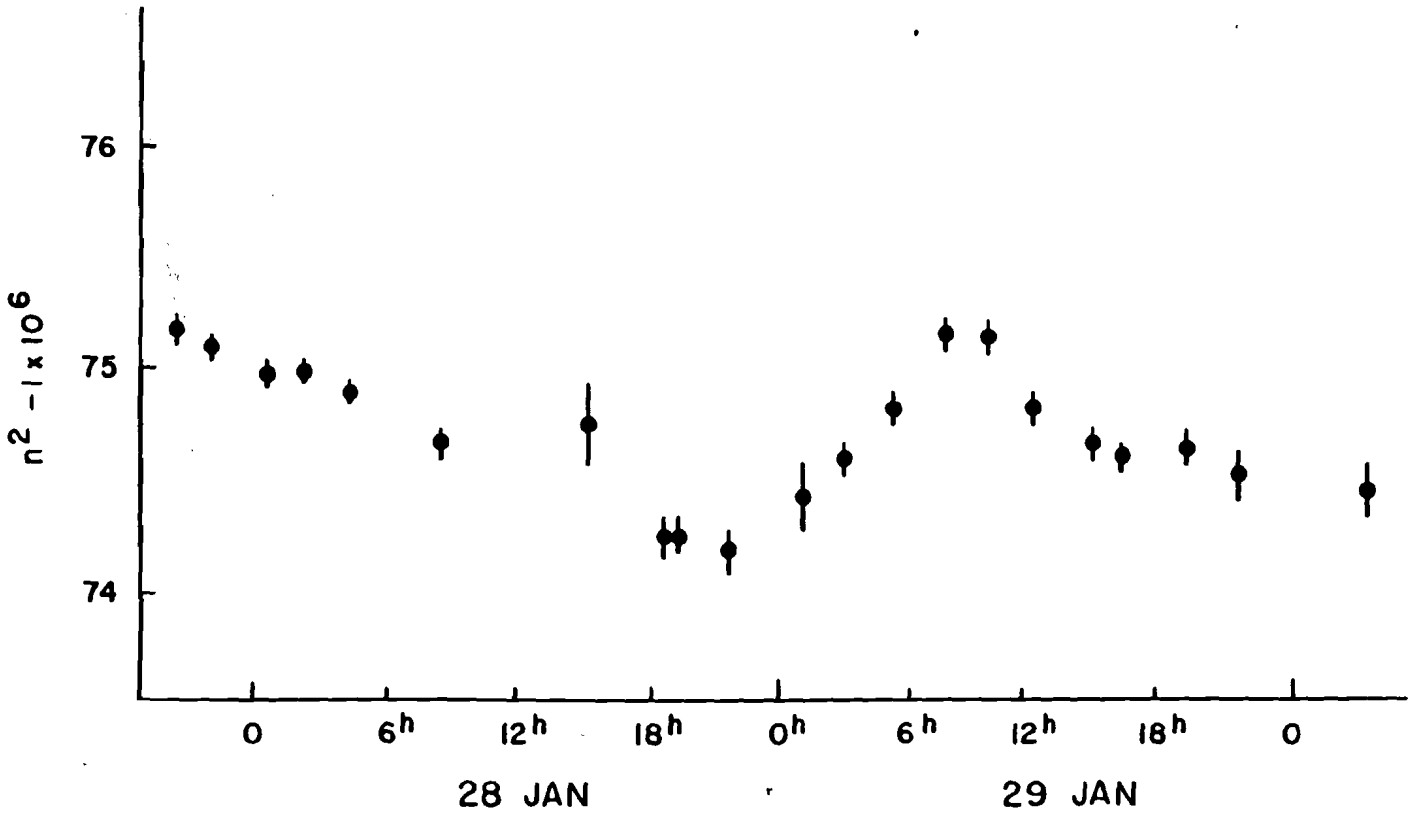

Figure 18

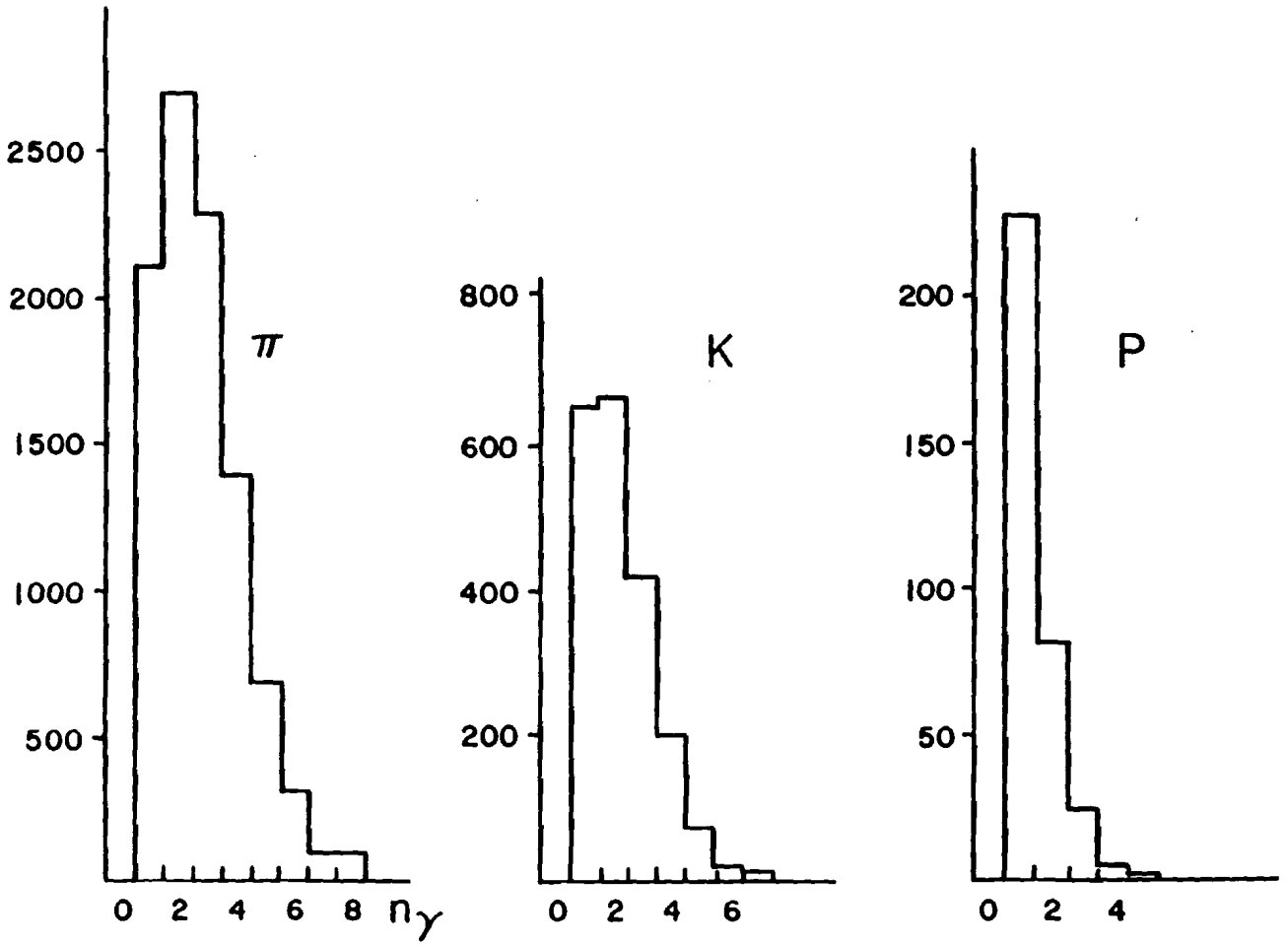
2500
2000
1500
1000
500
π
0 2 4 6 8 nγ
800
600
400
200
K
0 2 4 6
200
150
100
50
P
0 2 4

Figure 19

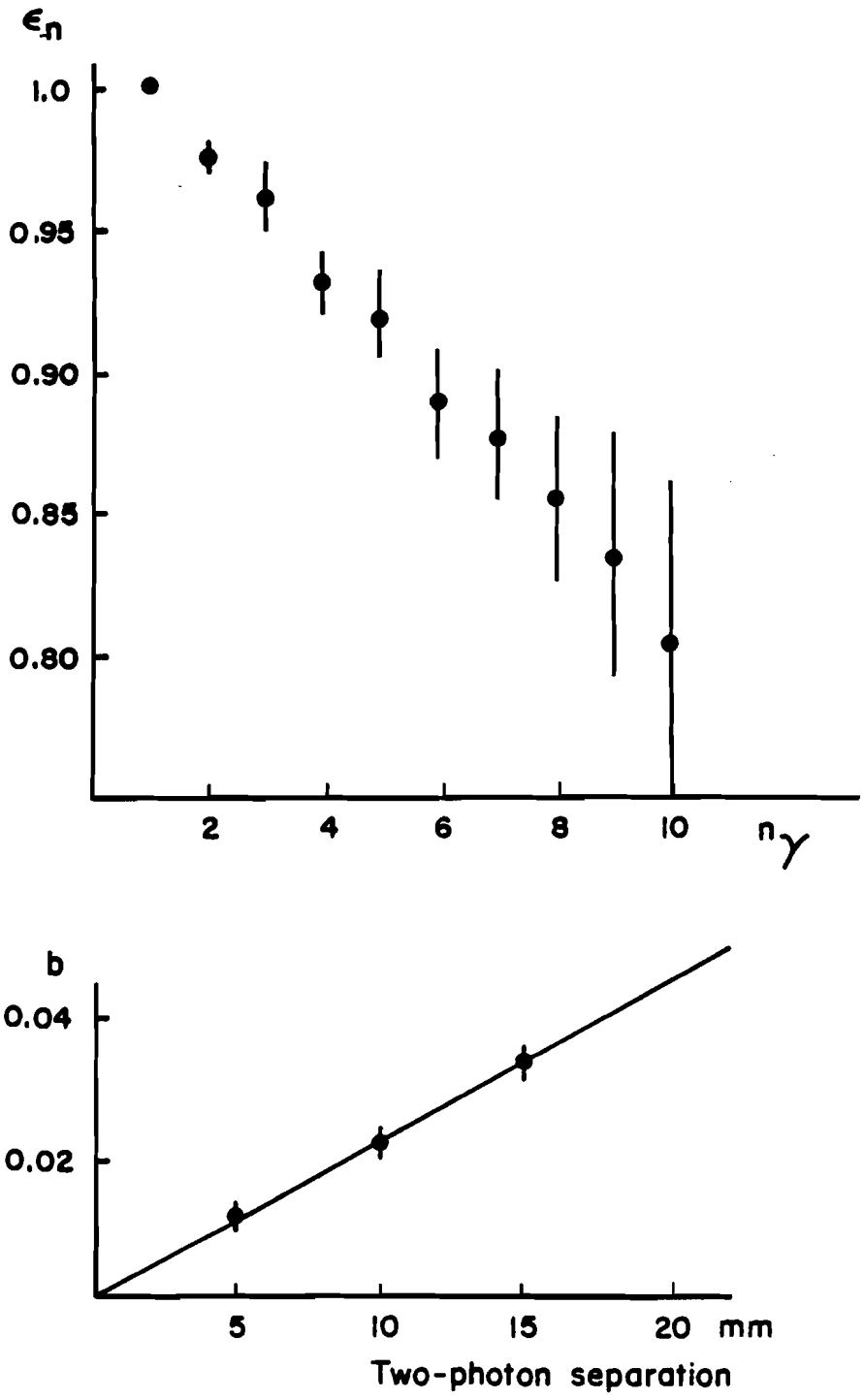
ϵ_n
1.0
0.95
0.90
0.85
0.80
2
4
6
8
10
n_γ
b
0.04
0.02
5
10
15
20 mm
Two-photon separation

Figure 20

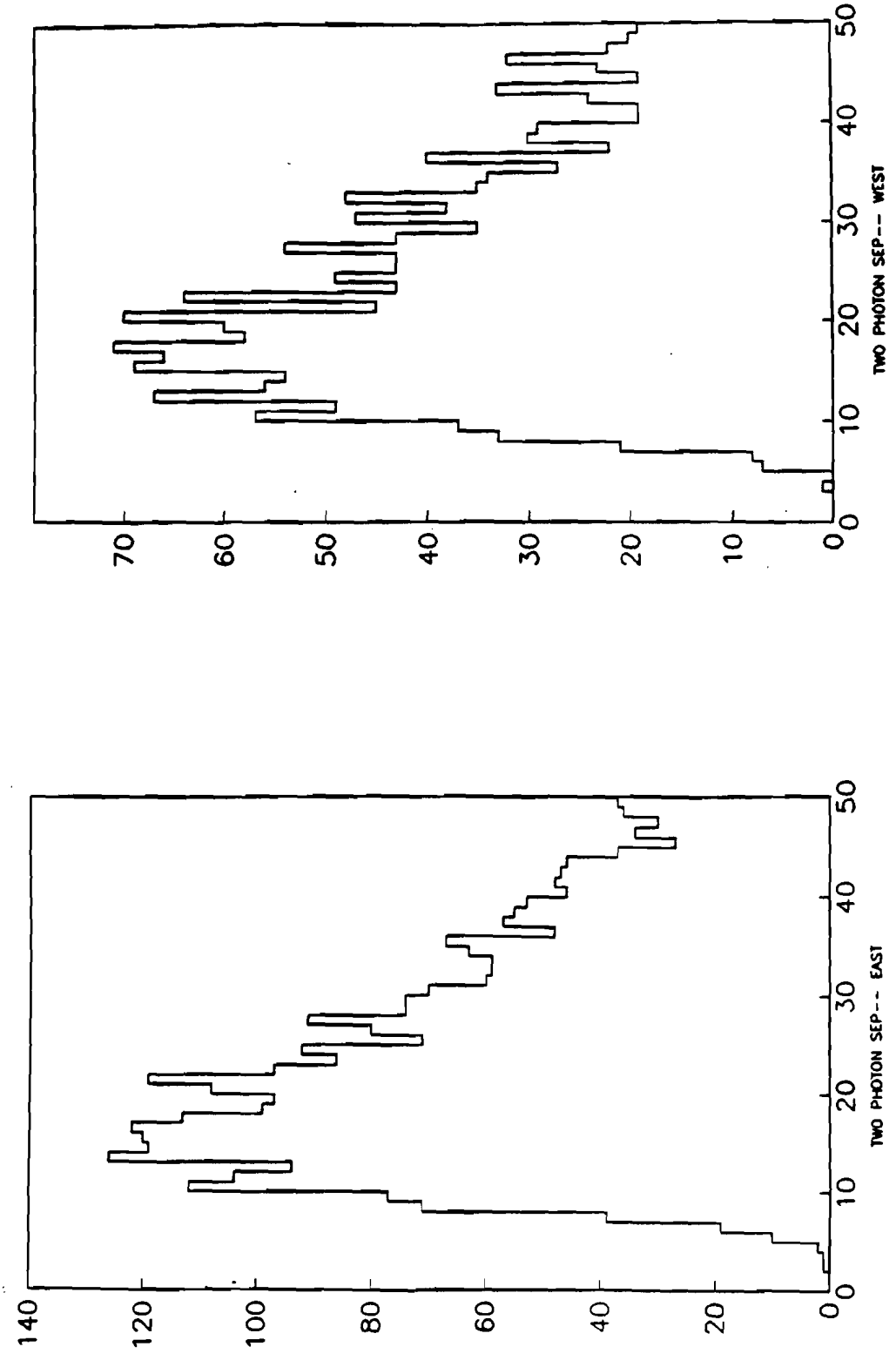

Figure 21

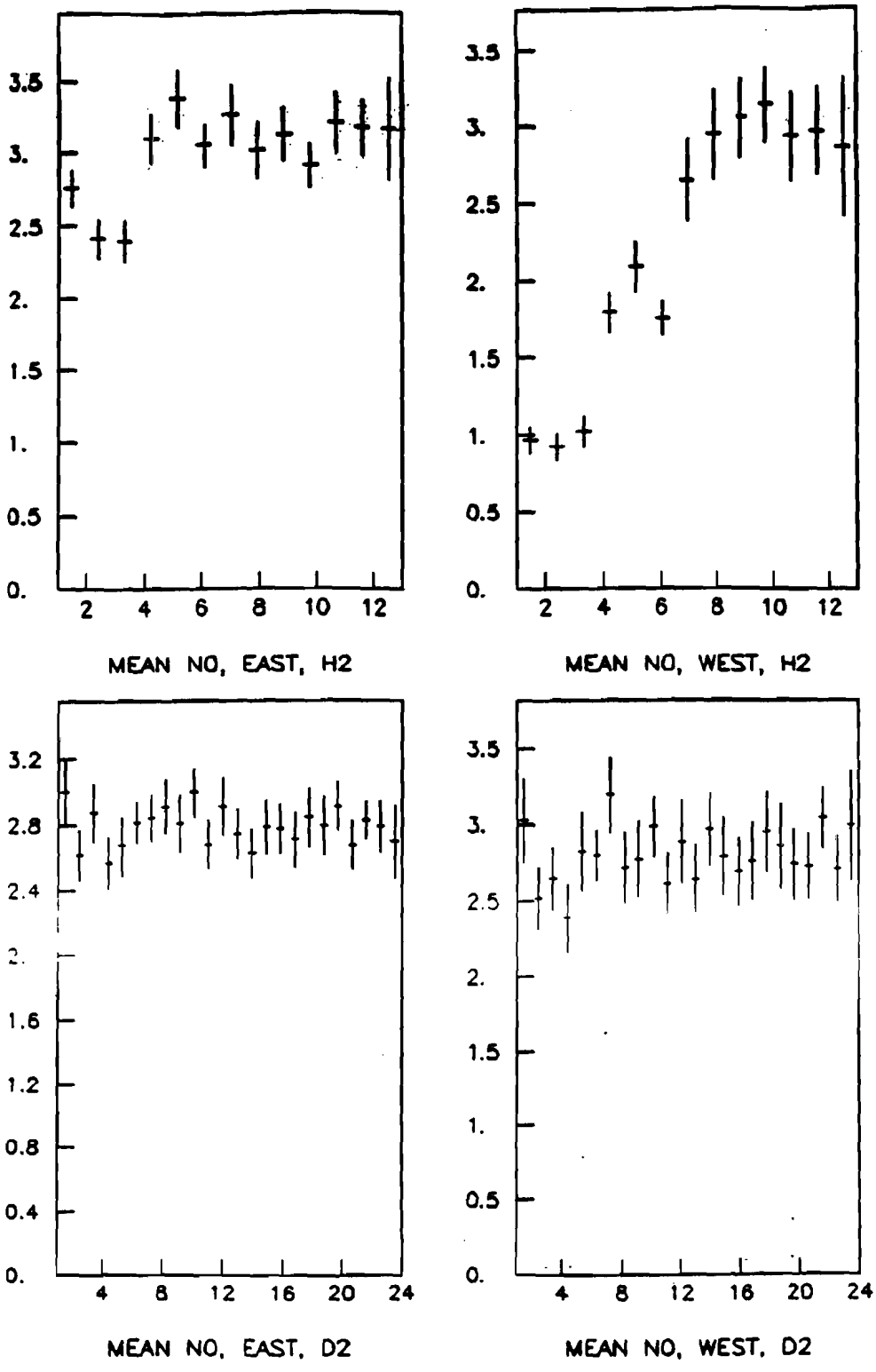

Figure 22

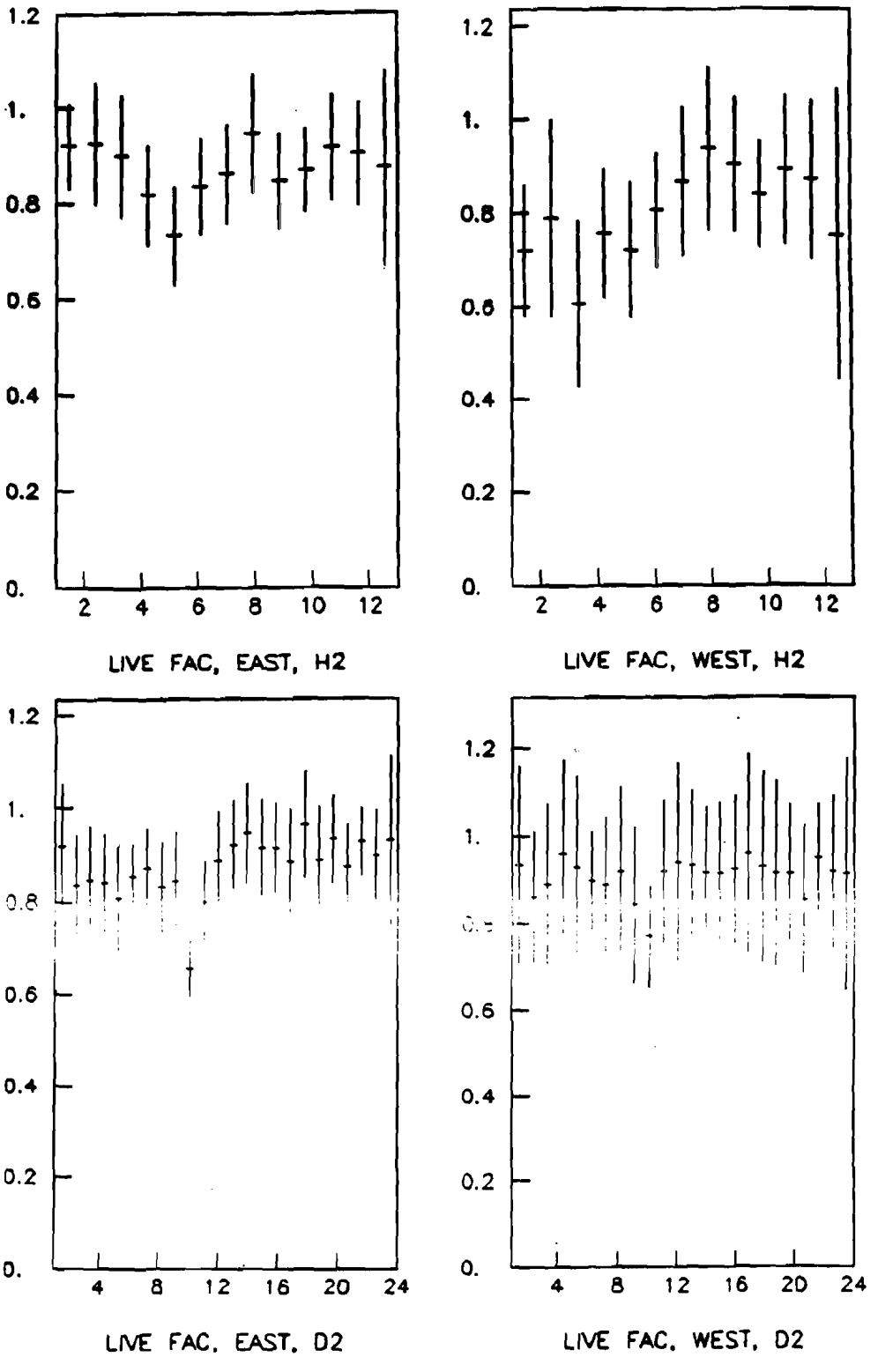
1.2
1.
0.8
0.6
0.4
0.2
0.
2 4 6 8 10 12
LIVE FAC, EAST, H2
LIVE FAC, WEST, H2
4 8 12 16 20 24
LIVE FAC, EAST, D2
LIVE FAC, WEST, D2

Figure 23

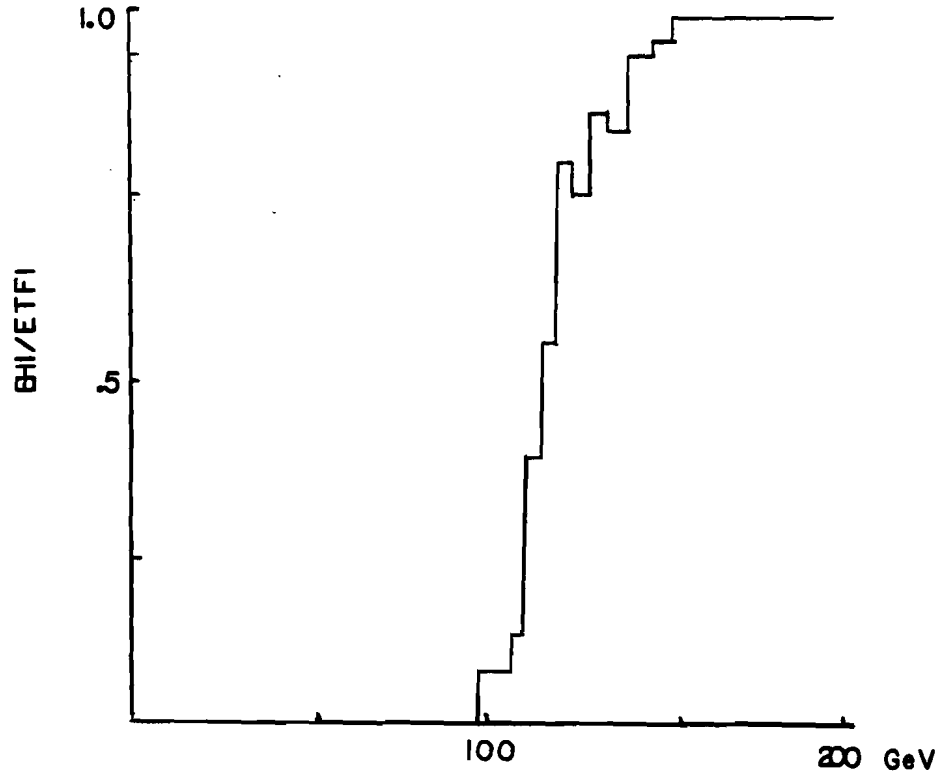

Figure 24

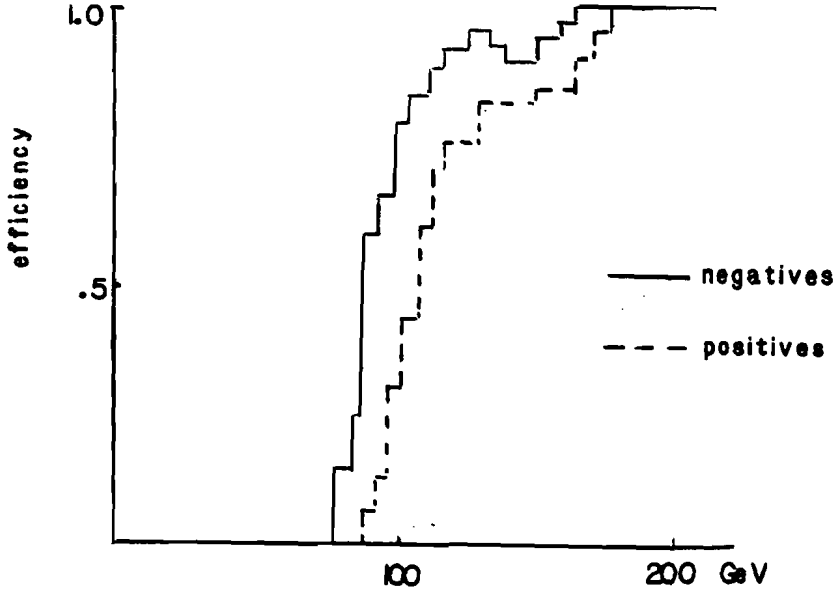

Figure 25

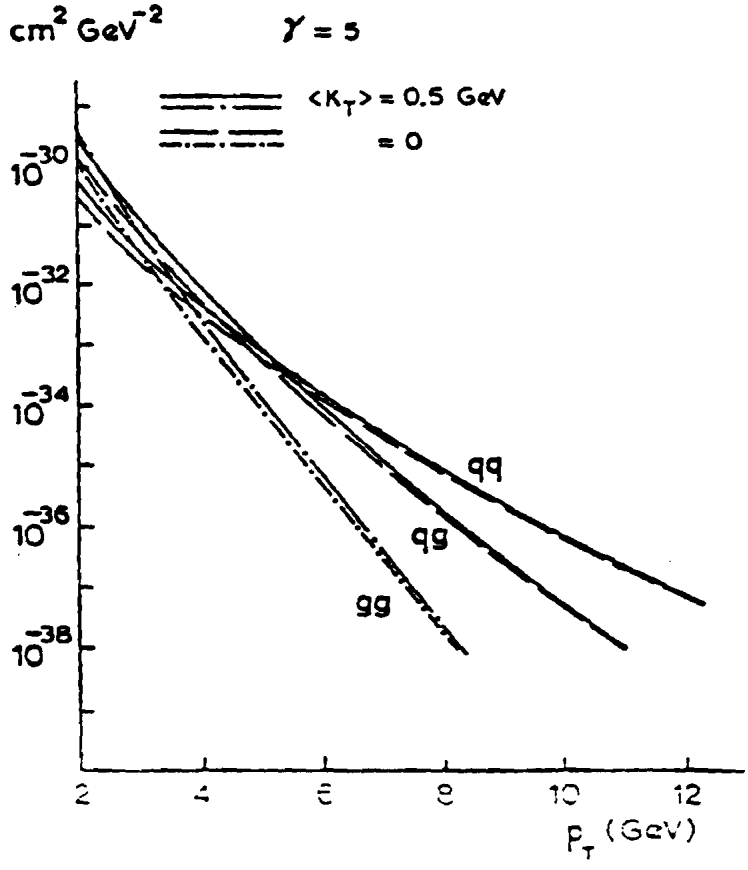
cm² GeV⁻²
γ = 5
<K_T> = 0.5 GeV
= 0
10⁻³⁰
10⁻³²
10⁻³⁴
10⁻³⁶
10⁻³⁸
qq
qg
gg
2
4
6
8
10
12
p_T (GeV)

Figure 26

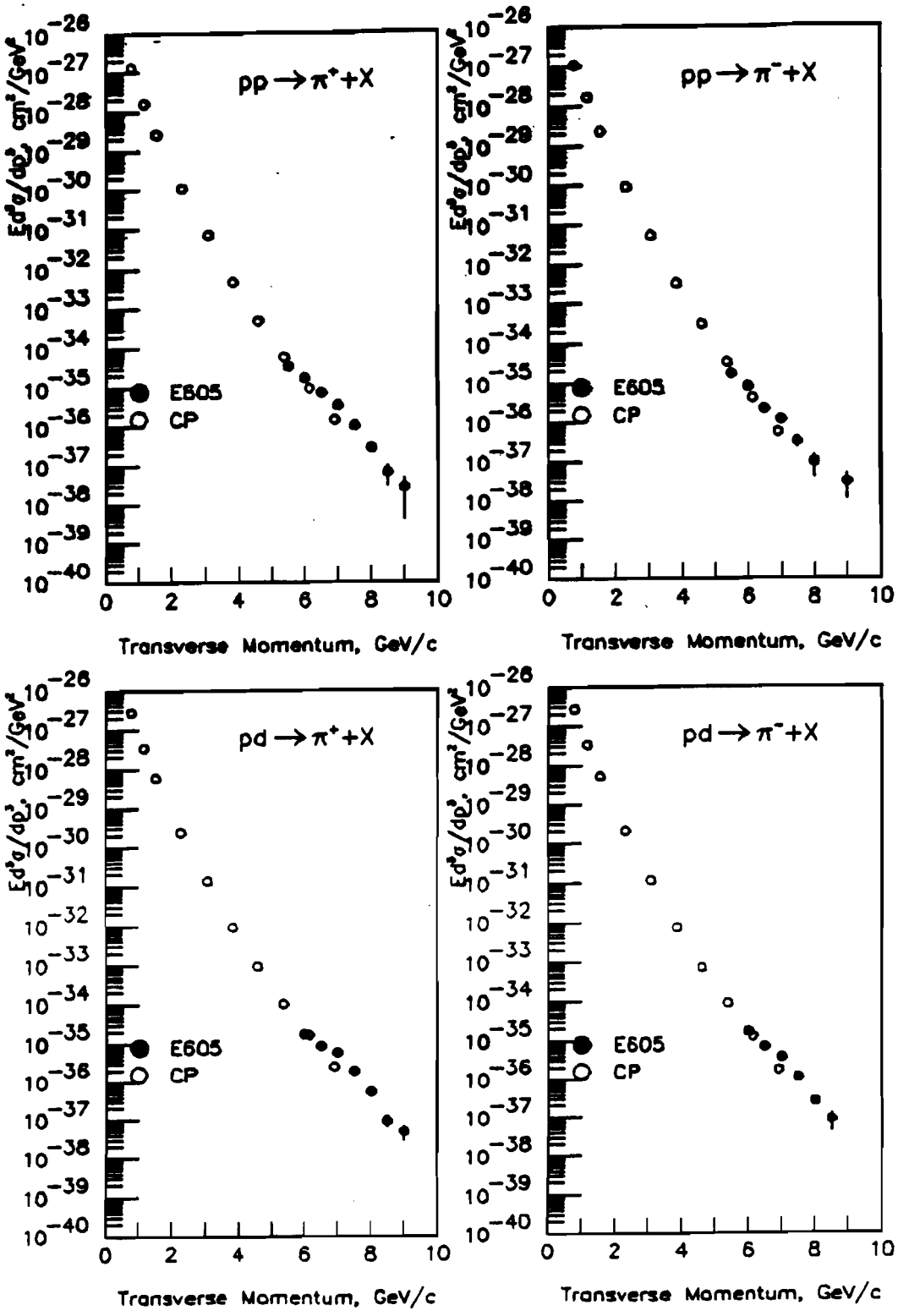

Figure 27

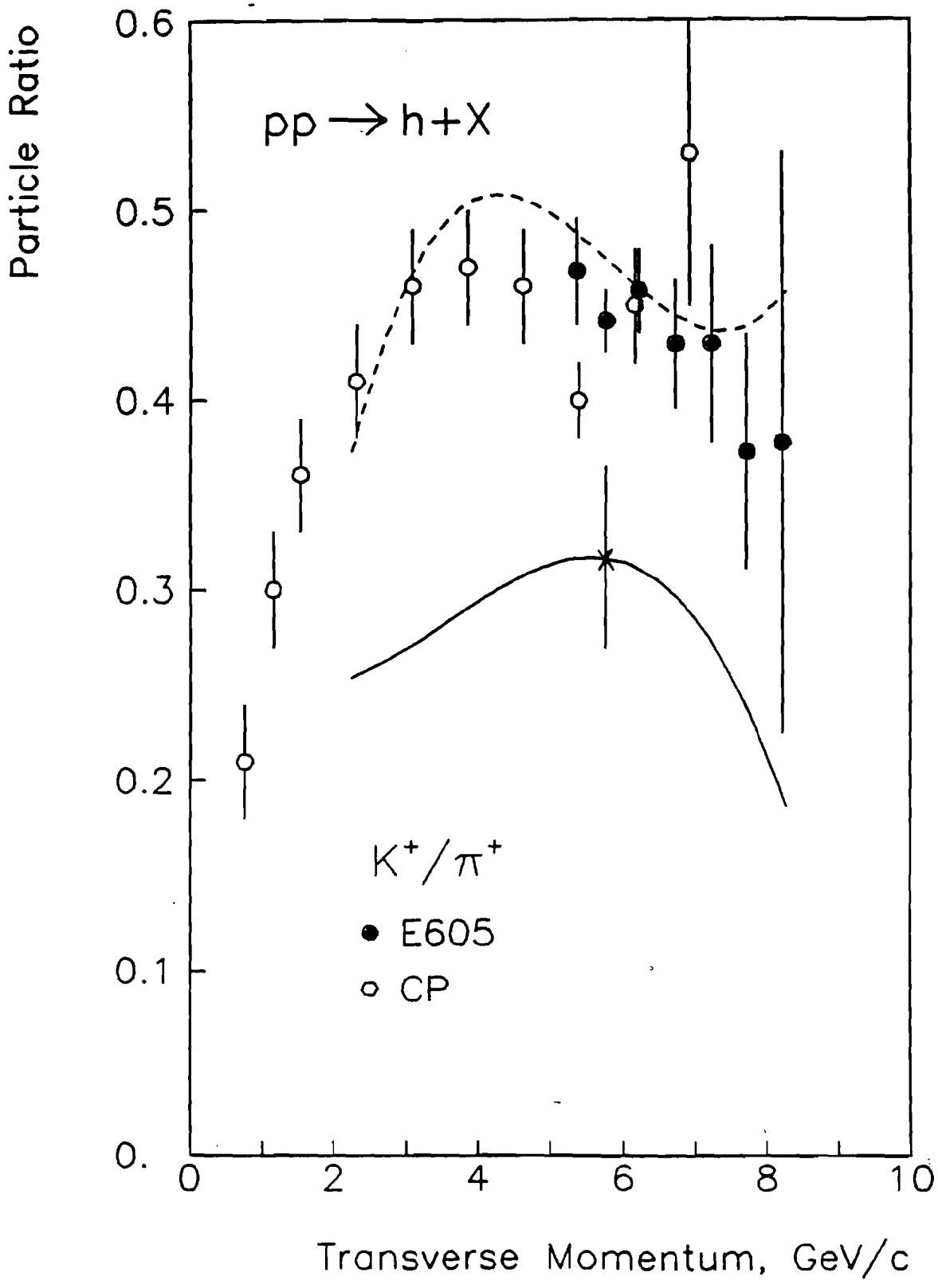
Particle Ratio
0.6
0.5
0.4
0.3
0.2
0.1
0.
pp → h+X
K+/π+
E605
CP
0
2
4
6
8
10
Transverse Momentum, GeV/c

Figure 28

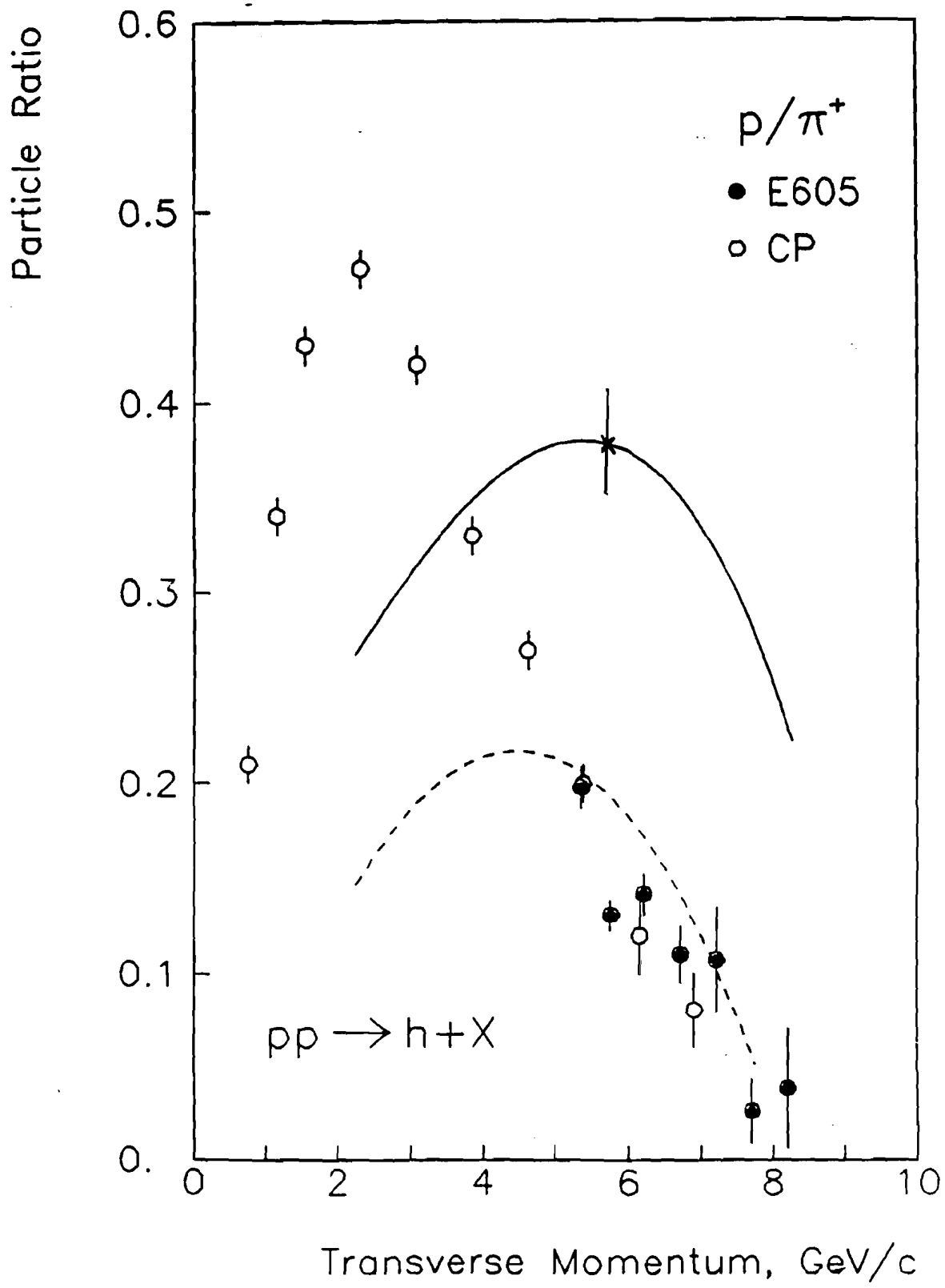
Particle Ratio
0.6
0.5
0.4
0.3
0.2
0.1
0.
0
2
4
6
8
10
Transverse Momentum, GeV/c
p/π+
E605
CP
pp → h+X

Figure 29

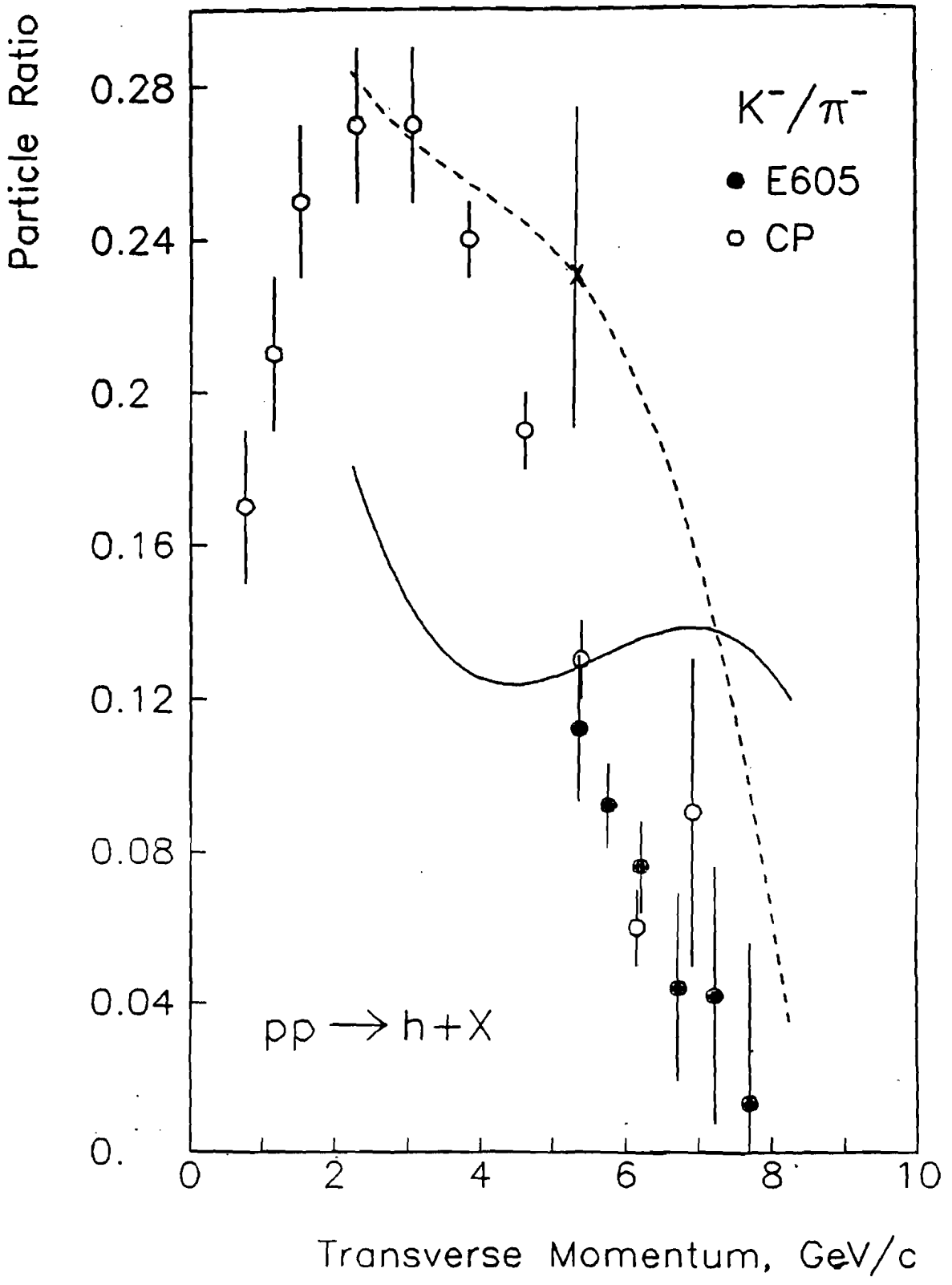
Particle Ratio
0.28
0.24
0.2
0.16
0.12
0.08
0.04
0.
0
2
4
6
8
10
Transverse Momentum, GeV/c
K^-/π^-
E605
CP
$pp \rightarrow h+X$

Figure 30

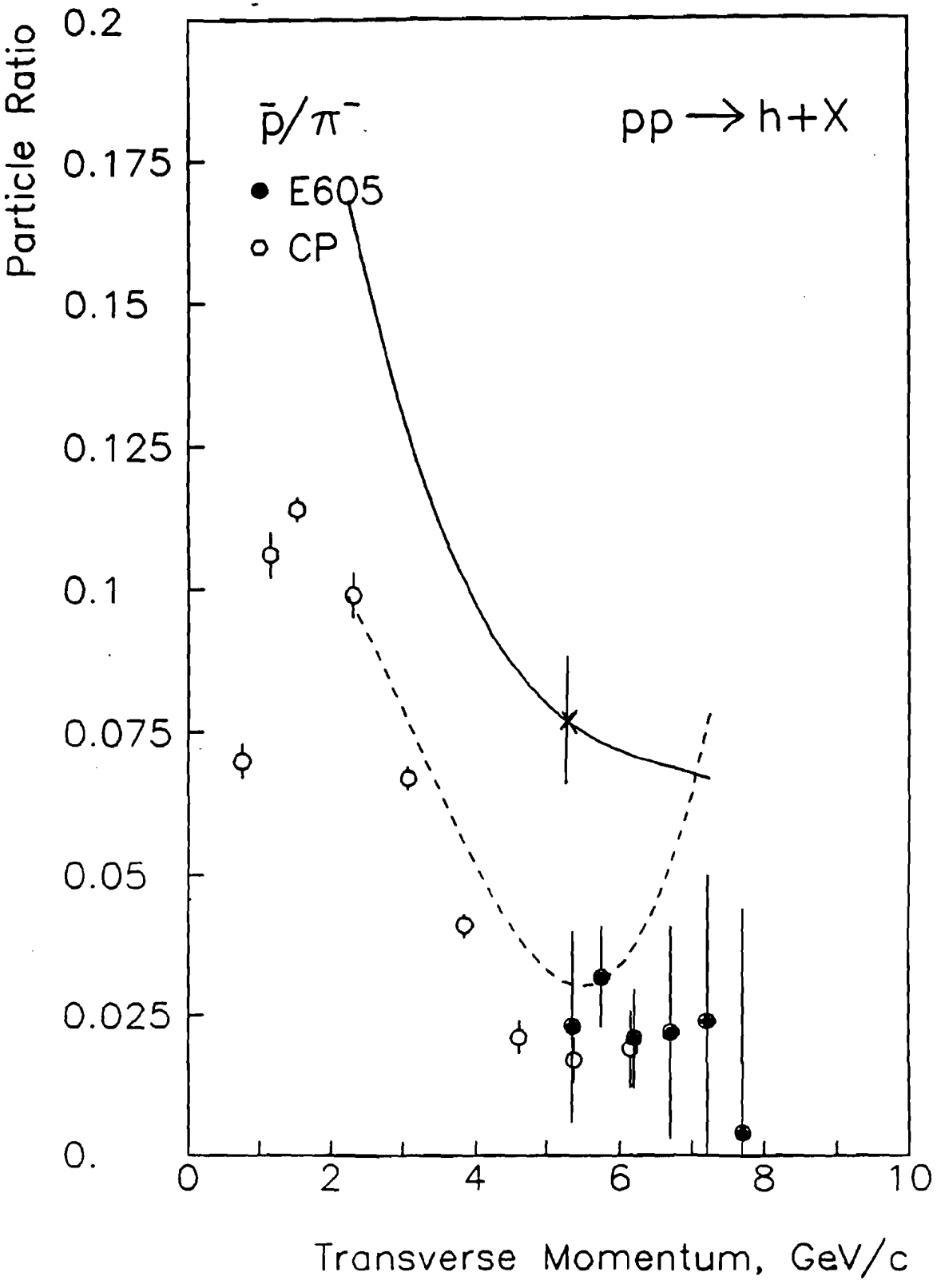
Particle Ratio
0.2
0.175
0.15
0.125
0.1
0.075
0.05
0.025
0.
$\bar{p}/\pi^-$
pp → h+X
E605
CP
0
2
4
6
8
10
Transverse Momentum, GeV/c

Figure 31

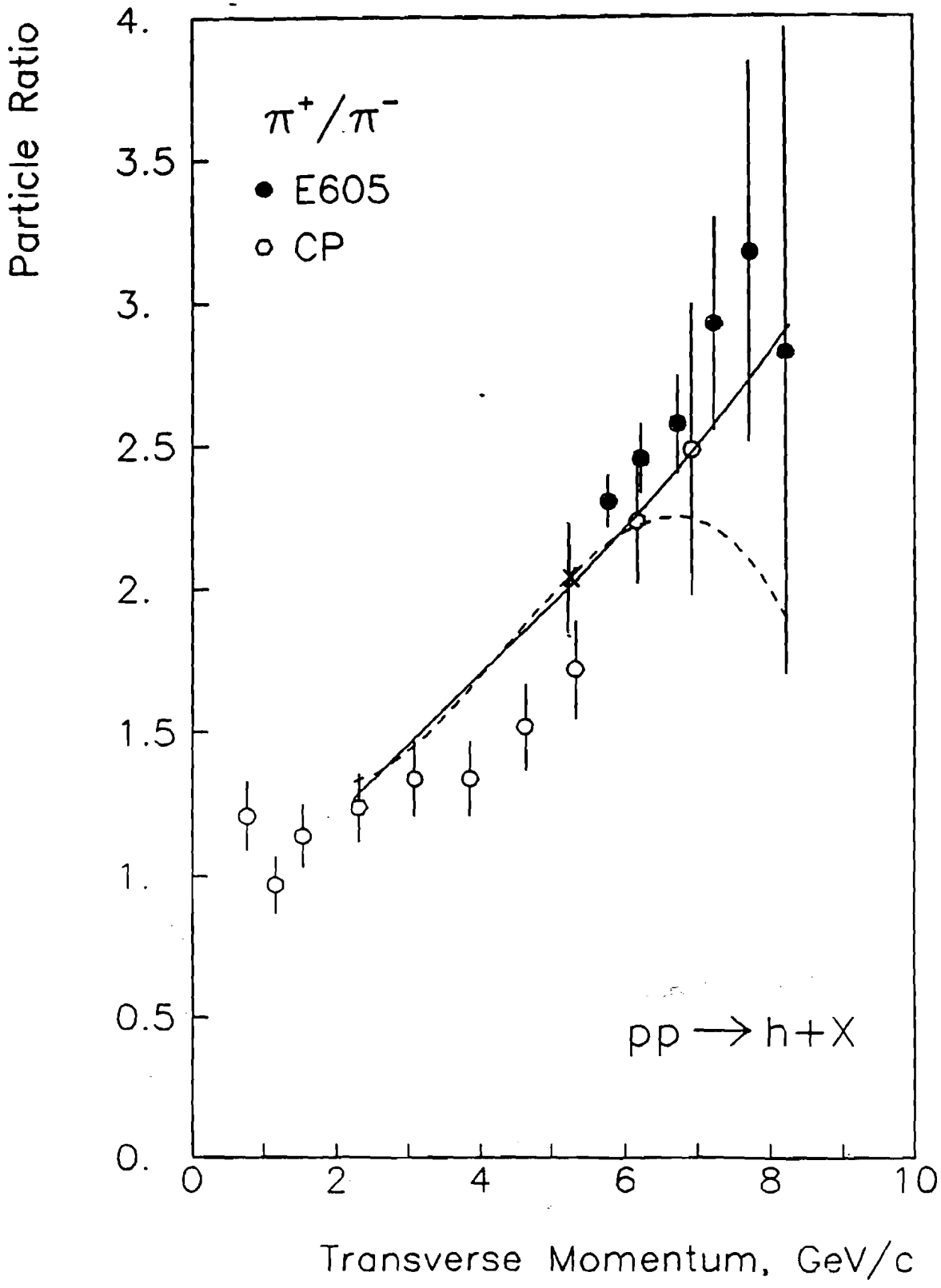
Particle Ratio
4.
3.5
3.
2.5
2.
1.5
1.
0.5
0.
π^+/π^-
E605
CP
$pp \rightarrow h+X$
0
2
4
6
8
10
Transverse Momentum, GeV/c

Figure 32

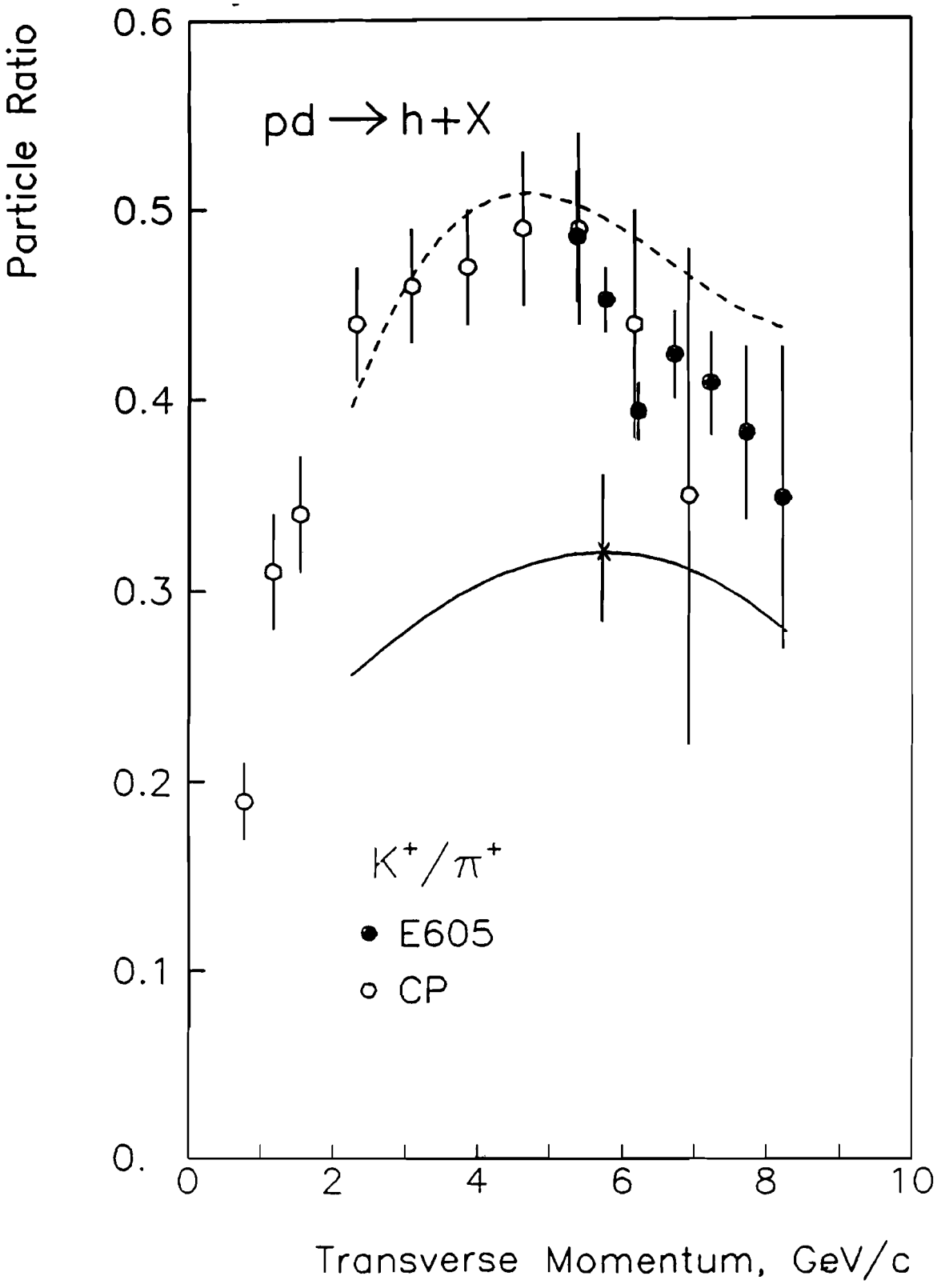
Particle Ratio
0.6
0.5
0.4
0.3
0.2
0.1
0.
pd → h+X
K+/π+
E605
CP
0
2
4
6
8
10
Transverse Momentum, GeV/c

Figure 33

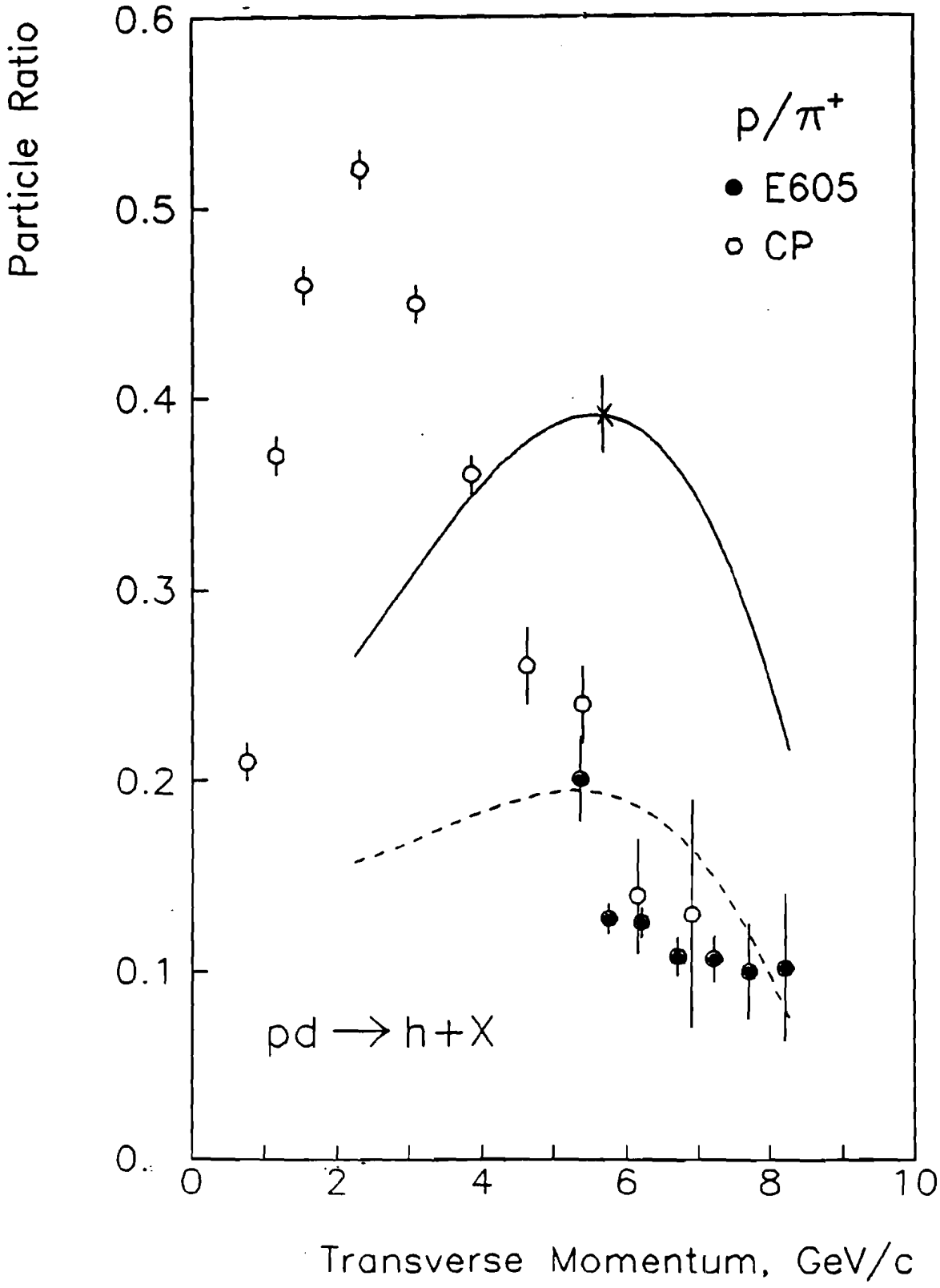
Particle Ratio
0.6
0.5
0.4
0.3
0.2
0.1
0.
0
2
4
6
8
10
Transverse Momentum, GeV/c
p/π+
E605
CP
pd → h+X

Figure 34

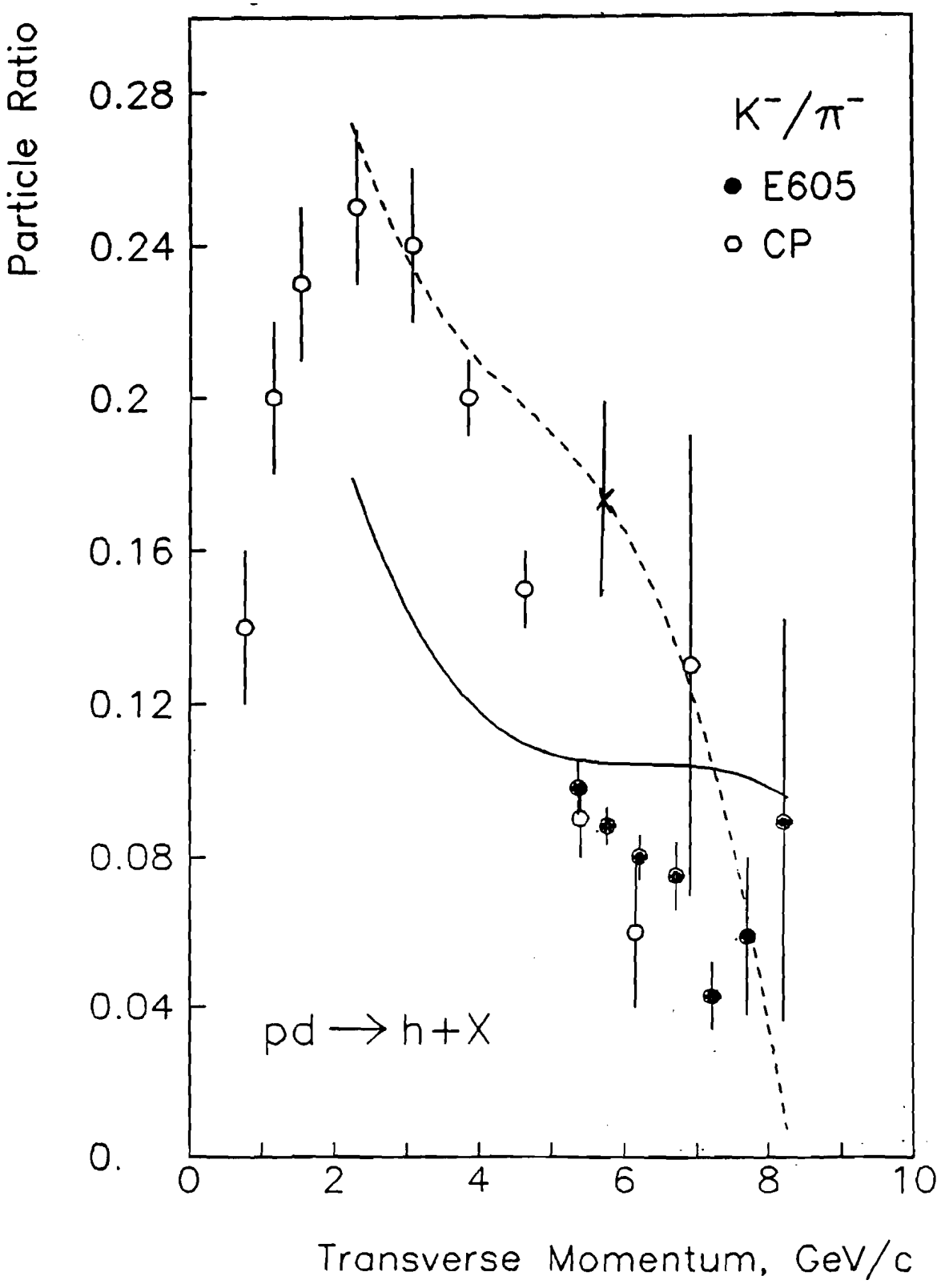
Particle Ratio
0.28
0.24
0.2
0.16
0.12
0.08
0.04
0.
K^-/π^-
E605
CP
$pd \rightarrow h+X$
0
2
4
6
8
10
Transverse Momentum, GeV/c

Figure 35

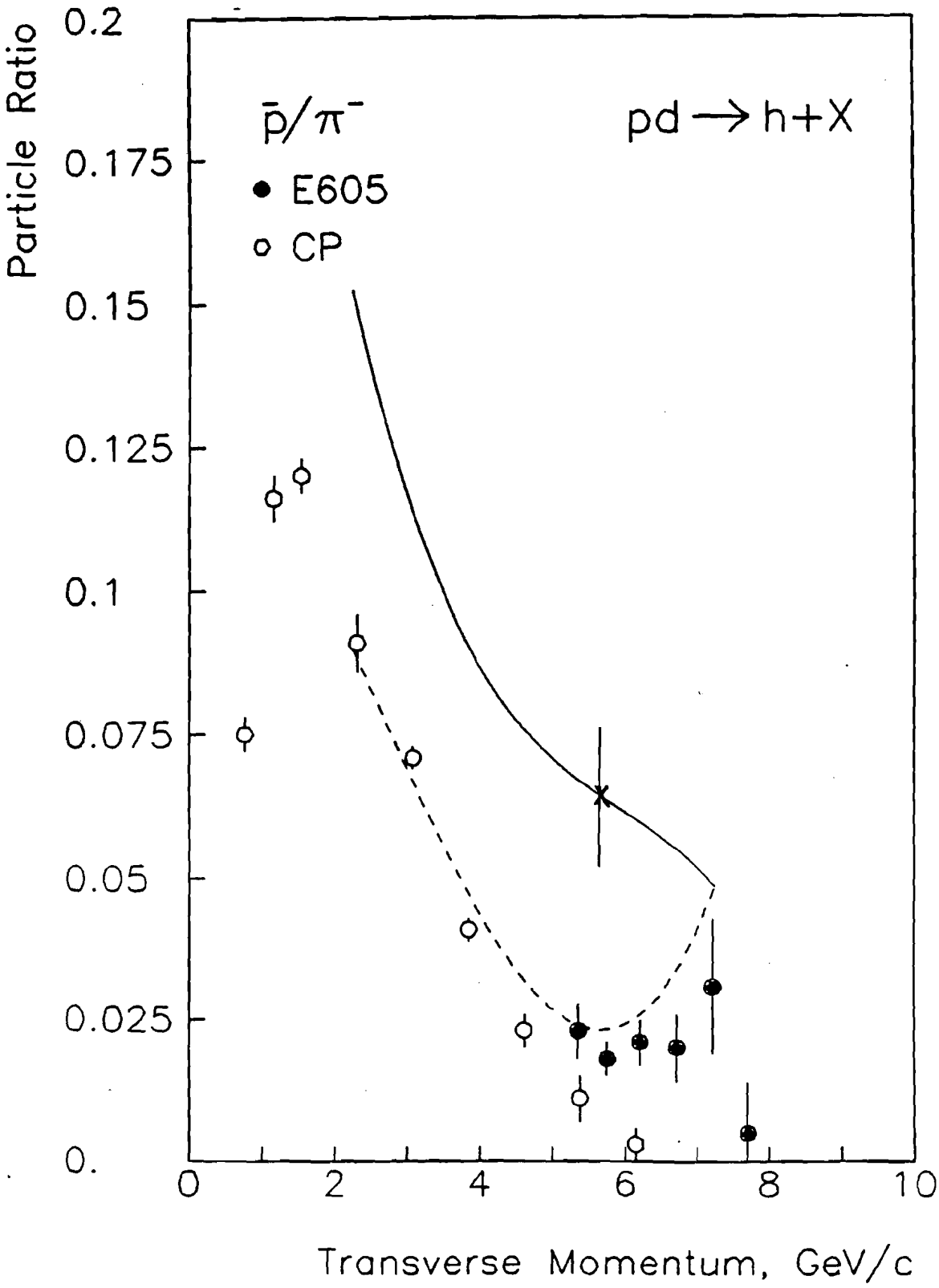
Particle Ratio
0.2
0.175
0.15
0.125
0.1
0.075
0.05
0.025
0.
$\bar{p}/\pi^-$
pd → h+X
E605
CP
0
2
4
6
8
10
Transverse Momentum, GeV/c

Figure 36

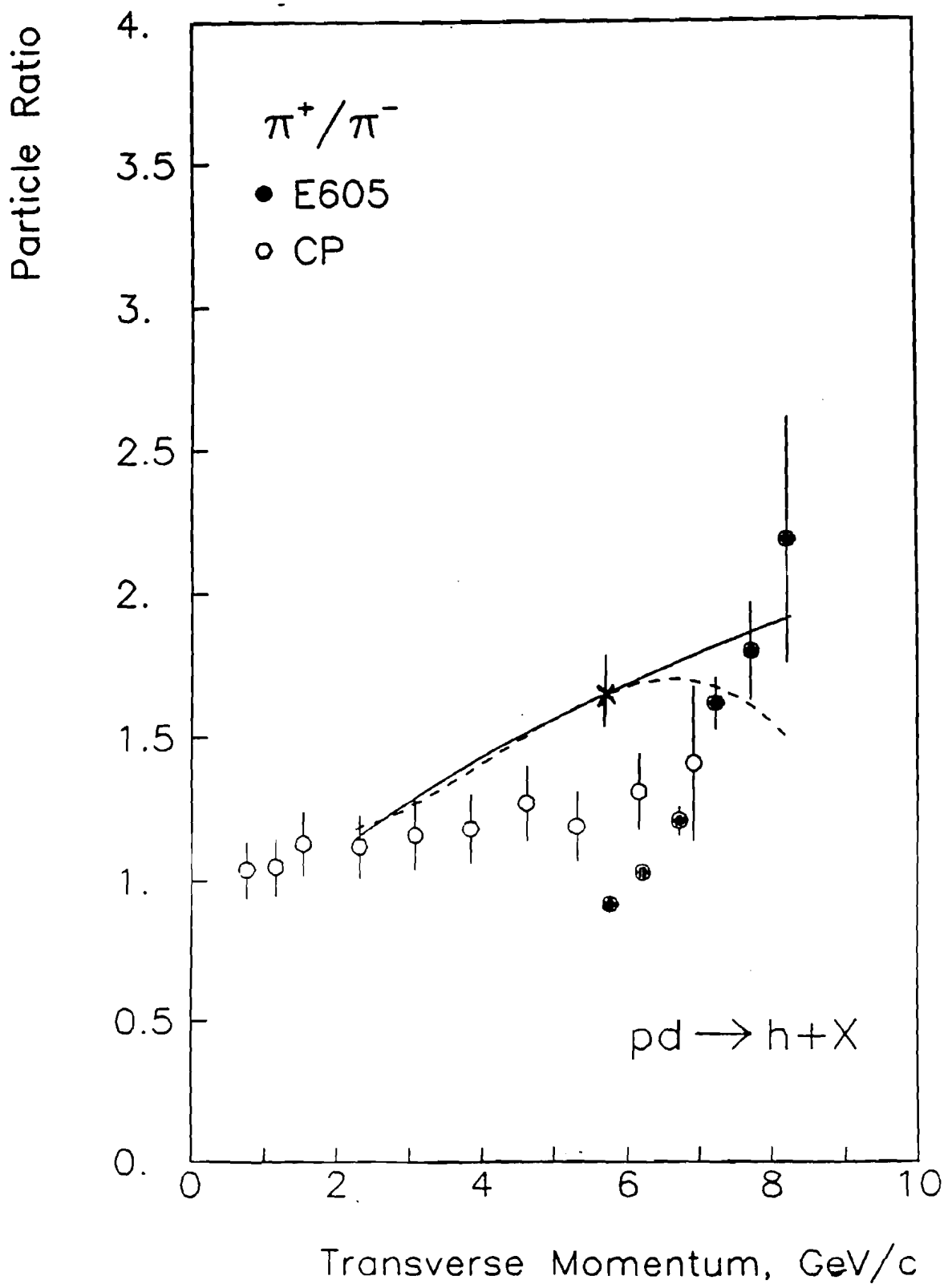
Particle Ratio
4.
3.5
3.
2.5
2.
1.5
1.
0.5
0.
π^+/π^-
E605
CP
$pd \rightarrow h+X$
0
2
4
6
8
10
Transverse Momentum, GeV/c

Figure 37

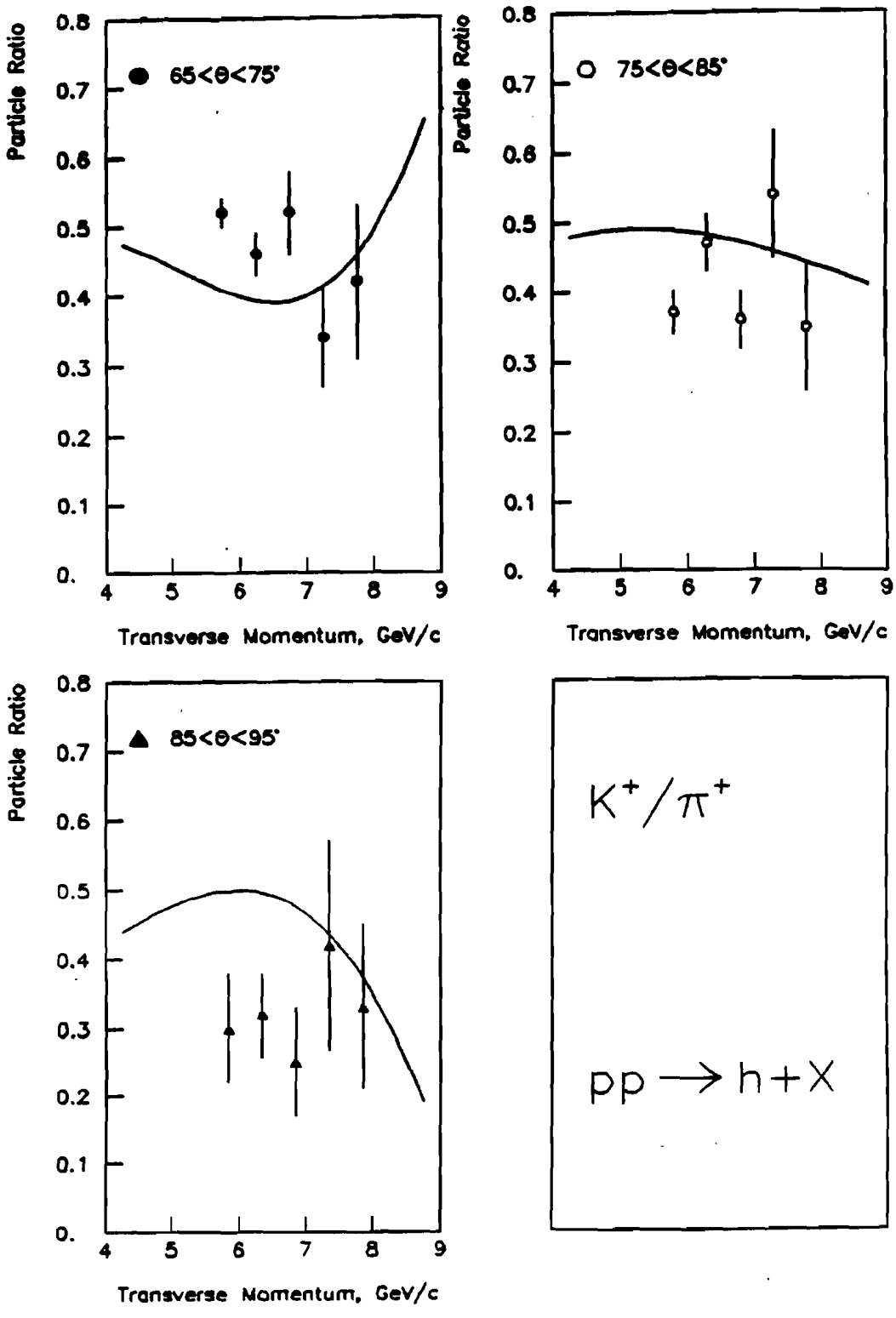
Particle Ratio
65<θ<75°
75<θ<85°
85<θ<95°
Transverse Momentum, GeV/c
K+/π+
pp → h+X

Figure 38

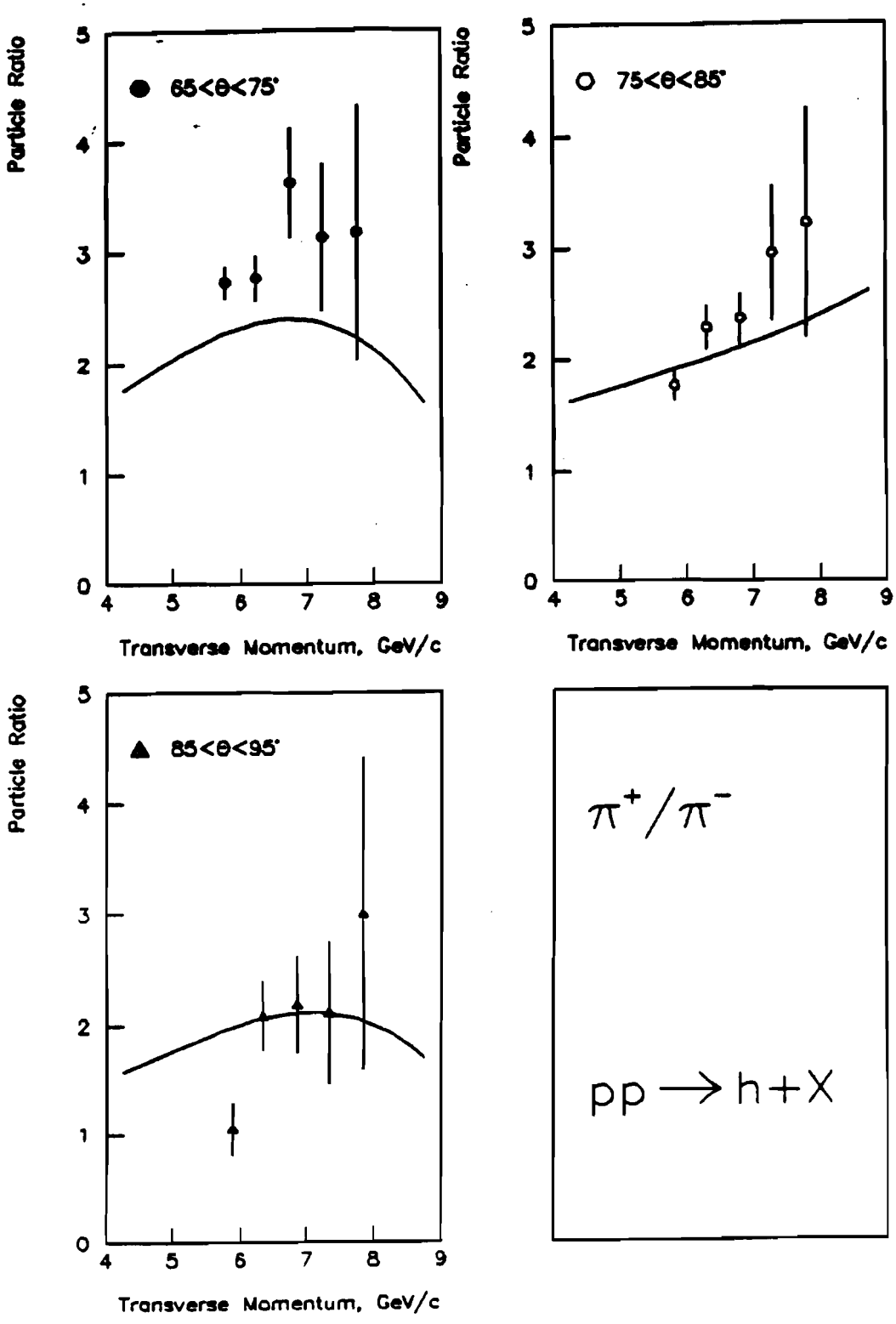
Particle Ratio
65<θ<75°
Transverse Momentum, GeV/c
75<θ<85°
85<θ<95°
π^+/π^-
$pp \rightarrow h+X$

Figure 39

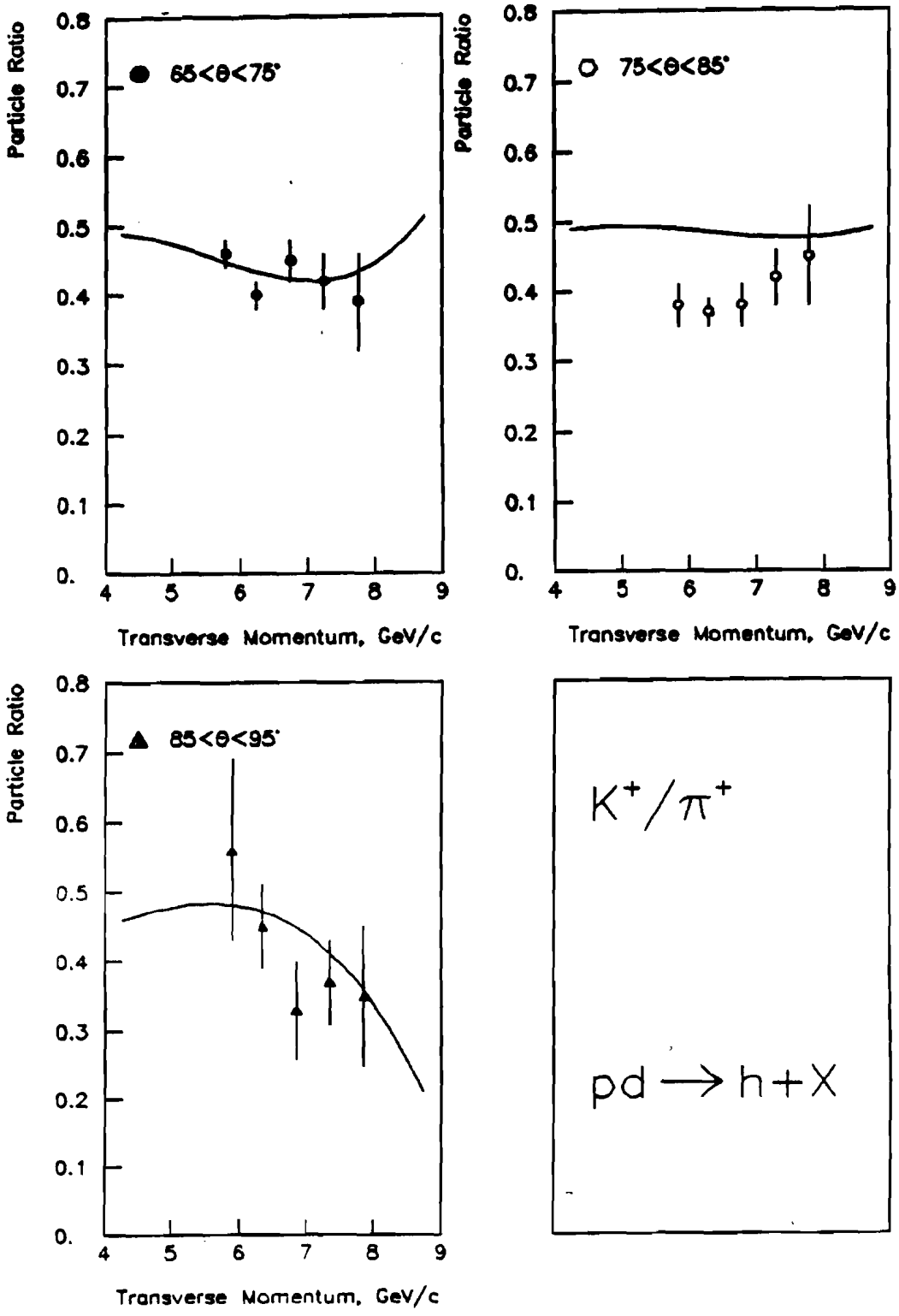
Particle Ratio
65<θ<75°
75<θ<85°
85<θ<95°
Transverse Momentum, GeV/c
K^+/π^+
$pd \rightarrow h+X$

Figure 40

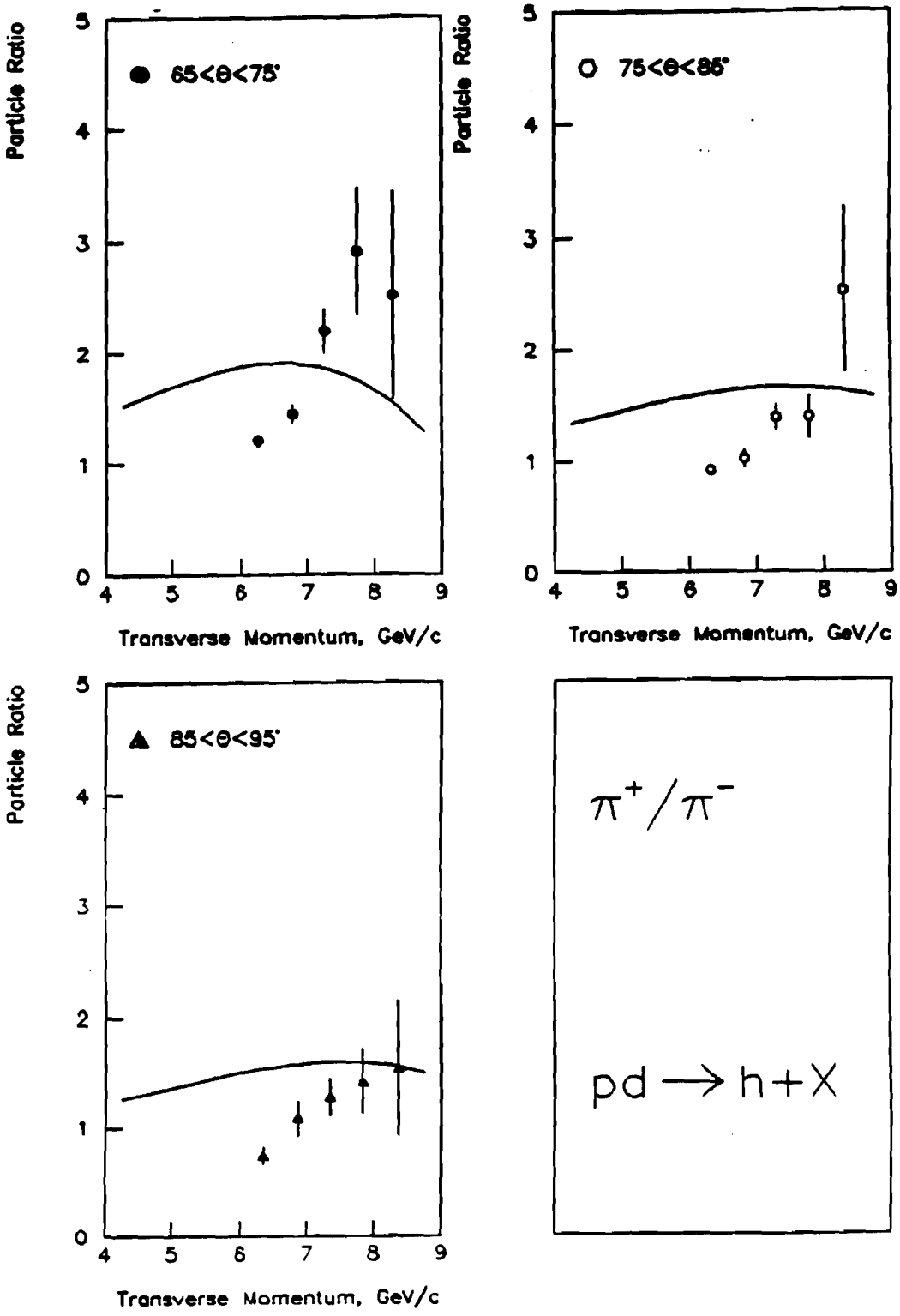
Particle Ratio
65<θ<75°
Transverse Momentum, GeV/c
75<θ<85°
85<θ<95°
π^+/π^-
pd → h+X

Figure 41

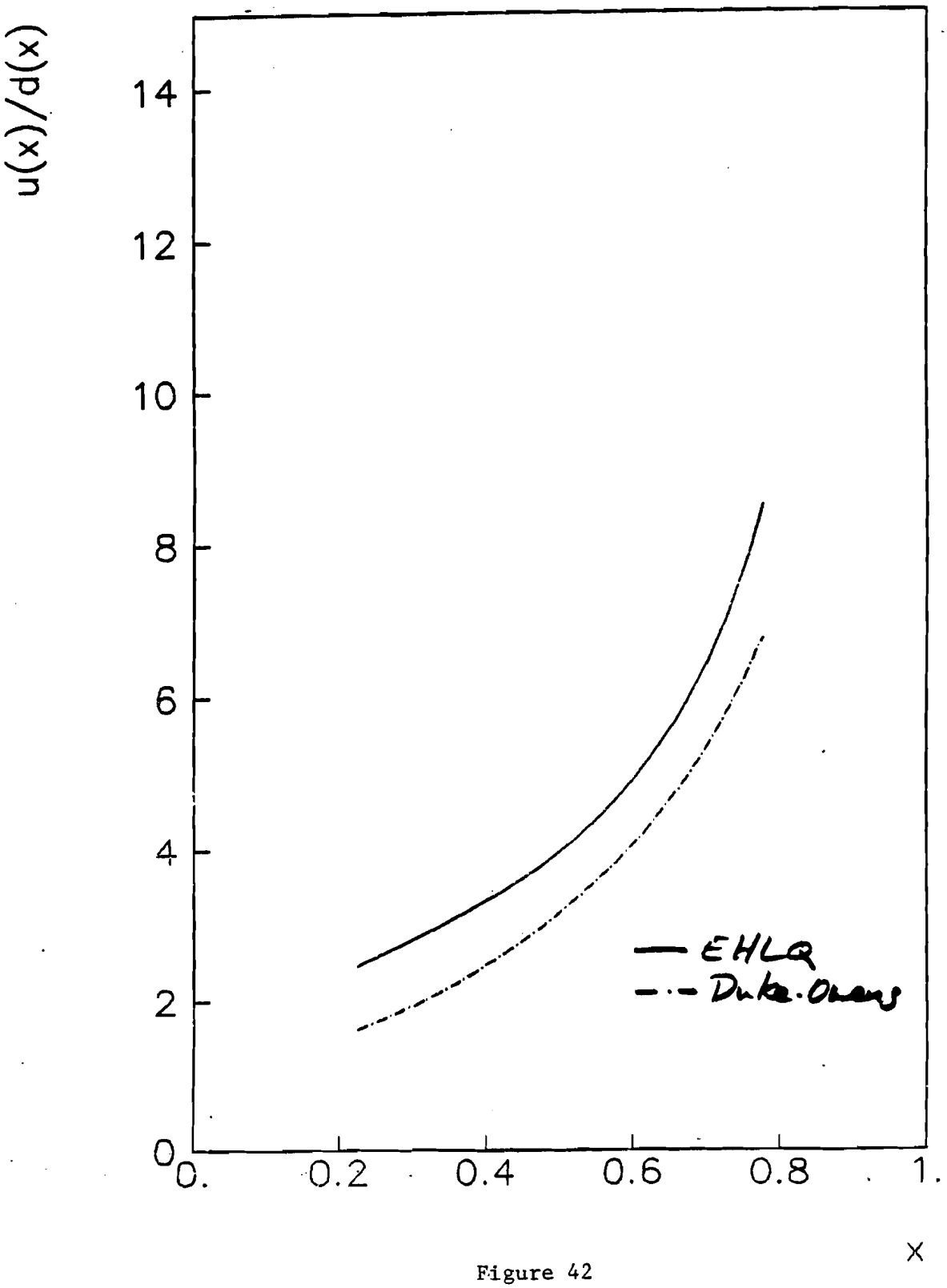

Figure 42

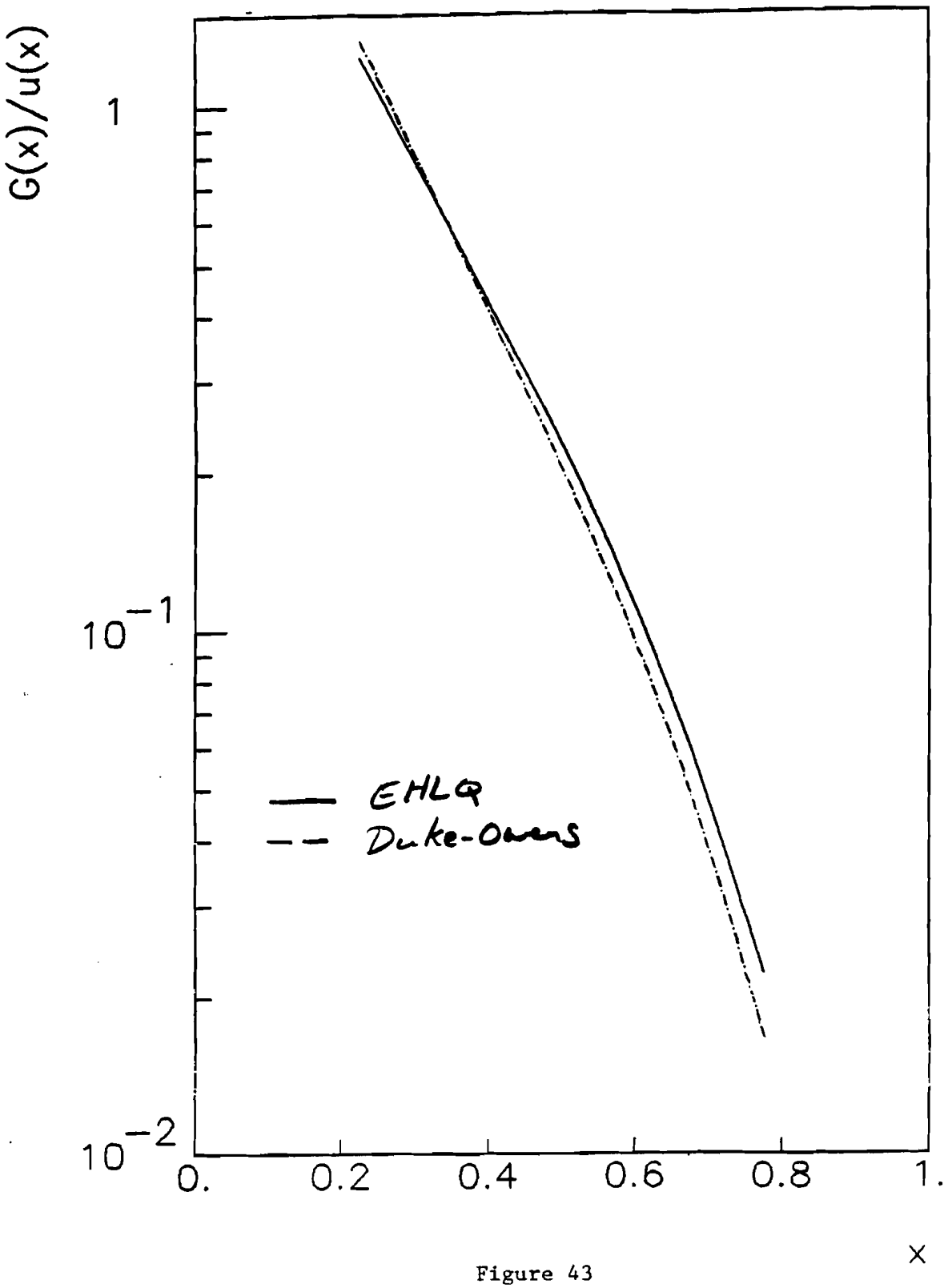

Figure 43

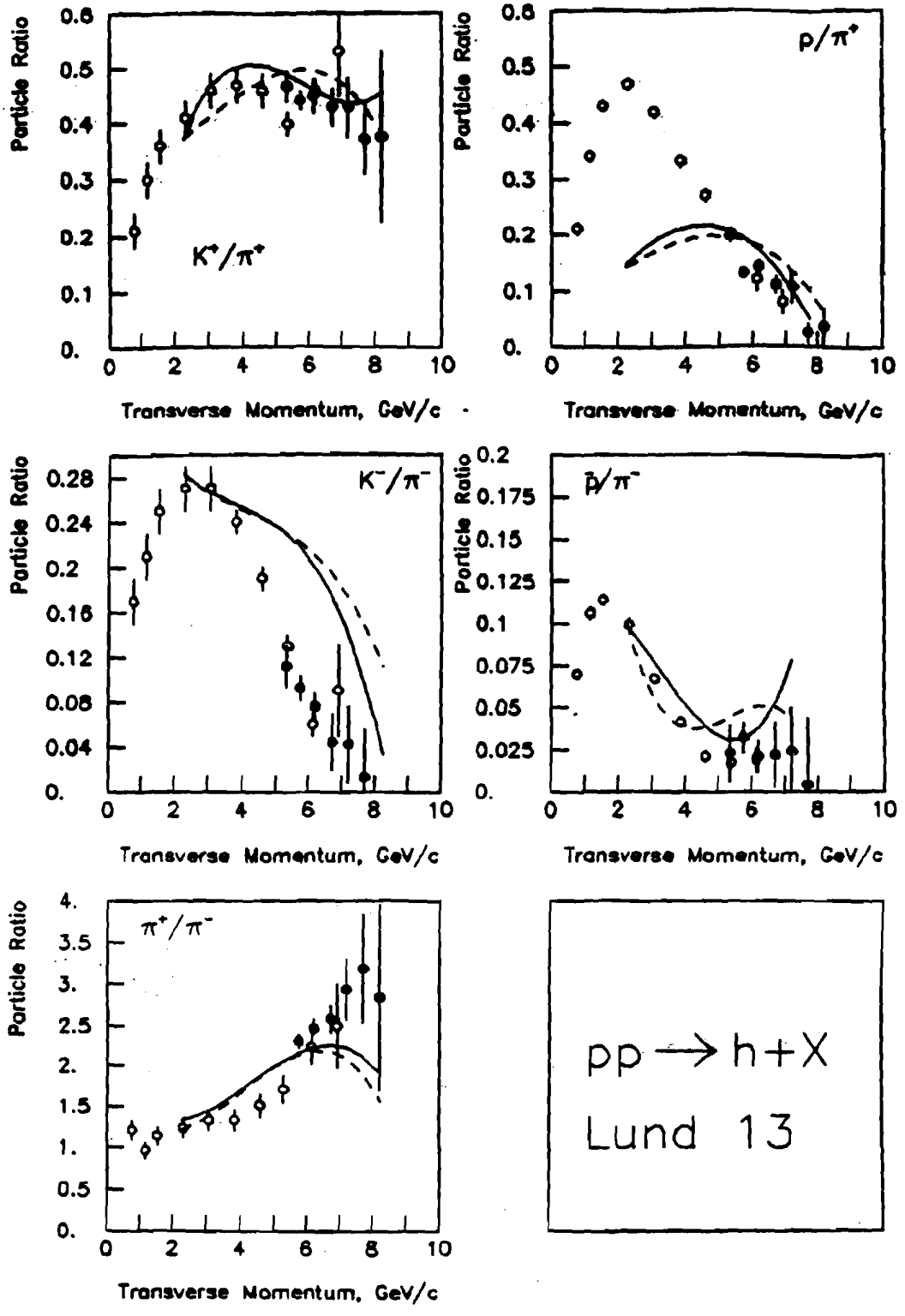
Particle Ratio
K^+/π^+
Transverse Momentum, GeV/c
p/π^+
Transverse Momentum, GeV/c
K^-/π^-
Transverse Momentum, GeV/c
$\bar{p}/\pi^-$
Transverse Momentum, GeV/c
π^+/π^-
Transverse Momentum, GeV/c
pp → h+X
Lund 13

Figure 44a

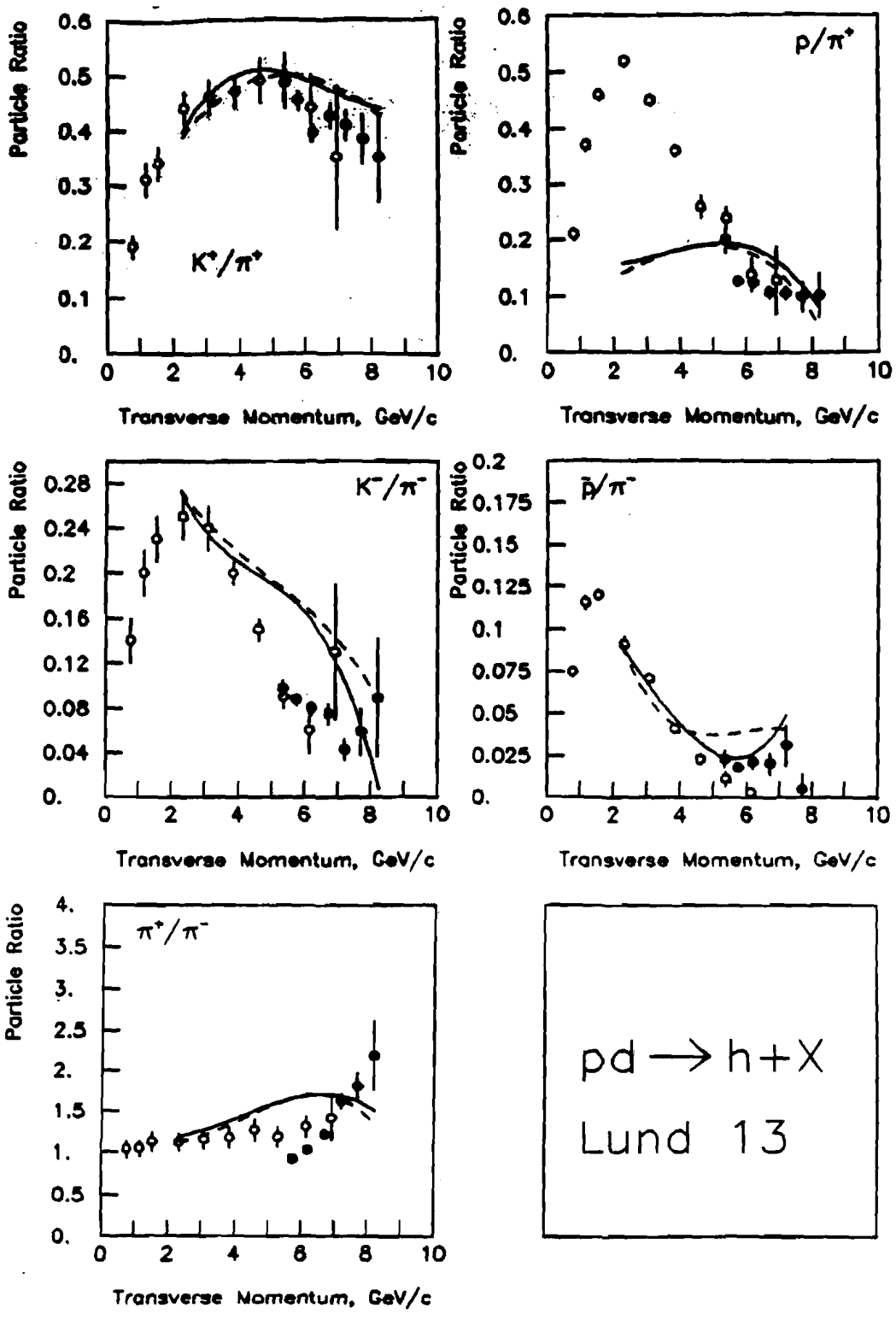
Particle Ratio
K^+/π^+
p/π^+
K^-/π^-
$\bar{p}/\pi^-$
π^+/π^-
Transverse Momentum, GeV/c
pd → h+X
Lund 13

Figure 44b

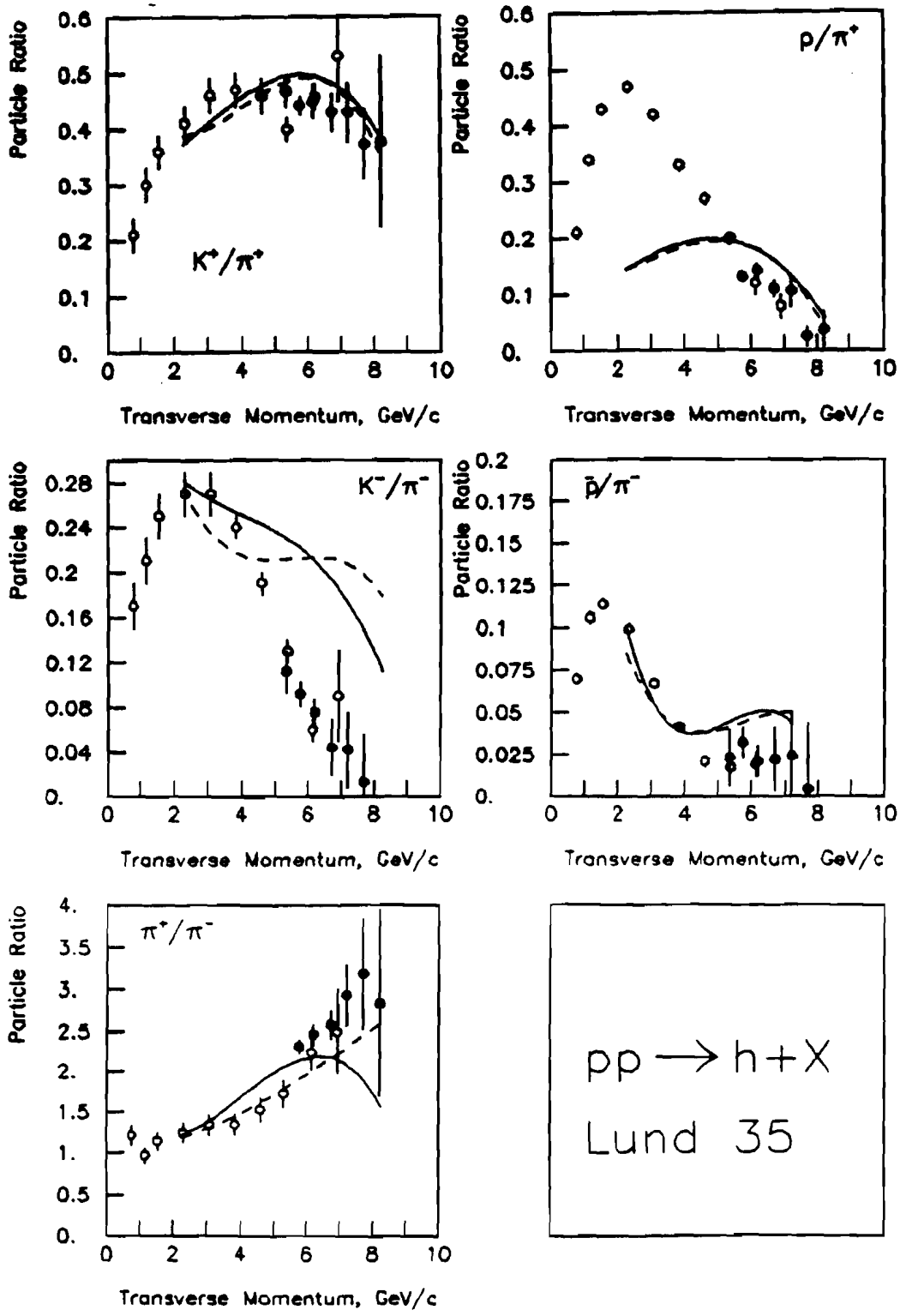
Particle Ratio
K^+/π^+
p/π^+
K^-/π^-
$\bar{p}/\pi^-$
π^+/π^-
Transverse Momentum, GeV/c
pp → h+X
Lund 35

Figure 45a

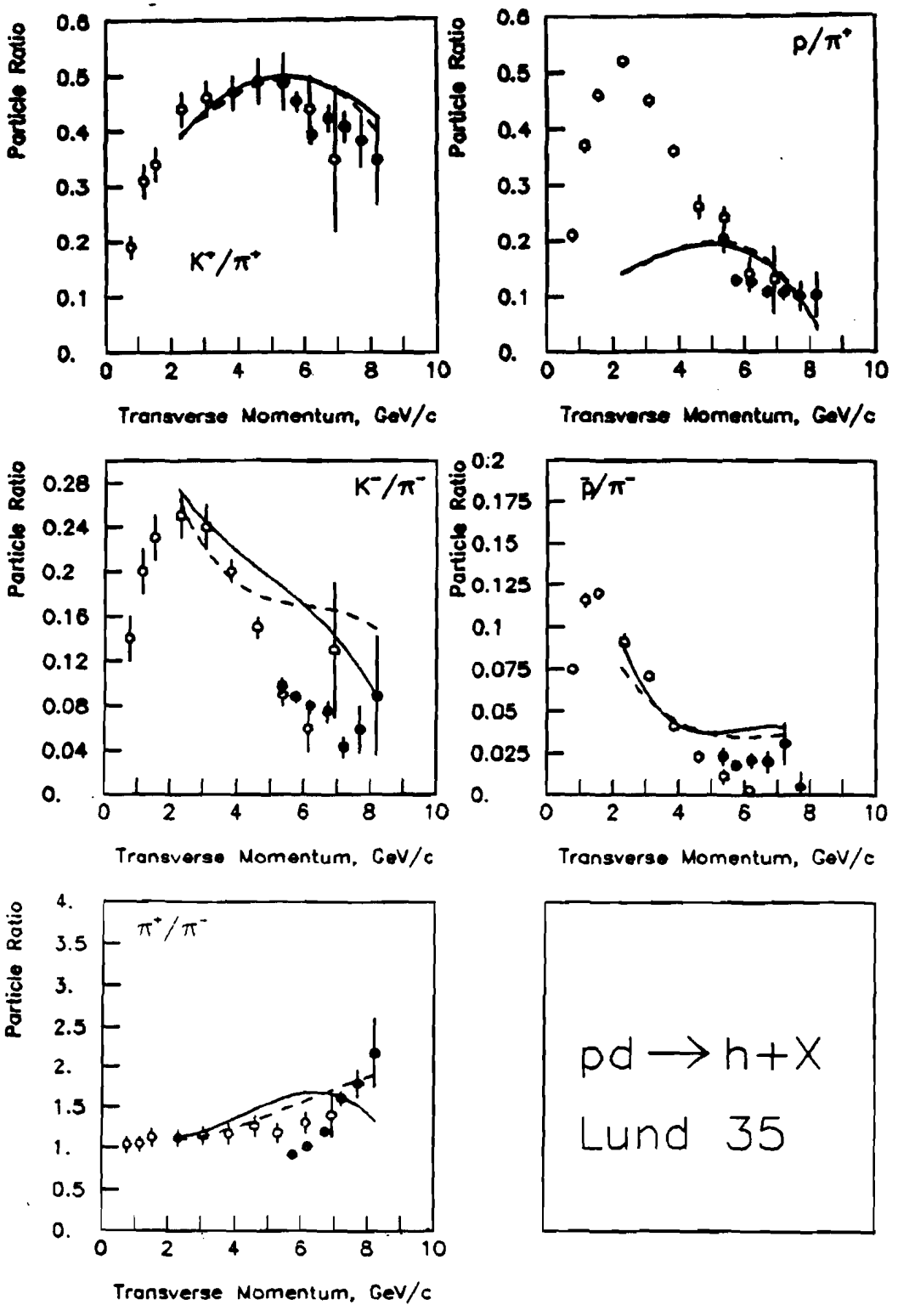
Particle Ratio
K^+/π^+
Transverse Momentum, GeV/c
p/π^+
Transverse Momentum, GeV/c
K^-/π^-
Transverse Momentum, GeV/c
$\bar{p}/\pi^-$
Transverse Momentum, GeV/c
π^+/π^-
Transverse Momentum, GeV/c
pd → h+X
Lund 35

Figure 45b

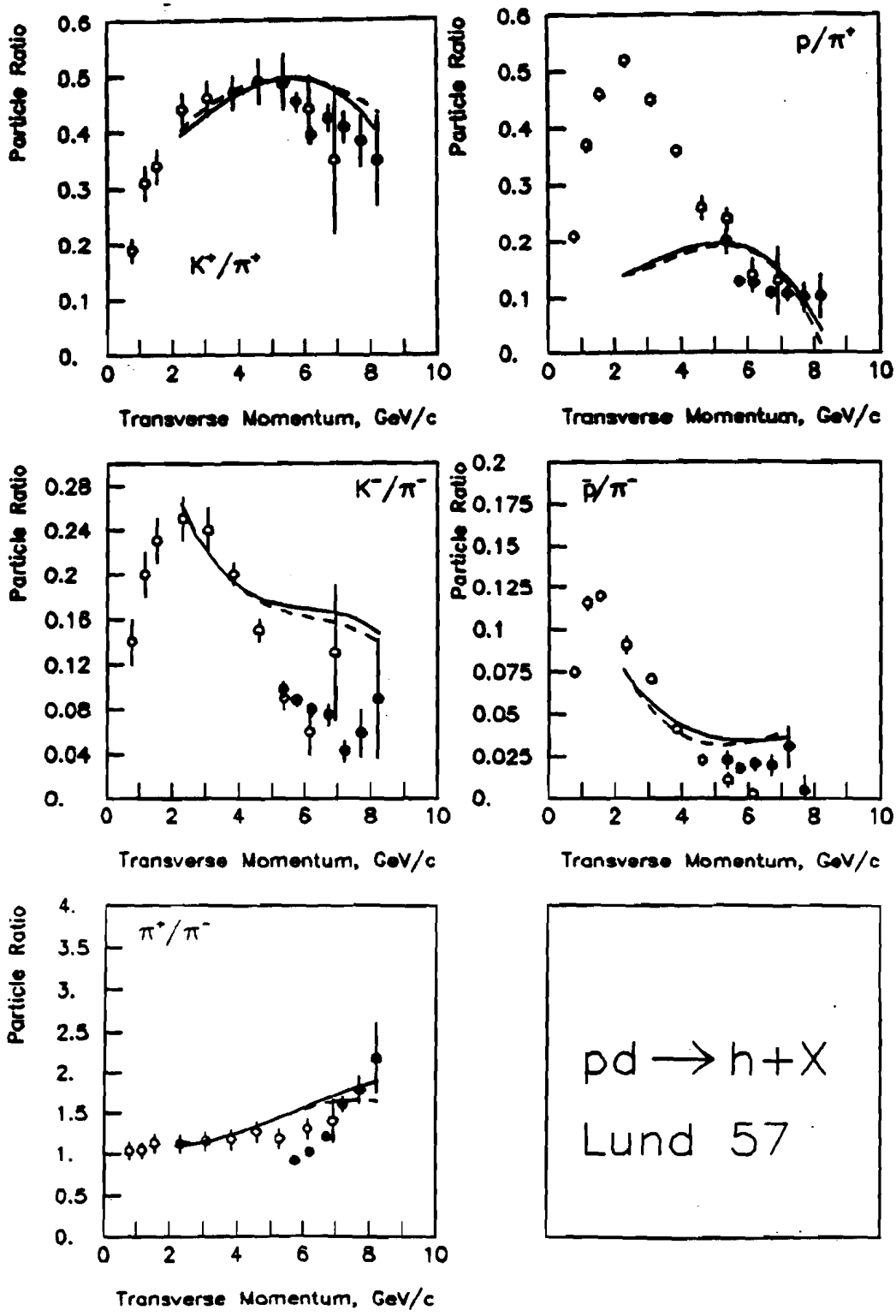
Particle Ratio
K^+/π^+
Transverse Momentum, GeV/c
p/π^+
Transverse Momentum, GeV/c
K^-/π^-
Transverse Momentum, GeV/c
$\bar{p}/\pi^-$
Transverse Momentum, GeV/c
π^+/π^-
Transverse Momentum, GeV/c
pd → h+X
Lund 57

Figure 46a

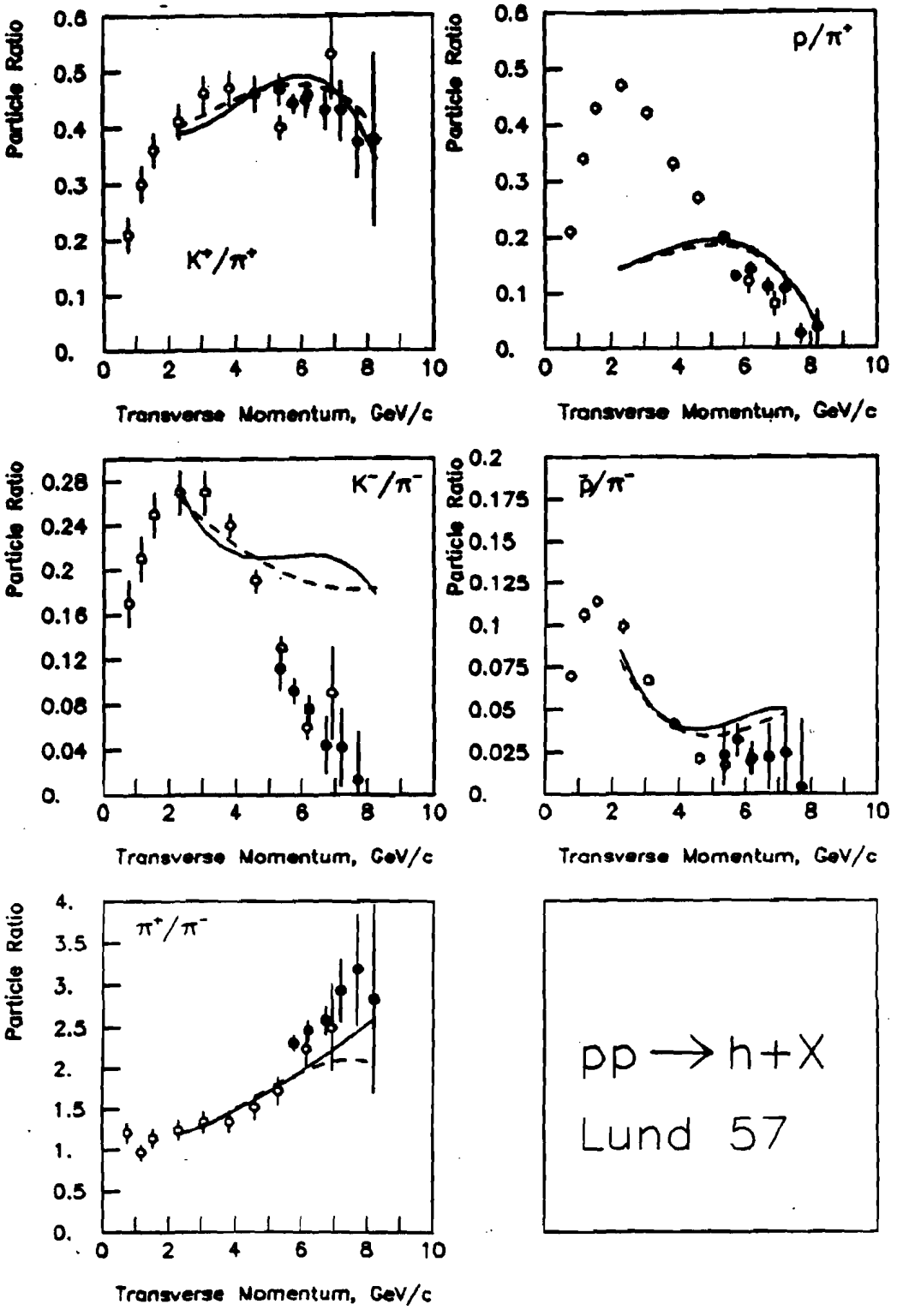
Particle Ratio
K^+/π^+
p/π^+
K^-/π^-
$\bar{p}/\pi^-$
π^+/π^-
Transverse Momentum, GeV/c
pp → h+X
Lund 57

Figure 46b